受入
87-1-320
高工研図書室

EUROPEAN ORGANIZATION FOR NUCLEAR RESEARCH

CERN-EP/86-213
December 16th, 1986

THE UA5 HIGH ENERGY $\bar{p}p$ SIMULATION PROGRAM

UA5 Collaboration
Bonn[1], Brussels[2], Cambridge[3], CERN[4] and Stockholm[5]

G.J. Alner[3*], K. Alpgård[5], R.E. Ansorge[3], B. Åsman[5], C.N. Booth[3+], L. Burow[1], P. Carlson[5], R.S. DeWolf[3], B. Eckart[1], G. Ekspong[5], I. Evangelou[4$], A. Eyring[1], K.A. French[3], L. Fröbel[1], C. Fuglesang[5], J. Gaudaen[2#+], C. Geich-Gimbel[1], B. Holl[1], K. von Holt[1], R. Hospes[1], D. Johnson[2], K. Jon-And[5], Th. Kokott[1], F. Lotse[5], N. Manthos[4$], R. Meinke[1], Th. Müller[1+], H. Mulkens[4], D.J. Munday[3], J.E.V. Ovens[3], W. Pelzer[1], J.G. Rushbrooke[3], H. Schmickler[1], F. Triantis[4$], L. Van hamme[2], Ch. Walck[5], C.P. Ward[3], D.R. Ward[3], C.J.S. Webber[3], A.R. Weidberg[3+], T.O. White[3], G. Wilquet[2] and N. Yamdagni[5].

1 Physikalisches Institut der Universität Bonn, Germany
2 Inter-University Institute for High Energies (ULB-VUB), Brussels, Belgium
3 Cavendish Laboratory, Department of Physics, Cambridge University, UK
4 CERN, Geneva, Switzerland
5 Institute of Physics, University of Stockholm, Sweden

ABSTRACT

The UA5 Monte Carlo program, consisting of a non-diffractive event generator GENCL, a diffractive event generator DIFFR and a tracking program are described. The inputs to the event generators are explained in detail. Their outputs are compared to available data from the $S\bar{p}pS$ Collider, and the agreement is shown to be good. The importance of some features of the generators are discussed. It is shown that cluster production and leading baryons are necessary to describe non-diffractive phenomena.

(Submitted to Nuclear Inst.and Methods)

* Member of Rutherford Appleton Laboratory, Chilton, Didcot, UK.
# Also at the Universitaire Instellingen Antwerpen, Antwerp, Belgium.
$ Also at the University of Ioannina, Greece.
+ Now at CERN

1. INTRODUCTION

During recent decades experiments in high energy physics have become progressively larger and more complex. The experimental hardware has grown in size and as the collision energy has increased, the final states of the particle collisions have become more complicated.

The highest energy collisions during the last few years have been $\bar{p}p$ collisions in the CERN Collider at centre of mass energies from 200 to 900 GeV. The main aim of the UA5 experiment was to search for new phenomena (notably the so called Centauro phenomenon observed in cosmic ray experiments [1]) at these very high energies and to investigate the gross features of low transverse momentum (p_T) collisions.

The UA5 experiment took data in October and November 1981 and in September 1982 at $\sqrt{s}$=546 GeV and in March-April 1985 from 200 to 900 GeV, the latter with the Collider operated in pulsed mode [2]. The detector and standard analysis procedures are extensively described in ref. [3]. Two large streamer chambers, 6m×1.25m×0.5m, were placed 5 cm above and below the axis of the SPS beryllium beam pipe (fig. 1.1). The geometrical acceptance is about 95% for $|\eta|<3$, falling to zero at $|\eta|=5$ (η is the pseudorapidity, $\eta=-\ln \tan\theta/2$, where θ is the c. m. emission angle). Each chamber is viewed by three cameras, which are equipped with mirror systems to give stereoscopic pairs of views. The trigger for the high voltage pulse to the chambers was provided by scintillation counter hodoscopes at each end of the chambers, covering the pseudorapidity range $2<|\eta|<5.6$.

We have reported on the general properties of the $\bar{p}p$ interactions, namely multiplicity distributions [4-9], rapidity distributions [8,10-12], particle ratios [9], correlations [13], strange particle production [14-16], photon production [17], search for new phenomena [17,18] and cross sections and diffraction dissociation [2,12]. An extensive review of our results from the 546 GeV runs is given in paper [3].

The observed data have to be corrected for geometrical acceptances, secondary interactions in detector material, particle decays between the interaction point and the sensitive detector volume, and for trigger losses as well as for measurement errors. These corrections are made through the use of Monte Carlo techniques since sufficient precision can not be reached by analytical methods due to the complexity of the final states and the geometry of the detector.

This paper gives a description of the UA5 Monte Carlo correction techniques, consisting of two main parts. The first part, which is detector independent and therefore of general interest, is an event generator which produces the final state particles of the $\bar{p}p$ interaction. In the second part the particles are tracked through the detector from the interaction point and the measurements with their errors are simulated. The purpose of this paper is to make clear what the Monte Carlo program contains so readers better can judge our corrected data, to show where data are strongly dependent on the corrections (e.g. diffractive data) and to explain some non-trivial results of the generator (multiplicity distributions in limited pseudorapidity regions, "spikes" and "mini-jets").

It is important for the quality of the final corrected data that the Monte Carlo program simulates reality as well as possible. For the tracking routines one can rely on well understood physical processes (electromagnetic and nuclear interactions, multiple scattering, decays of unstable particles etc) and one can get almost any degree of accuracy depending on the availability of computer time. The event generator, however, is generally made in an iterative way, since the production characteristics are not known a priori but are rather the experimental objective. One starts with an educated guess of the properties of the interaction augmented by theoretical prejudices and makes a generator. After comparison with data, changes are made, followed by new comparisons until satisfactory agreement is reached.

The event generators described in this paper have developed through the years in parallel with the analysis of the UA5 data. At different times corrections to data have relied on the current version of the event generators. The generators are still developing and indeed the production of this paper will probably give us ideas for new improvements. Here only the latest version is described. It can be regarded as a "snapshot" of the UA5 Monte Carlo program as it looks in September 1986.

We emphasize that our event generators are based on ad hoc models. They are mixtures of some basic physical ideas together with ad hoc inputs taken from data. The most important physical inputs are energy and momentum conservation, clustering, leading baryons and p_T limited phase space. Parameters and details change when data become available and are tuned so as to reproduce most of the basic features of low p_T $\bar{p}p$ interactions at high energy. The main purpose of the event generators is to be used to correct data. Some observed distributions are "forced" into the models (e.g. the charged multiplicity distribution), but interestingly enough there are features of the data that are not put into the generators but come out correctly, giving support to the underlying assumptions. One gets a hint of which physics

picture can be correct, and which cannot, by trying to understand why some non-input features come out correct and why others do not. Particularly it is found that clusters are needed to reproduce data. It is also seen that leading baryons are important for semi-inclusive pseudorapidity distributions.

The outline of the paper is as follows: In section 2 we describe the general principles of the event generators. In section 3 we compare the output of the generators with data and discuss the tuning necessary to reproduce some features of the data. The detector simulation routines are decribed in section 4. A summary and conclusions are given in section 5.

2. PRINCIPLES FOR THE EVENT GENERATORS.

An event generator is a Monte Carlo program that produces a simulated final state of an interaction, i.e. particle identities and particle momenta. In the UA5 experiment two event generators are used for different classes of high energy $\bar{p}p$ interactions. The event generator GENCL is used for simulating non diffractive (ND) events and the generator DIFFR for diffractive events. In ND events (fig. 2.1.a) particles are produced in a central region, flat in rapidity, and in two fragmentation regions. In the fragmentation regions leading particles emerge. Diffractive events can be single diffractive (SD) or double diffractive (DD). An event is called SD when one of the two interacting particles is still intact after the collision and the other particle has been excited to a system of higher mass but with the same quantum numbers (except possibly spin), which subsequently decays (fig. 2.1.b). In a DD event both the proton and the antiproton are excited to higher mass diffractive systems and they are assumed to decay independently (fig 2.1.c).

Experimentally it is very difficult to distinguish between ND and DD events. Therefore one often uses the concept non single diffractive (NSD) events, which are both ND and DD events. GENCL is actually tuned to and used to correct NSD data, although it technically speaking is a ND event generator.

The first subsection describes GENCL, the second DIFFR and in the last subsection we describe the changes of GENCL and DIFFR made in order to simulate Centauro events. These are events reported in cosmic ray experiments [1], which are supposed to contain very many baryons with high transverse momentum, and virtually no photons at all.

2.1 THE NON DIFFRACTIVE EVENT GENERATOR

The non diffractive event generator GENCL is an ad hoc model aiming to reproduce as many features of particle production as possible. An event is built up of two leading and a varying number of central clusters (16 on average at $\sqrt{s}$=546 GeV). Each cluster is given a transverse momentum p_T and a rapidity y. After transforming the rapidities to conserve energy and momentum the clusters are made to decay isotropically. The following is a technical description of how an event is generated.

2.1.1. Charged multiplicity

As the first step in generating an event the number of charged particles n_{ch} in the event is drawn from a negative binomial distribution

$$P(n;\langle n\rangle,k) = \begin{bmatrix} n+k-1 \\ k-1 \end{bmatrix} \left[\frac{\langle n\rangle/k}{1+\langle n\rangle/k}\right]^n \frac{1}{(1+\langle n\rangle/k)^k} \qquad (2.1)$$

where $\langle n\rangle$ is the average and k is a parameter determining the shape. Of course, n_{ch} has to be even, so the resulting distribution is not strictly a negative binomial. The energy dependence of $\langle n\rangle$ and k are taken from fits to data. Our latest fits are given in ref. [7], although the program actually uses an earlier result for $\langle n\rangle$:

$$\langle n\rangle = -9.50+9.11\cdot s^{0.115} \qquad (2.2)$$

$$k^{-1} = -0.104+0.029\cdot\ln(s) \qquad (2.3)$$

2.1.2. Particle composition

This section describes how particle species that make up the given n_{ch} charged particles are determined and furthermore how a certain number of neutral particles are generated. The basic particle production mechanism is by cluster formation and decay, and GENCL is therefore a cluster Monte Carlo program.

Six different types of clusters are made according to Table 1. There are always two leading clusters produced, consisting of a nucleon or a Δ or their antiparticles. The fraction of Δ's is determined by an input parameter R_Δ. For results presented here, unless otherwise stated, R_Δ=0 has been used. The value of R_Δ makes little difference except for the x_F-distribution of leading baryons (see end of sec. 2.1.3 and sec. 3.1.3).

Central baryons and strange particles are produced in pairs in order to locally conserve the baryon and strangeness quantum numbers. We choose the numbers of pairs in the following way. The ratios of average numbers of different particle types have been parametrized as linear functions of ln(s) using ISR and $\sqrt{s}$=546 GeV [9,15,16] data:

$$R_N = \frac{n_{\text{nucleons}}}{n_{\text{all charged}}} = -0.008+0.00865\cdot\ln(s) \qquad (2.4)$$

$$R_Y = \frac{n_{\text{hyperons}}}{n_{\text{all charged}}} = -0.007+0.0028\cdot\ln(s) \qquad (2.5)$$

$$R_\Xi = \frac{n_{\Xi^-}}{n_{\Lambda \text{ not from } \Xi}} = -0.16+0.028\cdot\ln(s) \qquad (2.6)$$

$$R_K = \frac{n_{K^+ + K^-}}{n_{\pi^+ + \pi^-}} = 0.024+0.0062\cdot\ln(s) \qquad (2.7)$$

From these ratios, assumed independent of n_{ch}, we can compute the mean number of pairs of each type for the events. The actual numbers of pairs of each type are then drawn in turn from Poisson distributions by making the Poisson parameters proportional to the number of charged particles still to be

made at each step, n'_{ch}:

$$\text{No. of nucleon pairs} = \text{Poisson}(R_N \cdot n'_{ch}/2) \qquad (2.8)$$

$$\text{No. of hyperon pairs} = \text{Poisson}(R_Y \cdot n'_{ch}/2)^{\S} \qquad (2.9)$$

$$\text{No. of xi pairs} = \text{Poisson}(2/3 \cdot R_\Xi \cdot R_Y \cdot n'_{ch})^{\S} \qquad (2.10)$$

where the 2/3 is because 2/3 of the hyperons are Λ's, and

$$\text{No. of kaon pairs} = \text{Poisson}(R_K/(1+R_K) \cdot n'_{ch}) \qquad (2.11)$$

The identities of the pairs are decided succesively at each step with particle probabilities according to column 3 and 4 in table 1. Each kaon will be a K^* with 60% probability in accordance with ISR measurements [19].

The remaining charged particles (normally some 80-90% of the total but it can occasionally be zero) are π^+ and π^-. They are put together with π^0's into clusters. Several algorithms for doing this have been tried. Only the latest method will be mentioned.

The method is based on drawing the number of charged π's and the number of π^0's in a cluster from two independent Poisson distributions. First the numbers of charged π's in the clusters are drawn from a distribution with an average of 1.8. The procedure is repeated until there are no charged particles left. If the sum of the drawn numbers does not equal the number of particles left, a method of adjustment is used which can either increase or decrease cluster sizes, thus avoiding any bias towards too many small clusters. (See appendix A.) Then there will be say n_c pion clusters, where some might contain no charged π's.

Secondly the number of neutral pions is decided for each of the n_c clusters. (If there are no charged π's from the beginning n_c will be set to one.) The π^0 Poisson parameter, μ_{π^0}, is chosen such that one gets the observed ratio and correlation of n_γ and n_{ch} [20], also taking into account the π^0's coming from decaying K^*'s. The only source of photons in GENCL is π^0's. The average number of photons, $\langle n_\gamma \rangle$, is parametrised versus n_{ch} by

$$\langle n_\gamma \rangle = 2+1.03 \cdot n_{ch} \; . \qquad (2.12)$$

Since 60% of the kaons are K^*'s and of these 1/3 yield one π^0 when decaying (see sec. 2.1.4), on average one gets $\frac{1}{3} \cdot 0.60 \cdot 2 \cdot \mu_K = 0.4 \cdot \mu_K$

§ Strictly speaking n'_{ch} in eqs. 2.9 and 2.10 should be the n'_{ch} appearing in eq. 2.8 (compare eqs. 2.5-2.6). However this is the way it is done, and the resulting errors are certainly much smaller than the uncertainties in the parameters of eqs. 2.5-2.6.

number of π^o's from K^*'s, where $\mu_K = R_K/(1+R_K)\cdot n'_{ch}$ is the Poisson parameter for the kaon pairs (see eq. 2.11). Thus

$$\mu_{\pi^o} = [\tfrac{1}{2}\cdot(2+1.03\cdot n_{ch}) - 0.4\cdot\mu_K] \;/\; n_c \qquad (2.13)$$

where n_c is the number of pion clusters.

A few clusters (~5%) will end up with zero charged pions and zero π^o. These are disregarded, and as a consequence the output average number of charged π's per cluster is increased to 1.88. The average number of charged π's in a cluster has been chosen by tuning the Monte Carlo to correlation data [13]. On average one finds 1.3 π^o per pion cluster.

All clusters made up of more than one particle are given some excitation energy in terms of an additional mass. For the kaon and baryon pair clusters the excitation energy q follows the distribution

$$\frac{dN}{dq^2} \propto e^{-\frac{2}{a}q} \qquad (2.14)$$

where a is a free parameter adjusted to get the desired $\langle p_T \rangle$ for different particle types. For kaon pairs a=0.75 GeV and for the baryon pairs a=0.4 GeV. The pion clusters are given masses m from the following distribution

$$\frac{dN}{dm} = 1.1\cdot(1+No(0,0.2))\cdot\exp(\tfrac{1}{3}n_\pi - 1) \qquad (2.15)$$

with a lower cutoff in mass at $n_\pi \cdot 0.15$ GeV where n_π is the number of pions in the cluster. No(0,0.2), which denotes a number drawn from a Gaussian distribution with mean 0 and standard deviation 0.2 GeV, introduces a width to the mass distribution. This mass distribution is chosen to roughly represent the masses of known resonances [21]. As an example for n_π=2 one gets on average a mass of 0.79 GeV which is close to the ρ mass of 0.77 GeV and a width of 0.16 GeV compared to 0.15 GeV for the ρ.

At $\sqrt{s}$=546 GeV the generation method above results in 16.2 central clusters on average, and of these, 2.2 clusters contain only neutral particles.

2.1.3. Phase space

The clusters are given transverse momenta p_T and longitudinal momenta p_L in two steps. The transverse momenta are randomized from either an exponential distribution

$$\frac{dN}{dp_T^2} \propto e^{-b\cdot p_T} \qquad (2.16)$$

or a power law distribution

$$\frac{dN}{dp_T^2} \propto \frac{1}{(p_T+p_o)^n} \qquad (2.17)$$

where b, p_o and n are free parameters to be adjusted (see sec. 3.1.4).

However, at this stage transverse momenta are given to clusters and it is not trivial to calculate what the momenta of the decay products will be [22]. There is an underlying physical idea to this two component distribution: The exponential part represents soft processes and the power-law represents the low p_T-tail of hard processes [22].

Single pions (~10% of all clusters) always get their transverse momenta from the exponential distribution, because the tail of the single particle p_T-distribution otherwise becomes too strong. In other cases the relative amount of the two distributions is made to depend on the multiplicity of the event. The probability P for a cluster to get p_T from equation 2.17 is assumed to increase linearly with the total number of clusters in the event, n_{tot}: $P=0.03 \cdot n_{tot}$ (or $P=1$ for $n_{tot} \geq 34$). In this way the average transverse momentum increases with n_{ch}, as found in data [23,24]. The exponential form is made to dominate in the region of small p_T and equation 2.17 to dominate at large p_T. This is qualitatively in agreement with p_T-distributions for particles found in data [16,23]. To achieve a rise of $\langle p_T \rangle$ with energy the parameter n is assumed to be a function of energy according to

$$n = 3 + \frac{1}{0.01+0.011 \cdot \ln(s)} \qquad (2.18)$$

This relation together with $p_o=3.0$ GeV/c and a slope of the exponential part of 6 $(GeV/c)^{-1}$ gives a good description of data [24]. Azimuthal directions are drawn uniformly between 0 and 2π. To conserve momenta in the yz-plane perpendicular to the beam axis (x direction) we make two independent linear translations in p_y and p_z:

$$p_i^{new} = p_i^{old} - (\Sigma p_i^{old})/N \quad ; \; i=y,z \qquad (2.19)$$

where the summation is over the N clusters in the event. Note that p_T is generated independent of rapidity.

Longitudinal momentum is given to a cluster by assigning to it a rapidity y, since

$$p_L = m_T \cdot \sinh(y) \qquad (2.20)$$

where $m_T=\sqrt{(m^2+p_T^2)}$ is the transverse mass. Rapidity distributions have a central plateau and a fall off at higher values of |y| [3,8,10,11]. "Pre-rapidities", y', are generated at random from a similar distribution. "Pre-rapidity" is used rather than rapidity at this stage, because the transformations done later to conserve energy and momentum markedly change the shape of the distribution. It is found that a flat central part with Gaussian wings, where the ratio of the width of the flat part to the standard deviation

of the Gaussian part is 1.2 (fig 2.2), gives satisfactory agreement with data in the energy region of the SPS Collider (see sec. 3.1.2).

As many numbers from this distribution as we have clusters are drawn. The two leading clusters are given the smallest and highest pre-rapidities with a very large probability. An ad hoc assumption for the probability for the leading cluster to get the k:th largest (smallest) pre-rapidity is used:

$$P(k) = 1-(1-\frac{k}{N/2})^{<n_{ch}>} \qquad (2.21)$$

where N is the number of clusters. For example, for $<n_{ch}>=29.1$ and N=18 this gives P(1)=0.97. The remaining pre-rapidities are randomly distributed among the other clusters. The pre-rapidities are transfomed into true rapidities by $y = A+By'$, where A is determined from p_L conservation, and B from energy conservation [25].

The kinematics for the event is now fully specified and other variables for the clusters can be calculated, such as the Feynman scaling variable x_F, defined by

$$x_F = \frac{p_L}{p_{beam}} \qquad (2.22)$$

This variable measures, in the c.m. frame, the fraction of the beam momentum which is contained in the longitudinal momentum component of a cluster. At high collision energies rapidity and x_F are related by

$$x_F = \frac{2m_T}{\sqrt{s}}\cdot\sinh(y) \qquad (2.23)$$

The generation method gives a generally flat x_F-distribution with a peak very close to $|x_F|=1$ for the leading baryon, i.e. the proton or the neutron with highest (lowest) x_F, which is supposed to be the main remnants of the incoming proton (antiproton). For leading baryons it is difficult to determine the distribution of x_F experimentally, but it has some effect on our trigger efficiencies. Thus we want to try different forms of the x_F-distribution for the leading baryon, in particular one that goes like $1-|x_F|$ at large $|x_F|$ [28], which is in fact now the default distribution. It is done by "brute force". If $|x_F|>0.95$ for a leading cluster a weight is calculated, $w=20\cdot(1-|x_F|)$, and the kinematics of the event is kept with probability w. If it is rejected one starts all over again generating momenta for all clusters (p_T and y), but at most 20 attempts are done. Another factor which suppresses $|x_F|$ close to one, is that if an event has very few clusters (2 or 3) one starts from the very beginning again but with the same n_{ch} (a maximum of 10 times). This is done because such events will always, from kinematical reasons, give clusters close to $x_F=1$.

2.1.4. Decays

The final step in the particle generation is the decay of clusters and of short lived particles. The decays are generated uniformly in phase space, and are therefore isotropic. The decays of the clusters are done with performed with the program FOWL [26]. The particle decays taken into account are:

$K^{*o} \rightarrow K^o\pi^o$ (1/3), $K^+\pi^-$ (2/3)
$K^{*+} \rightarrow K^o\pi^+$ (1/3), $K^+\pi^o$ (2/3)
$\pi^o \rightarrow \gamma\gamma$ (98.85%), $e^+e^-\gamma$ (1.15%)
$\Delta^{++} \rightarrow p\pi^+$
$\Delta^+ \rightarrow p\pi^o$ (2/3), $n\pi^+$ (1/3)
$\Delta^o \rightarrow p\pi^-$ (1/3), $n\pi^o$ (2/3)

and correspondingly for antiparticles. After the decays are performed we have n_{ch} charged particles, as decided in the very beginning of the event. (Actually this is true only to 99%. Any $\pi^o \rightarrow e^+e^-\gamma$ decay is not included in this n_{ch}. On average an event will have $\sim n_{ch}/2$ π^o's, each having a probability of 1.15% to make this decay, giving two extra charged particles. Thus the increase of n_{ch} is only about 1%.) From now on K^o's (and $\bar{K}^o$'s) are considered to be K^o_S or K^o_L with equal probability.

2.2 THE DIFFRACTIVE EVENT GENERATOR

For analysis of diffractive events UA5 has a special event generator, DIFFR. At this stage the diffractive event generator is quite simple, mainly because the analysis is still elementary and not many data exist to tune the generator to. DIFFR can simulate both single and double diffractive events. Like in GENCL there is a minimum of theoretical assumptions behind the model. The main goal is to reproduce data. Good reviews of diffractive phenomena can be found in [27,28] and recent experimental results are given in [29,30].

DIFFR chooses a mass M for the diffractive cluster (clusters) and a four-momentum transfer squared (-t). A cluster decays into one nucleon and a number of π's. The decay is either isotropic or according to a cylindrical phase space, depending on $\langle p_T \rangle$ of all the particles in the cluster.

The mass M of the diffractive cluster is drawn from the following distribution:

$$\frac{dN}{d(M^2/s)} \propto \frac{1}{M^2/s} \qquad (2.24)$$

This results from triple Pomeron Regge theory [27] and is well supported by data [28]. There is a lower cutoff in M of 1.08 GeV ($=m_{\pi}+m_p$) and an upper cutoff such that $M^2/s \leq 0.05$. The latter is to fulfill the "coherence" condition for diffractive excitation [27] and to conform to most previous experiments [30]. The four-momentum transfer squared (-t), is randomized from an exponential distribution in $t-t_{min}$ with a slope of 7 $(GeV/c)^{-2}$ [28], where t_{min} is the minimum four momentum transfer squared needed to produce the clustermass (-masses) generated above. Although phenomenologically the exponential slope of the -t-distribution is dependent on the mass of the cluster, the UA5 trigger is not sensitive to this, and thus for simplicity a fixed slope is used.

The charged multiplicity, n_{ch}, of a cluster with mass M is decided in the same way as in GENCL. It is randomized from a negative binomial distribution (eq 2.1), but with s replaced by M^2 in the equations for the parameters $\langle n \rangle$ and k^{-1} (eq 2.2 and 2.3), although $\langle n \rangle$ is restricted to be ≥ 0.5. This is in agreement with the latest data which show that diffractive clusters of mass M behave much like non diffractive events with c.m. energy $\sqrt{s}=M$ [29]. For masses that are so small that k^{-1} goes below zero, n_{ch} is drawn from a Poisson distribution with mean $\langle n \rangle$. (In the limit $k^{-1} \to 0$, the negative binomial distribution becomes a Poisson distribution.) In all cases n_{ch} is

made odd, in order to conserve the charge quantum number.

The number of neutral particles in the cluster is assumed to follow a Poisson distribution with mean $(1+0.52\cdot n_{ch})$. This gives the same correlation between charged and neutral particles as in ND events (cf. eq. 2.12). All clusters will contain one nucleon, n or p with equal probability (or their antiparticles if it is a $\bar{p}$-diffractive cluster), and the other particles will be pions.

The clusters are first made to decay isotropically. This is done with the program FOWL [26]. If the average of the transverse momenta of the decay particles is larger than a cut parameter p_c, the decay of the diffractive cluster is recalculated following a cylindrical phase space instead. Thus the parameter p_c can be used to adjust the average transverse momentum of the particles generated. A large p_c will always give isotropic decays with [28]

$$\langle p_T \rangle = \frac{\pi}{4} \frac{M}{1.5\langle n_{ch} \rangle} \qquad (2.25)$$

whereas $p_c \to 0$ will always give cylindrical decays. p_c=0.4-0.5 GeV/c, corresponding to $\langle p_T \rangle$=0.35-0.45 GeV/c, gives good agreement with data (see sec. 3.2). The cylindrical phase space is generated by the method of Jadach [25]. The average p_T is p_c and the rapidity is uniformly distributed. The nucleons are given the largest rapidities. Finally $\pi^0 \to \gamma\gamma$ decays are performed.

2.3 CENTAURO EVENT GENERATION.

In cosmic ray experiments the Centauro events have been described as having high multiplicities, high p_T and containing no or very few photons [1]. The production mechanism is unknown and therefore we try different ways to produce these kind of events. One way to simulate such events is with the GENCL event generator with the following modifications:

A high, narrow multiplicity distribution is generated by fixing <n>=75 and k^{-1}=1/30 in equation 2.1. By setting R_N=2 (eq. 2.4), R_Y=R_Ξ=R_K=0 (eq. 2.5-2.7) and μ_{π^0}=0 (eq. 2.13), we create no strange particles and no π^0's and thus no photons. This gives on average as many nucleon pairs as we have charged particles, i.e. 75 pairs containing together 150 protons and neutrons (and their antiparticles) in the mean. Only about half of the events contain π-clusters with just a few charged π's.

The clusters are given transverse momenta from a

$$\frac{dN}{dp_T^2} \propto e^{-bm_T} \qquad (2.26)$$

distribution. b is an input parameter which is varied to try different scenarios. Typically b=1 GeV^{-1}, giving the particles an average p_T of 1.4 GeV/c.

Another way to generate Centauro events is with the DIFFR event generator. A "fireball" of mass ~250 GeV is produced which decays into ~100 baryons. This is like the Brazil-Japan collaboration interpretation of their data [1].

The mass of the "fireball", or diffractive cluster, is Gaussian distributed with mean 250 GeV and standard deviation 25 GeV. The number of charged particles n_{ch} is drawn from a Poisson with mean 50. One will be a leading proton and the rest protons and antiprotons (same amount of each). The number of neutral particles is drawn from a Poisson with mean n_{ch}, they will all be neutrons and antineutrons. The "fireball" decays isotropically (p_c is set to a large value) giving a $\langle p_T \rangle$ of 1.77 GeV/c.

A recent search for Centauro events at $\sqrt{s}$=900 GeV is given in reference [18].

3. COMPARISON BETWEEN GENERATED EVENTS AND DATA

In this section we compare the output of the event generators with data. We look at most features for which data are available. Where it is not obvious we discuss why the output and data agree or disagree. We also show some interesting distributions for which no data exist yet, such as Feynman-x distributions for leading particles.

3.1 NON DIFFRACTIVE EVENTS

3.1.1 Particle yields

In table 2 the average number of all particle types in the final states of GENCL-generated events at $\sqrt{s}$= 200, 546 and 900 GeV are given. Naturally they agree with data at 546 GeV since these data have been used as input. For comparison data are given in brackets in the table.

3.1.2 Pseudorapidity distributions

The input to the generator is a flat distribution with gaussian wings in "pre-rapidity" (fig. 2.2) for the clusters, independent of both c.m. energy and event multiplicity. This gives a good description of pseudorapidity distributions for charged particles, both for fixed multiplicity (fig. 3.1) and at three Collider-energies (fig. 3.2), although the input distribution has been tuned only to 546 GeV data. It shows that from GENCL's point of view, the variation of the pseudorapidity distributions with multiplicity and $\sqrt{s}$ in this energy region is primarily an effect of energy and momentum conservation.

It is possible to achieve an even better agreement with data by making the pre-rapidity distribution dependent on the c.m. energy. This is also needed in order to get a fair reproduction of pseudorapidity data at $\sqrt{s}$=53 GeV. One parametrizes the width of the flat part F of the pre-rapidity distribution (see fig. 2.2) as

$$F = 0.38+11800\cdot(\ln\sqrt{s})^{-5.2} \qquad (3.1)$$

keeping the s.d. of the Gaussian wings fixed at one. Note that as the collision energy grows, the pre-rapidity distribution gets more and more Gaussian.

It is interesting to see the difference in rapidity and pseudorapidity distributions for the same set of particles. Figure 3.3 shows these distributions for charged particles from events generated by GENCL at $\sqrt{s}$= 200 GeV and 900 GeV. The small bumps close to y_{beam} (=$\ln(\sqrt{s}/m_p)$, the rapidity

of the beam particle), are from the leading protons, shown by the shaded region.

The necessity for leading clusters in the generator is most clearly seen in pseudorapidity distributions for fixed multiplicities. When the leading clusters are turned off in the sense that they are randomly placed in pre-rapidity, as all other clusters (eq. 2.21 is ignored), GENCL fails to reproduce data. Figure 3.4 compares this variant of GENCL (dashed line) with data and the normal version of GENCL (full line). The figure also shows that a strictly uniform x_F-distribution (independent of n_{ch}) imposed on the leading clusters does not reproduce data either (see further sec. 3.1.3). The key feature of the generator seems to be the location of the leading baryons very near the ends of the rapidity chain.

3.1.3 Feynman-x and inelasticity distributions

The Feynman-x, x_F (see eq. 2.22), distribution for the leading baryons has not been measured at the SPS Collider. Nevertheless it is a theoretically important concept. In ref. [31] Basile et al., present data [32] at $\sqrt{s}$=14-28 GeV, from which they conclude that the x_F-distribution falls about a factor two between x_F=0 and 0.95 and then drops to 0 for x_F=1. Experimental information at lower energies is given in reference [33,34]. Figure 3.5 shows GENCL's $|x_F|$-distribution for leading baryons at $\sqrt{s}$=546 GeV, using three different options. The leading baryon is always taken as the proton or neutron (or their antiparticles) from the leading cluster. One sees that when we do not use the $1-|x_F|$ suppression at large $|x_F|$ (see sec. 2.1.3) the distribution peaks at $|x_F|$=1. The peak can be suppressed arbitrarily much by increasing R_Δ to 1, but we prefer the "brute force" method with the $1-|x_F|$ suppression at $|x_F|$>0.95 (see sec 2.1.3), which gives a somewhat flatter distribution at intermediate $|x_F|$-values. The shape of the distribution does not change much with $\sqrt{s}$, only the maximum around $|x_F|$=0.3 decreases ~5% when going from 200 GeV to 900 GeV.

The smaller peak at $|x_F|$=0.95 (in the default version) contains the same protons as the bump close to y_{beam} in the rapidity distribution in figure 3.3 (compare eq. 2.23). The bumps appear as an effect of the suppression at the peak at $|x_F|$=1, but if we do not use the suppression we will get a small spike at $y=y_{beam}$ instead (as long as R_Δ does not equal 1). Probably GENCL needs a more sophisticated way to simulate the leading clusters, but at the moment, and since there are no data in this kinematical region, we prefer simple ways of trying different distributions.

The main reason for trying different distributions is that the trigger efficiency of the UA5 detector is dependent on the $|x_F|$-distribution. Figure 3.6 shows the probability for a trigger in one trigger arm only (see fig. 1.1) as a function of $|x_F|$ for the leading baryon on that side. It is clear that the shape of the x_F-distribution for x_F>0.95 is crucial for the trigger efficiency. This can be understood from the following simple kinematical argument. If the leading particle has Feynman-x x_F, the

remainder of the event has effective mass given by $M^2=(1-|x_F|)s$. This system is produced at rapidity $\ln(M/\sqrt{s})$, and the resulting particles will spread over $\pm\ln(m_T/M)$ units of rapidity (where $m_T^2=p_T^2+m^2$). Thus the closest particle to the leading particle will be at rapidity $\sim\ln[M^2/(m_T\sqrt{s})]$, and as this value approaches 2 the probability of no particles hitting the trigger hodoscopes on the same side as the leading particle becomes large, and a 1-arm trigger results. (Compare with single diffraction [12,28]). The leading particle itself usually passes inside the beampipe. For example, the 2-arm efficiency has fallen to ~50% at $x_F=0.98$, which corresponds to a maximum rapidity (taking $p_T=0.4$ GeV/c) ~3, which is approaching the outside of the trigger hodoscopes.

Table 3 shows the trigger efficiency ε for the three distributions shown in figure 3.5, and also ε at 200 and 900 GeV for the default distribution. They have been determined by assuming that a charged particle pointing to a hodoscope will always give a trigger and that a neutral particle pointing to a hodoscope will give a trigger with 40% probability (through decay or secondary interaction). Comparison with the full Monte Carlo (tracking etc.) has shown that this is a reasonable assumption. 1A denotes a hit in one trigger arm together with a veto in the other and 2A denotes hits in both arms. It is essentially the relative sizes of 1A and 2A that changes, the sum staying very close to 100% in all cases. One should note that the value of R_Δ is not so important for the relative sizes, whereas the $1-|x_F|$ suppression makes a difference. The important thing for the trigger efficiency is x_F for the leading cluster, whether it be N or Δ, as one can see from the above kinematical argument.

Trigger efficiencies are of importance for cross section studies [2] and also for e.g. studies of multiplicity distributions for non single diffractive (NSD) events. These are based on 2A data and we try to correct the data for (among other things) trigger losses. Trigger losses are most important for low multiplicities, the 2A trigger efficiency being close to 100% for $n_{ch}>20$.

Note that apart from the $1-|x_F|$ suppression at $|x_F|>0.95$ no x_F-distribution is imposed by the generator, and the distribution is just a result of other inputs. A truly uniform x_F-distribution was imposed on the leading clusters in order to study possible systematic errors on the trigger efficiencies, but it was found that this did not reproduce pseudorapidity distributions in limited multiplicity intervals (fig. 3.4), and we conclude that a uniform distribution is not possible (in our framework, at least).

A study at ISR [35] has shown that the x_F-distributions of the two leading baryons in the same event are independent. The region $0.4<|x_F|<0.9$ was studied and it was found that $\langle x_F\rangle=0.6$ for one leading baryon

independent of the other. GENCL roughly has this feature, see figure 3.7. The increase at large $|x_F|$ and decrease at small $|x_F|$ are due to the correlation that energy and momentum conservation imposes, which will only appear close to the kinematical limits ($|x_F| \to 1$).

A concept of interest in some theoretical models (e.g. [36,37]) is the inelasticity k, defined to be the fraction of the energy that goes into particle production:

$$k = \frac{\sqrt{s} - E_1 - E_2}{\sqrt{s}} \qquad (3.2)$$

where E_1 and E_2 are the energies of the two outgoing leading baryons. A very good approximation is

$$k = 1 - \frac{|x_{F1}| + |x_{F2}|}{2} \qquad (3.3)$$

where x_{F1} and x_{F2} are the Feynman-x values for the two leading baryons. Our generator gives the inelasticity distribution shown in figure 3.8. It has a mean $\langle k \rangle = 0.50$ and the distribution looks the same at 200, 546 and 900 GeV. But when we do not use the $1-|x_F|$ suppression it changes a little so that $\langle k \rangle = 0.49$ with $R_\Delta = 0.0$ and $\langle k \rangle = 0.53$ with $R_\Delta = 0.5$. This can be compared with results from a statistical model [36], where it is claimed that $\langle k \rangle = 0.50$ up to and including ISR energies, and then decreases to 0.30 at $\sqrt{s} = 546$ GeV. Ref. [37] uses a geometrical model with another stochastic approach and fit their model to rapidity distributions in fixed multiplicity intervals. They arrive at $\langle k \rangle = 0.28$ at $\sqrt{s} = 546$ GeV, but they assume that several leading particles can emerge on each side. However, there are also predictions for a softening of the leading baryon spectrum with energy, and thus an increase of the inelasticity [38]. We see that in the framework of our model the data can be well fitted with no change of inelasticity.

3.1.4 Transverse momenta

Average p_T for some particles at 546 GeV are compared with data in table 2. The agreement is good, which it should be since it is not difficult to reproduce only one value. It is much more difficult to reproduce full distributions. We have tried to mix two p_T-distributions for the clusters (eq. 2.16 and 2.17) in order to reproduce the dependence of p_T on both multiplicity and c.m. energy as well as the p_T-distribution itself for charged particles. This was done mainly by looking at the $\langle p_T \rangle$ versus n_{ch} data at 200 to 900 GeV [23,40] in the following way: At the lowest multiplicities $\langle p_T \rangle$ is ~0.37 GeV/c independent of $\sqrt{s}$. This determines the slope of the exponential part (eq. 2.16). Then $\langle p_T \rangle$ grows roughly linearly with n_{ch} up to n_{ch}~40, where it flattens out. This prompts us to increase the probability P for equation 2.17 linearly from zero at n_{ch}=0 to one at n_{ch}=40. But it is technically more easy (and physically more pleasing) to make the probability grow with the number of clusters, and thus $P=0.03 \cdot n_{tot}$, where n_{tot} is the number of clusters. Finally the height of the plateau at high multiplicities is used to adjust the parameters p_o and n in equation 2.17. Since the height increases from ~0.44 GeV/c at 200 GeV to ~0.49 GeV/c at 900 GeV, at least one of the parameters needs to be dependent on $\sqrt{s}$, and it seems natural that it should be n, the power. When choosing n and p_o an eye was also kept on the p_T-distribution. After we fixed p_o and tuned n at 200 and 900 GeV, n was parametrized as a function of ln(s) through the two values, giving equation 2.18.

In figure 3.9 $\langle p_T \rangle$ versus n_{ch} in the pseudorapidity region $|\eta|<2.5$ is compared to recent preliminary data from UA1 [41]. Although the trends are qualitatively right, the Monte Carlo is mostly about 5% above data. The reason for this is that the tuning was done using a cut in y instead of in η, because older UA1 data were given in rapidity cuts [23]. However, one should also note that UA1 relies on a fit to extrapolate to low p_T, and uncertainties in the functional form in the low p_T region lead to systematic errors. The results of the generator are certainly within these errors. Note that whereas $\langle p_T \rangle$ for all charged particles agree within 2% with UA1's data (see tab. 2), at fixed multiplicity the difference is generally 2-3 times larger.

Figure 3.10 shows the $\langle p_T \rangle$ dependence on rapidity and pseudorapidity. It is seen that in the central region average momentum is clearly higher for a η-value than the same y-value. Although transverse momentum is generated independently of the "pre-rapidity", $\langle p_T \rangle$ is slightly dependent on the rapidity. The fall at large y is easy to understand from kinematical reasons. When particles have large rapidities there is less energy left to allow them to have large transverse momenta. The small bump at y=4.7 is because there are relatively more nucleons at large rapidities due to the leading baryons, and they have larger average p_T than the predominating pions (compare tab. 2). This is seen from the dotted curve in figure 3.10 that shows the $\langle p_T \rangle$ vs. rapidity for charged pions only.

The p_T distributions for charged particles and for kaons are compared to data in figures 3.11 and 3.12. UA1's data on p_T for charged particles is represented by the curve

$$\frac{A}{(p_T+1.30)^{9.14}} \qquad (3.4)$$

which is a very good parametrisation of data at $0.30<p_T<10$ GeV/c [23]. The normalisation constant A is chosen so that the curves cross at $p_T=0.5$ GeV/c. The agreement with data is good in both figures, except for $p_T>6$ GeV/c for the charged particles, where GENCL gives too many particles. But this region is not important for UA5 analyses. Presumably one needs proper jet fragmentation. In figure 3.12 we also show the effect of cutting in η instead of in y. There are then fewer particles with low p_T, thus increasing the average transverse momentum (compare with figure 3.10). In figure 3.13 the K/π ratio is given as function of p_T and compared to data [16]. The agreement with data is acceptable, although plausible production mechanisms (jets) would give a constant K/π ratio for higher p_T. The K/π curve is of course roughly the result of dividing the curves in fig 3.11 and 3.12 by each other.

3.1.5 Multiplicity distributions

The charged particle multiplicity distribution for the full phase space is of course in good agreement with data, since we generate multiplicities from distributions that are very good parametrisations to data. But there is no input for multiplicity distributions in limited regions of pseudorapidity, on which we have recently published a paper [5]. Thus it is interesting to compare the output with these data. Figure 3.14 shows the multiplicity distributions for the pseudorapidity regions $|\eta|<$ 0.2, 0.5, 1.5 and 3.0 at $\sqrt{s}$=546 GeV. The distributions are "KNO-plotted", i.e. $\langle n\rangle P(z)$ is plotted as a function of $z=n/\langle n\rangle$. The agreement is very good, although for the narrower η-regions GENCL tends to give a little too narrow a distribution, whereas it gives a somewhat broad distribution for the wider regions.

In paper [5] it was shown that multiplicity distributions in limited central η-regions are very well described by negative binomial distributions (eq. 2.1). We have fitted the generated distributions to negative binomials and compare the resulting values of the k-parameter of these fits with the results of paper [3] in figure 3.15 (solid line). Here η_c defines the interval according to $|\eta|<\eta_c$. Whereas the fits to data always are good [42], only the MC distributions for $\eta_c<0.5$ and $\eta_c>4.5$ give acceptable fits.

It is worth noting that the event generator reproduces these data so well,

although there is no input for it. If this feature is stable for the details of the model, such as cluster sizes and cluster masses, one might believe that the widening of the scaled multiplicity distribution in narrower pseudorapidity interval is primarily a kinematical effect, as has been suggested [43]. On the other hand if it is sensitive to some input, this can give an clue to the underlying physical process.

The effect of the cluster size ν was studied, by changing the average number of charged particles per cluster $\langle\nu\rangle$ from 1.8 to 1.1 and 2.7. How this was done technically is described in appendix B. A run was also made where the clustering was turned off completely (see app. B). Multiplicity distributions in limited pseudorapidity regions from these runs were then fitted by negative binomial distributions. The resulting k-values are shown in figure 3.15.

The version without clusters always gives very good fits. However, the behaviour of k in the latter case strongly disagrees with data, flattening out at a value of 2.4. Although a negative binomial distribution is imposed on the multiplicity of full phase space it is not obvious that also for limited phase space this distribution gives a good fit. If the primary distribution follows a negative binomial($\langle n\rangle$,k) (e.g. the multiplicity distribution in full phase space) and if every member of this distribution has the same probability q to have some characteristic (e.g. to fall in some limited η-range) then the resulting secondary distribution follows a negative binomial($q\cdot\langle n\rangle$,k), i.e. with the parameter k unchanged. When the particles are positioned one by one in pseudorapidity (no clustering), the second condition would be fulfilled were it not for energy and momentum conservation. But we have seen in figures 3.1 and 3.4 that energy and momentum conservation yields significantly different pseudorapidity distributions as a function of multiplicity, and thus the second condition is not valid.

The goodness of the fits when one has clusters is better for smaller cluster sizes, but is generally bad. It is only for very small ($|\eta|<0.2$) or very large ($|\eta|<5.0$) regions that the fits always are acceptable. Although no value of $\langle\nu\rangle$ gives an overall good description, the k-values for data are much closer to the normal version of GENCL with clustering, thus strongly indicating that cluster production is a mechanism needed to explain the data of reference [5]. The question of the cluster size is further discussed in the next subsection.

3.1.6 Particle correlations

Multiplicity correlations among particles emitted at various values of pseudorapidity were reported in paper [13]. Two symmetric, non-overlapping intervals in η, one forward (F) and one backward (B) were defined. For each event the number of charged particles falling in the two intervals, n_F and

n_B, were determined. It was found that the average value of the backward multiplicity at fixed forward multiplicity is well described by a linear relation

$$\langle n_B(n_F)\rangle = a+bn_F \qquad (3.5)$$

The slope b is a measure of the correlation strength between the multiplicities in the two intervals. The FB multiplicities from GENCL are also well fitted by eq. 3.5. In figure 3.16 the slope b from the event generator (solid line) is compared with preliminary data. In fig 3.16.a the F and B regions are $0<\eta<4$ and $-4<\eta<0$ respectively. However, due to the cluster decays there is a clear short range correlation signal (fig. 3.18). In order to reduce the likelihood of a single cluster contributing to both regions a gap of size 2 in pseudorapidity is used in figure 3.16.b, separating the two regions. The strength of the correlation then decreases somewhat. GENCL reproduces the rise of b with energy and the decrease of b when a gap is introduced, but generally GENCL gives a slope b that is too large. To show the dependence of b on the average cluster size $\langle\nu\rangle$, we changed $\langle\nu\rangle$ from 1.8 to 1.1 and 2.7 (see app. B), just as in section 3.1.5. The slope b is clearly sensitive to $\langle\nu\rangle$ and from fig 3.16 one would like $\langle\nu\rangle$ to be increased by about 50%, if this was the only test of $\langle\nu\rangle$.

Another test of the cluster size is to study, for a fixed multiplicity $n_S(=n_F+n_B)$, a distribution $f_S(n_F)$ giving the probability of finding n_F particles in the forward region. It thus describes how the n_S particles are shared between the F and B regions. It turns out that the correlation parameter b depends only on the variances $d_S^2(n_F)$ of the f_S distributions. One can show that the following identity holds between expectation values:

$$b = \frac{D_S^2/4 - \langle d_S^2(n_F)\rangle}{D_S^2/4 + \langle d_S^2(n_F)\rangle} \qquad (3.6)$$

where the symbol $\langle x\rangle$ means an average of x over the n_S distribution and D_S^2 is the variance of the n_S distribution. Note that the overall multiplicity distribution put in along with its moments introduces long range correlations, through the D_S^2 term in formula (3.6). The variance $d_S^2(n_F)$ is dependent on the cluster size, as can be seen from the following trivial example. Assume that (1) the number of clusters falling into F (or B) is governed by the binomial distribution, (2) all clusters have the same size ν, and (3) all ν particles from a cluster remain in the same region as the parent cluster, then

$$d_S^2(n_F) = \frac{1}{4}\nu n_S \qquad (3.7)$$

is valid. However, in reality there is a mixture of sizes ν, and cluster products leak from and into observed regions. Figure 3.17 shows $4d_S^2(n_F)/n_S$ plotted versus n_S at 200 and 900 GeV. The data points are preliminary. Event generator curves are shown for the three average cluster sizes mentioned above. In general the data points fall in between the $\langle\nu\rangle$=1.8 and $\langle\nu\rangle$=2.7 lines.

Short range correlations in the form of the two-particle correlation function $C_n(\eta_1,\eta_2)$ versus the rapidity difference between the two particles are shown in figure 3.18. One sees that the default value of the cluster size describes the data well.

To conclude, GENCL reproduces the observed particle correlations in pseudorapidity, although some parts could be improved (fig. 3.16). However, it is not clear what to change or tune. Besides the cluster size, one can e.g. change the dispersion of the cluster decay or/and the cluster decay width. It was also seen in section 3.1.5 that it is not enough to change only the cluster size (fig. 3.16) in order to tune the generator to the negative binomial parameter k. A detailed discussion of all these points is outside the scope of this article. A thorough discussion of long range correlations can be found in reference [44]. One should also note that to all data points in figures 3.16 and 3.17 a systematic error should be added, which is not included in the errors. The data are preliminary and the systematic error has not yet been estimated.

3.1.7 Photon production

In GENCL all photons come from decays of π^0:s, of which most are produced in the pion-clusters that simulate the known resonances. There are for example no so called direct photons, expected from leading order QCD processes and observed at the Collider [45]. The production cross-section for these is, however, several orders of magnitude smaller than that for hadronic jets.

UA5 has measured the average number of photons, $\langle n_\gamma \rangle$ as a function of the number of charged particles in $\bar{p}p$ events at $\sqrt{s}$=546 GeV [3,17,20], which has been used as input to the generator (eq. 2.12). The photon distribution in pseudorapidity has also been measured [17], and in figure 3.19 the output is compared to these data. In figure 3.20 the p_T distribution for the photons from GENCL is shown. Using the calorimeter of the UA5 detector [3] it is possible to estimate the central photon p_T-spectra. This has been done at $\sqrt{s}$=546 GeV for $|\eta|<0.9$ [46] and the result is compared with GENCL in figure 3.21, showing good agreement.

3.1.8 Local particle fluctuations in pseudorapidity, "spikes"

UA5 has looked for large particle fluctuations in pseudorapidity [47,48] in the following way: a narrow window in pseudorapidity was defined, typically of the order of 1/2 unit. For each event this window was slid from η=-5 to η=5, everywhere counting the number of charged particles falling inside the window. In this way events were looked for where the window at some place in η contained very many particles, so called "spikes". Figure 3.22 shows three typical "spike" events together with one Monte Carlo generated "spike".

Figure 3.23 shows the mean spike multiplicity as a function of the number of observed particles. Here the "spike" is defined to be the maximum number of particles found in a window of width 0.5. GENCL's output has been passed through the tracking Monte Carlo (sec. 5) to get a simulated number of observed particles. Data and Monte Carlo agree very well indeed. Also when one looks at extreme cases, e.g. the largest spike in all events with 40 observed particles, GENCL gives roughly the same spikes. Both for data and GENCL the particles in the spikes are uniformly distributed in φ, the azimuth angle.

It is random fluctuations in the cluster production, their positioning in rapidity and subsequent decays, that creates these spikes. Note that in GENCL two or more clusters can superimpose in η. No new physical effect is needed. The result is interesting because there is no explicit input to GENCL that makes these spikes. When the clustering is turned off (see app. B), most spikes, $\approx$90%, are still there, so the most important contribution to the spikes seems to be the random positioning in rapidity.

3.1.9 Local energy fluctuations, "jets"

We have studied another kind of fluctuation in GENCL by applying UA1:s jet-finding algorithm [41,49,50]. The events generated by GENCL were put through an analysis program simulating the geometry and energy resolution of UA1's calorimeter [50] and were then subjected to the jet-finding algorithm of UA1. We do not simulate the full UA1 detector. The $\eta\varphi$-space in $|\eta|<2.4$ was divided into 16×24=384 cells of size $\Delta\eta\cdot\Delta\varphi=0.3\times15^{\circ}$, the approximate size of UA1's hadronic calorimeter modules [49]. Particle energies were smeared with the energy resolution of the calorimeters [50]. For each event the transverse energy E_T for all cells was calculated as

$$E_T^{cell}=(\Sigma E_i)\cdot\sin(\theta^{cell}) \qquad (3.8)$$

where the sum is over all particles pointing to the cell. Any cell that has $E_T^{cell}>1.5$ GeV is called an initiator. The initiators are arranged in decreasing order. Smaller initiators are added (vector sum) together with the largest initiator within a distance of $R=\sqrt{(\Delta\eta^2+\Delta\varphi^2)}=1$. Finally cells

are added to the closest remaining initiator if the distance R<1. Thus one roughly adds (as a vector sum) all the particles' "energy vector" within a circle of radius one in the $\eta\varphi$-plane around the initiator. If the absolute value of the resulting vector is >5 GeV this is a "jet".

Like UA1 [41] we divide the events into two samples. "Jet events", containing all events where the algorithm finds at least one "jet" with its axis in the pseudorapidity region $|\eta|<1.5$ and the remainder, called "no-jet events". Only particles in $|\eta|<2.5$ are now considered.

We found that GENCL gives between half and two thirds as many low-E_T "jets" as UA1 has found [24,41]. In table 4 GENCL's output is compared with UA1's result. In about 20% of the jet events we find more than one jet in the $\eta\varphi$-acceptance of UA1, compared to 30% for data. All $\langle p_T \rangle$ from GENCL are a few percent larger than data in table 4, and this has to do with the tuning and systematic errors explained in sec. 3.1.4, but all trends are the same and generally the agreement with data is surprisingly good. The "jets" even look jet-like. Figure 3.24 shows the energy flow in pseudorapidity around the jet axis (the φ hemisphere opposite to the jet axis is not included) for data and GENCL at 900 GeV [24,40]. However, the E_T-spectrum of the generated "jets" falls faster than data (fig. 3.25).

UA1 has made scaled multiplicity distributions: $\langle n \rangle P(z)$ as a function of $z=n/\langle n \rangle$, for the jet and no-jet samples at 200, 350, 630 and 900 GeV [41]. They found the distributions to be independent of the c.m. energy, i.e. the multiplicity distributions KNO-scale. Figure 3.26 shows the corresponding distributions for GENCL's jet and no-jet samples, as well as for all charged particles in $|\eta|<2.5$ at 200 and 900 GeV. The shaded areas show where UA1's datapoints are. We do not find scaling for the generated events. The scale breaking is not large, however, and it is not certain that UA1 would see such a small difference.

Lately it has been shown that the mini-jets show Rutherford scattering [51], strongly suggesting that the mini-jets originate from parton-parton scattering. This is not reproduced in GENCL. If θ^* is the scattering angle in the c.m.s. of two jets, one rather gets a flat $\cos\theta^*$ distribution instead of the $(1-\cos\theta^*)^{-2}$ behaviour as one expects from Rutherford scattering.

In order to understand the "jet" generation, the power law part of the p_T-spectrum was turned off and all clusters were given transverse momenta from an exponential distribution in the transverse mass, tuned such that $\langle p_T \rangle$ was the same as before. The number of "jet events" then decreased by one third, so most "jets" were still there. An important factor in the jet generation seems to be fluctuations of particles in the $\eta\varphi$-plane. A "jet" contains on the average 12.6 (10.9) particles at 900 (200) GeV, whereas an average circle with radius $R=\sqrt{(\Delta\eta^2+\Delta\varphi^2)}=1$ in $|\eta|<2.5$ contains only 4.1 (3.1) particles. It is not the clustering of particles that makes the fluctuations. Turning off all clustering (see app. B) does not change the number of "jets" or the number of the particles in "jets" appreciably. On the other hand initiators contain only 1.4 (1.3) particles, indicating that the hard p_T is important for making these. To see the importance of the

initiators we searched for "jets" around every cell (i.e. all cells were regarded as initiators). In this case we found twice as many "jet events" as ordinarily, but the "jet-structure" in figure 3.24 was lost.

To summarize this subsection we conclude that although we do not include hard scattering explicitly, the main features of jets are found with GENCL and therefore taken into account in the correction of the UA5 data. A further improvement of the generator, though, might need a jet-component. Two-component models have been suggested, e.g. in reference [52].

3.2 DIFFRACTIVE EVENTS

UA5 has done some analyses on single diffractive processes [12]. In particular we have estimated the SD cross-section at Collider energies. This is done by using our trigger rates, where the trigger efficiencies have been determined by Monte Carlo. Thus it is important that DIFFR correctly describes SD processes and especially the charged particle distribution in pseudorapidity, which determines the trigger efficiency. We now compare DIFFR's output with recent data from UA4 [29,30,53] and UA5 [12].

The mass-spectrum for the diffractive states is randomized from a $1/M^2$ distribution independent of the four-momentum transfer squared, -t and therefore agrees well with data [30]. More interesting is the η-distribution of charged particles of the decaying state. By varying the parameter p_c (see sec. 2.2) we make this distribution less or more isotropic. An isotropic distribution gives a more narrow pseudorapidity distribution. In figures 3.27 and 3.28 DIFFR:s output for the values p_c=0.3, 0.4 and 0.5 GeV/c, resulting in an average p_T of 0.29, 0.38 and 0.45 GeV/c, respectively, is compared to data [29]. Figure 3.27 shows the particle density at the diffractive state's kinematical central value, $\bar{\eta}=\ln(M/\sqrt{s})$, where M is the mass of the state. The change of slope around M=5 GeV shows where the clusters decaymode changes from isotropic to cylindrical. It is seen that $\langle p_T \rangle$=0.38 GeV/c (p_c=0.4 GeV/c) gives the best description of the data. Figure 3.28 shows $dn/d\eta$ in the mass-ranges 7 - 50 GeV (a) and 72 - 90 GeV (b). All three values of p_c are in fair agreement with data, and one can also see how the distribution gets more isotropic, i.e. narrower, when p_c is increased. Figure 3.29 shows the p_T-distribution that DIFFR gives for the charged particles from the decaying state, when using p_c=0.4 GeV/c. There are no data on p_T-distributions available.

The recent UA5 data at $\sqrt{s}$=900 GeV can also be used to test the DIFFR event generator. The sample of events where the UA5 detector gave a trigger in only one arm (fig. 1.1) are supposed to be mainly single diffractive, but also contain some low multiplicity non-single diffractive events. Thus to simulate these events one needs a combination of GENCL and DIFFR. Figure 3.30 shows the pseudorapidity distribution of the detected particles in the 1-arm triggered events compared to a mixture of GENCL and DIFFR, where the outputs of the generators have been subject to the same trigger condition as data. These are uncorrected data and the Monte Carlo curves are from full simulations with tracking etc. (see sec. 4). There are no entries (almost) for $\eta<-2.0$, since in that case we would have had a two arm trigger instead of the

one arm trigger. Three curves where $\langle p_T \rangle$=0.35, 0.45 and 0.55 GeV/c[§] are shown. Here $\langle p_T \rangle$=0.45 GeV/c seems to agree best with data, slightly larger than the value preferred in figure 3.27. The reason for this could be that in figure 3.27 no consideration has been given to the non single diffractive background, which also is expected to be larger at 546 GeV than at 900 GeV.

Figure 3.31 shows for three multiplicity intervals of the 1-arm trigger events the width of the pseudorapidity distribution, σ_η, defined as

$$\sigma_\eta = \left[\frac{1}{n_{obs}} \sum_{i=1}^{n_{obs}} (\eta_i - \langle \eta \rangle)^2 \right]^{1/2} \qquad (3.9)$$

where n_{obs} is the number of observed particles. The shaded areas are the GENCL contributions, the solid lines are DIFFR with $\langle p_T \rangle$=0.45 GeV/c (p_c=0.5 GeV/c) and the dashed lines are DIFFR with clusters always decaying isotropically ($p_c \to \infty$, $\langle p_T \rangle$=1.5 GeV/c). Clearly the latter case is ruled out by data. The agreement with data in figures 3.30 and 3.31, is good enough to give support for the event generators, especially since the relative sizes of the mixture is fixed to the observed SD- and NSD-cross-sections [2,18].

§ Figure 3.30 is from reference [12] where p_c was tuned so to achieve these values of $\langle p_T \rangle$.

4. SIMULATION OF THE UA5 DETECTOR

In order to use these event generators to understand and correct the UA5 data, we need to simulate how the detector would respond to any event. Firstly this involves tracking particles through the material of the detector, allowing for scattering, interactions and decays. Then the precise measurements of the event made using the detector and analysis system must be carefully simulated. For early runs of UA5 we used a Monte-Carlo tracking program written specifically for the UA5 application [54]. Lately we have changed to using the powerful CERN Monte-Carlo system GEANT [55], which is used by many other HEP experiments.

The GEANT package provides a flexible method for specifying the geometry of a detector using standard shapes. The user can input simulated vertices and tracks to GEANT, and they will be tracked through the materials defined, allowing for decays, multiple scattering and interactions. The GEANT routines for electromagnetic interactions have been extensively checked against the EGS program [56], and interfaces to several hadronic interaction packages have been provided, of which GHEISHA [57] has been preferred for the present application. As tracking proceeds the user is given the opportunity to store information as particles cross sensitive parts of the detector, from which the detector response may be simulated at the end of the event. GEANT also provides a range of graphics facilities to display the simulated geometry and tracks.

4.1 APPLICATION OF GEANT TO UA5

The geometry of the UA5 detector (fig. 1.1, [3]) can be adequately simulated with a small subset of the GEANT standard shapes; just rectangular boxes, and cylindrical tubes or segments of them are required. For purposes of simulation the UA5 detector was divided into six units:-

i) Beam pipe. The beryllium beam pipe is composed of segments of cylindrical tubes joined to form an approximately elliptical tube. This geometry is easily simulated by GEANT, together with aluminium flanges connecting segments of pipe, and clamps and support bars.

ii) Streamer chambers. These are simulated as boxes of gas (90% Ne/10% He) enclosed by thin mylar walls. Also included are the surrounding aluminium Faraday cage and corona guard ring.

iii) Trigger hodoscopes. These are simulated as boxes or tube segments of plastic scintillator.

iv) Calorimeter. The calorimeter consists of lead and iron plates interspersed with scintillation counters. The geometry is straightforwardly simulated using rectangular boxes.

v) Photon converter. This is an aluminium box containing lead sheets which was placed between the beam pipe and the upper streamer chamber for part of the run. Its supporting rails are also simulated.

vi) A part of the streamer chamber support structure could affect particles hitting the calorimeter, and was therefore simulated.

Data cards were used to control which geometrical units were included in the simulation. The precise geometrical configuration was contingent on the units selected; thus the position of the upper streamer chamber was selected depending on whether the photon converter was enabled. Figure 4.1 shows a GEANT drawing of the simulated UA5 detector for comparison with fig. 1.1.

The interface of the UA5 event generators described above to GEANT was almost trivial. A realistic primary vertex distribution was simulated (using parameters controlled by user data cards). Then the mass codes used by the event generator were converted to the GEANT convention, and their 4-vectors supplied to GEANT.

The GHEISHA package was used for secondary hadronic interactions, since this seemed to give the best simulation of calorimeter data, and of hadronic interactions seen in the streamer chambers. The user has to select cutoffs below which tracking is not performed and secondary particles are not generated. These cuttoffs were generally taken to be 10 MeV for hadrons, and 0.5 MeV (kinetic energy) for electrons and photons. Higher cuts gave less satisfactory results for the calorimeter.

Information regarding the sensitive detectors (streamer chambers, trigger counters and calorimeter) is stored at tracking time. For the streamer chambers we store true space points along the trajectories of charged particles within the sensitive region. For the trigger counters we record any charged particle above 1 MeV which hits a module. In the calorimeter we store the ionization energy deposited in each scintillation counter when a charged particle traverses it.

4.2 SIMULATION OF DETECTOR RESPONSE

At the end of the tracking stage we simulate how the event would have appeared on our final data summary tapes. This involves first simulating the process of measuring the photographs of the streamer chamber. From the space points along a charged particle's trajectory in a streamer chamber we select approximately 10-12 space points to be "measured"; these always include the first and last points in the chamber, and the others are selected randomly by interpolation between the space points stored at tracking time. These points are projected through the optics of a camera on to the film plane, and random gaussian measurement errors (typically ~10 microns) applied. Points outside the field of view of the camera are rejected.

There are 3 cameras viewing each streamer chamber, any combination of which may be selected using data cards. Each camera sees two stereo views of the chamber, using a system of mirrors. Thus up to 6 views of each track may be simulated. For each view the measured start and end points are simulated, together with a different random choice of intermediate points. A real set of optical constants is used so as to give a realistic simulation. The simulated measurements are placed in the same type of data structure as real measurements.

Since the UA5 detector has no magnetic field the tracks seen on film are generally straight lines, after correcting for optical distortions. However, very low energy particles, generally electrons such as δ-rays, undergo significant multiple scattering in the streamer chamber gas, and are seen as "wiggly" tracks. Such tracks are not measured. In practice after measuring each track a single view straight line fit is performed, and if the r.m.s. deviation of the measurements from the fitted line exceeds some tolerance ($\sim 20\mu m$) the track is rejected. In the Monte-Carlo program the same procedure is followed; after each view is simulated for a track a single-view straight-line fit is carried out. If the track survives all these fits the "measurements" are passed to the standard UA5 geometrical reconstruction package to reconstruct the track parameters in space.

By this procedure an accurate modelling of the rejection procedure for "wiggly" tracks is achieved. We also make a good simulation of the errors on the reconstructed track parameters, allowing for different tracks being measured on different combinations of views. The final stage of the track simulation is to process the reconstructed tracks through the standard UA5 vertex finding procedure [3].

The simulation of the trigger counters is very simple. Although pulse heights and times are recorded for each module, this information is not used in

normal event analysis. We therefore just record which modules were hit by charged particles in the Monte-Carlo, and store this information in the same format as for data.

The UA5 calorimeter has been calibrated in a test beam. The first stage in analysis of the data, after pedestal subtraction, is to convert the pulse heights from the scintillation counters into equivalent particles (e.p.). One e.p. is the signal in a counter (by counter we mean a group of scintillators in general) due to the passage of a minimum ionizing particle (determined using muons from cosmic rays or a test beam). An analogous procedure is followed in the Monte-Carlo. Muons are passed through the calorimeter to determine the energy deposited in each counter. These provide factors which are used to scale the energy deposition in each counter in simulation of full events.

The signal in each counter is finally smeared, to allow for the effects of photoelectron statistics in the photomultiplier. A further source of smearing, fluctuations in energy deposition, is negligible in comparison, since a very low δ-ray threshold (0.5 MeV) is used. The calorimeter information (e.p.s in each counter) is stored in the same banks as used for data. We also store additional information about the particles incident on the calorimeter, for use in subsequent analysis.

4.3 PERFORMANCE OF THE TRACKING MONTE-CARLO

The program, consisting of interfaces to event generators, definition of geometry through GEANT calls, control of tracking and simulation of detector response, consists of ~2500 lines of FORTRAN code. Execution time for a typical 900 GeV $\bar{p}p$ event (~35 charged primary particles and a similar number of neutrals) is ~70 sec on a VAX 780, including geometric reconstruction and vertex finding. About half this time is spent in simulating and reconstructing streamer chamber tracks. The program may be run without film simulation, i.e. "electronics event" only, at about twice the speed. The program may be used for other special purposes, for example single particles may be generated just in front of the calorimeter to compare with test beam data, or events consisting only of strange particles (e.g. K^0_S, Λ, Ξ) may be generated for the determination of detection efficiencies.

Many checks of the simulation have been made against the data, of which two are shown here in illustration. It is important to simulate secondary interactions correctly. Figure 4.2 shows the longitudinal entry coordinates of observed tracks for data (solid) and Monte-Carlo (dashed). Figure 4.2(a) is for all tracks which point within 5 cm of the primary vertex (of which ~80% are true primary particles), and fig. 4.2(b) is for all non-pointing tracks (all coming from secondary interactions, particularly hadronic showers). Clearly the

normalization and shape of the data and simulation agree well. The peaks in fig. 4.2(b) reflect the presence of aluminium flanges which connect sections of the beryllium beam pipe.

The measurement errors on tracks, and their correlations, are complicated and difficult to simulate without the full measurement simulation outlined above. Tracks in different regions of the chambers are viewed by different combinations of cameras, or sometimes different portions of a track are seen by different cameras. Figure 4.3 shows some of the correlation coefficients between various measured quantities, between the azimuthal angle φ about the x-axis and the dip angle λ relative to the yz-plane (see fig. 4.1), and between φ and the longitudinal (z) coordinate of a reference point on the track, chosen to be at the track's mid-point. Figures 4.3(a) and (b) are for tracks in the region $2.5<\eta<3.5$ ($\eta=-\ln(\tan \theta/2)$) measured on the two stereo views of a main camera[§]. Figures 4.3(c) and (d) refer to tracks with $-1<\eta<0$ measured with two views of a main camera and two views of a supplementary camera, while figs. 4.3(e) and (f) correspond to tracks in the same rapidity range measured on two views of each of two main cameras. We see that the complicated variation of the correlations with track angle and cameras used is well reproduced by the Monte-Carlo.

§ Footnote: The main cameras, situated near the ends of the chambers, see fig. 1.1, view slightly more than half of a chamber. The supplementary cameras view the whole of a chamber at a greater demagnification.

5. SUMMARY AND CONCLUSIONS

The UA5 Monte Carlo program has been described in detail. The basic ideas of the two event generators are quite simple: The non diffractive event generator GENCL is a cluster Monte Carlo, where clusters are generated, placed in phase space, energy and momentum are conserved and then the clusters decay isotropically. The diffractive event generator DIFFR selects independently masses for the diffractive states and four-momentum transfer squared, a mass dependent multiplicity is chosen and then the decay is isotropic for small masses and cylindrical for larger masses, although it is not the value of the mass itself that determines the decay mode.

It was shown that the event generators agree very well with data. Much of it is of course because some of the data have been used as input, but also other data are surprisingly well reproduced. However, some parts can be improved, notably in GENCL where we have more data to compare with. The long range correlation (fig. 3.16) could be improved. This, and maybe multiplicity distributions in limited pseudorapidity intervals (which are quite well reproduced, but still could be improved) indicates that something with the cluster mechanism should be changed. The pseudorapidity distribution at $\sqrt{s}$=200 GeV does not agree as well with data as at 546 and 900 GeV (fig 3.2). This can be improved by letting the flat part in figure 2.2 decrease with increasing energy (eq. 3.1). Finally there are many "mini-jets" in GENCL (see sec. 3.1.8), but still 30-50% are missing. Maybe one has to put in explicitly a jet-component in GENCL to fix this. However, none of these discrepancies are serious and our conclusion is that we can trust corrections made to our data based upon GENCL and DIFFR. There is one place, though, where one needs to be careful, and that is when data are dependent on the trigger efficiencies. In GENCL these efficiencies depend on assumptions in the model which have not been possible to compare with data. Since different assumptions give different trigger efficiencies, the corrections will also be different. This has to be included in the systematic errors in the final data.

The event generators are ad hoc models built to reproduce data from low p_T, high energy $\bar{p}p$ collisions, and not to explain them. Nevertheless one can draw some conclusions of the underlying physical process by comparing data and event generator outputs when the inputs are changed. It is clear from e.g. particle correlations that particles in non diffractive events are created in clusters. We find that leading clusters are needed to describe pseudorapidity distributions in limited multiplicity intervals. Further, "spikes" and to a large extent "mini-jets" can be explained as ordinary fluctuations in the particle production mechanism. Finally, one saw in section 3.2 that heavier diffractive states decay according to a cylindrical phase space.

The non diffractive event generator GENCL describes $S\bar{p}pS$ Collider data from $\sqrt{s}$=200 to 900 GeV very well. Therefore it is natural to use GENCL at higher energies to get an idea of what particle collisions might look like at future accelerators. This has been done for SSC ($\sqrt{s}$=40 TeV), using the improvement of equation 3.1, and the results are presented in reference [58].

We have described how the UA5 detector and analysis system are simulated. The tracking through the detector is based upon the GEANT package and for secondary hadronic interactions the GHEISHA package is used. Comparisons between data and Monte Carlo show that the Monte Carlo reproduces the data well.

We conclude that the UA5 Monte Carlo program works well and gives good descriptions of reality, thus making it possible reliably to correct our data.

ACKNOWLEDGEMENT

We wish to thank K. Fialkowsi for helpful discussions. We acknowledge with thanks the financial support of the Brussel group by the National Foundation for Fundamental Research and the Inter-University Institute for Nuclear Sciences, of the Bonn group by the Bundesministerium für Wissenschaft und Forschung, of the Cambridge group by the UK Science and Engineering Research Council, and of the Stockholm group by the Swedish Natural Science Research Council.

APPENDIX A

This is a description of the method used to adjust cluster sizes such that the original Poisson distribution is not distorted.

One starts with a given number N (charged pions). Now the task is to divide this N into smaller numbers n_i (cluster sizes), which should follow a certain Poisson distribution. Numbers are drawn from this Poisson until the sum

$$S = \sum_{i=1}^{k} n_i \qquad (A.1)$$

is larger than or equal to N. If S=N the division is finished. If S>N the differences A=S-N and B=N-(S-n_k) are examined. Both A and B are ≥0, and n_k is the last generated number. If A<B, A numbers out of the k generated are randomly chosen and each of them is decreased by 1 (if n_i>0, otherwise another number is chosen). If B<A, B numbers out of the k-1 first generated numbers are randomly chosen and increased by 1. If A=B there is a 50% chance to increase A numbers and a 50% chance to decrease them.

APPENDIX B

This appendix describes how cluster sizes are changed in GENCL, and also how the clustering is turned off. Here $n_{\pi^\pm}$ denotes the number of charged pions in a pion cluster and n all charged particles in all central clusters (before π^0-decays so as to exclude Dalitz electrons).

To change the output average number of charged particles in the clusters, $\langle n \rangle$, the input parameter $\mu_{\pi^\pm}$, the Poisson parameter for generating the number of charged pions in the pion clusters, is changed. The default value of $\mu_{\pi^\pm}$ is 1.8, which gives $\langle n_{\pi^\pm} \rangle$=1.88 (due to some disregarded "empty clusters", see sec. 2.1.2) and $\langle n \rangle$=1.76. When $\mu_{\pi^\pm}$ is changed to 0.9 (3.6), $\langle n_{\pi^\pm} \rangle$ becomes 1.16 (3.52) and $\langle n \rangle$=1.21 (2.66). The reason for $\langle n_{\pi^\pm} \rangle$ =1.16 when $\mu_{\pi^\pm}$=0.9 is that there are then relatively more "empty clusters", and thus a greater increase of the average is made. However this effect has vanished when $\mu_{\pi^\pm}$=3.6 and instead a tiny suppression of large clusters occurs because occasionally there are not enough charged particles to make a big cluster. The average of all charged is less changed than $\langle n_{\pi^\pm} \rangle$ because the number and sizes of the pair clusters were not changed and they make up about one quarter of the central clusters (when $\mu_{\pi^\pm}$=1.8, see tab 1). Since the relative amount of π's decreases with $\sqrt{s}$, $\langle n \rangle$ decreases somewhat with $\sqrt{s}$ at fixed $\mu_{\pi^\pm}$. However, the difference is only significant for $\mu_{\pi^\pm}$=3.6, where $\langle n \rangle$=2.74 and 2.62 at 200 and 900 GeV respectively.

When the clustering is turned off all particles are placed singly and independently in "pre-rapidity" (see sec. 2.1.3.). In order to have no charged particle decays at all no K^*'s are produced either (the only decay left being that of π^0's). There is no excitation energy and hence no extra energy to give some particles a higher p_T. Transverse momentum is given to the single particles. The resulting $\langle p_T \rangle$ (in $|y|<2.5$) is 0.42 GeV/c, which one also can calculate from equations 2.16, 2.17 and 2.1, table 2, remembering that single π's always get p_T from eq. 2.16 and that clusters contain 3.0 particles on average. This is slightly less than the 0.44 GeV/c for the default version, the reason being that all pions here get transverse momenta from the exponential form (eq. 2.16) with an average of 0.333 GeV/c. Accordingly the pseudorapidity distribution is also almost the same as ordinarily. We can therefore conclude that the changes in the output when the clustering are turned off is primarily due to the "clustering effect".

REFERENCES

1. C.M.G. Lattes, Y. Fujimoto and S. Hasegawa, Phys. Rep. C 65(1980)151.
2. UA5-Col., G.J. Alner et al., Zeit. Phys. C32 (1986)153.
3. UA5-Col., G.J. Alner et al., to be submitted to Phys. Rep. C.
4. UA5-Col., G.J. Alner et al., Phys. Lett. 138B(1984)304.
5. UA5-Col., G.J. Alner et al., Phys. Lett. 160B(1985)193.
6. UA5-Col., G.J. Alner et al., Phys. Lett. 160B(1985)199.
7. UA5-Col., G.J. Alner et al., Phys. Lett. 167B(1986)476.
8. UA5-Col., K. Alpgård et al., Phys. Lett. 107B(1981)315.
9. UA5-Col., K. Alpgård et al., Phys. Lett. 121B(1983)209.
10. UA5-Col., K. Alpgård et al., Phys. Lett. 107B(1981)310.
11. UA5-Col., "Scaling of pseudorapidity distributions at c.m. energies up to 0.9 TeV", G.J. Alner et al., to appear in Zeit. Phys. C.
12. UA5-Col., "Diffraction dissociation at the CERN Pulsed Collider at c.m. energies of 900 and 200 GeV", R.E. Ansorge et al., to appear in Zeit. Phys. C.
13. UA5-Col., K. Alpgård et al., Phys. Lett. 123B(1983)361.
14. UA5-Col., K. Alpgård et al., Phys. Lett. 115B(1982)65.
15. UA5-Col., G.J. Alner et al., Phys. Lett. 151B(1985)309.
16. UA5-Col., G.J. Alner et al., Nucl. Phys. B 258(1985)505.
17. UA5-Col., K. Alpgård et al., Phys. Lett. 115B(1982)71.
18. UA5-Col., G.J. Alner et al., "An accelerator search at 900 GeV c.m. energy for the Centauro phenomenon", submitted to Phys. Lett. B.
19. AFS-Col., T. Åkesson et al., Nucl. Phys. B 203(1982)27.
20. Th. Müller, Ph.D. Thesis, Bonn University (1983), BONN-IR-83-21.
21. S. Uhlig et al., Nucl. Phys. B 132(1978)15.
22. R. Hagedorn, Rivista Nuovo Cimento 10(1983).
23. UA1-Col., G. Arnison et al., Phys. Lett. 118B(1982)167.
24. UA1-Col., G. Ciapetti, Proc. of "5th Topical Workshop on Proton Antiproton Collider Physics", St. Vincent, 1985. (Ed. M. Greco, Singapore, 1985.)
25. S. Jadach, Computer Phys. Com. 9(1975)297.
26. F. James, FOWL, A general MC p.s. program, CERN Program Lib., 1970, W505.
27. G. Alberi and G. Goggi, Phys. Rep. 74-1(1981).
28. K. Goulianos, Phys. Rep. 101-3(1983).
29. UA4-Col., D. Bernard et al., Phys. Lett. 166B(1986)459.
30. UA4-Col., M. Bozzo et al., Phys. Lett. 136B(1984)217.

31. M. Basile et al., Lett. Nuovo Cimento 38(1983)359.
32. J.W. Chapman et al., Phys Rev. Lett. 32(1974)257.
    P. Capilappi et al., Nucl. Phys. B 70(1974)1.
33. C.P. Ward et al., Nucl. Phys. B 153(1979)299.
    D.R. Ward et al., Nucl. Phys. B 141(1978)203.
34. F.C. Erné, Phys. Lett. 49B(1974)356.
35. M. Basile et al., Nuovo Cimento A 73(1983)329.
36. G.N. Fowler et al., Phys. Lett. 145B(1984)407.
    G.N. Fowler, R.M. Weiner and G. Wilk, Phys. ReV. Lett. 55(1985)173.
37. T.T. Chou and C.N. Yang, Phys. Rev. D 32(1985)1692.
38. J. Dias de Deus, Phys. Rev. D 32(1985)2334.
39. K. Jon-And, Ph.D. Thesis, Univ. of Stockholm (1985).
40. UA1-Col., F. Ceradini, presented at the International Europhysics Conference on High-Energy Physics, Bari, (July 1985).
41. UA1-Col., F. Ceradini, in Proc. of the International Europhysics Conference on High-Energy Physics, (Ed. L. Nitti and G. Preparata, Bari, 1985) p. 363.
42. B. Åsman, Ph.D. Thesis, Univ. of Stockholm (1985).
43. A. Bialas, I. Derado and L. Stodolsky, Phys. Lett. 156B(1985) 421.
44. G. Ekspong, in Proc. of the 3rd Topical Workshop on Proton-Antiproton Collider Physics, CERN yellow book 83-04 (1983) 112.
45. UA2-Col., J.A. Appel et al., Phys. Lett. 176B(1986) 239.
46. K.A. French, Ph.D. Thesis, Univ. of Cambridge.
47. P. Carlson, UA5-Collaboration, Invited talk at the IVth Int. Workshop on $\bar{p}p$ Collider Physics, Bern, 1984.
48. C. Geich-Gimbel, UA5-Collaboration, Invited talk at "The Quark Structure of Matter", Strasbourg-Karlsruhe, 1985.
49. UA1-Col., G. Arnison et al., Phys. Lett. 132B(1983)214.
50. UA1-Col., G. Arnison et al., Phys. Lett. 123B(1983)115
51. UA1-Col., A. DiCiaccio, presented at XVII International Symposium on Multiparticle Dynamics, Seewinkel, Austria (June 1986),
    F. Lacava, presented at VI th International Conference on Proton-Antiproton Physics, Aachen (June 1986).
52. G. Pancheri and Y. Srivastava, Proc. of "5th Topical Workshop on Proton Antiproton Collider Physics", St. Vincent, 1985. (Ed. M. Greco, Singapore, 1985.)
53. UA4-Col., pres. by V. Palladino, Workshop Chateau du Blois June 1985, CERN/EP 85-154.
54. A.R. Weidberg, Ph.D. Thesis, Univ. of Cambridge (1982), RAL report HEP-T-102.
55. R. Brun et al., "GEANT3 Users Guide", CERN DD/EE/84-1.
56. R.L. Ford and W.R. Nelson, SLAC-210 VC-32 (1978).
57. H. Fesefeldt, "Simulation of hadronic showers", PITHA-report RWTH Aachen.
58. D.R. Ward, "Low p_T Physics at the $Sp\bar{p}S$ Collider", invited talk at the Workshop on Physics Simulations at High Energies, Madison (May 1986).

TABLE CAPTIONS

Table 1: All cluster types occuring in GENCL.
The second column gives the resulting average number of each cluster type at $\sqrt{s}$=546 GeV and using R_{Δ}=0.5. These numbers are not input to the generator, but come out of it. The two last columns give the possible particle content of the clusters and the probability for its occurrence.
(When using R_{Δ}=0 the $\langle n_{clus} \rangle$ figures will increase by 3 %.)

Table 2: Particle rates, multiplicities in percent of total multiplicity and average momenta for all final state particles in GENCL at c.m. energies 200, 546 and 900 GeV. Where data are available they are given in brackets. Note that all GENCL numbers refer to the full phase space, whereas most data are for limited pseudorapidity intervals (see footnotes).

Table 3: Trigger efficiencies for the UA5 detector as given by GENCL for three different $|x_F|$ distributions for leading clusters at $\sqrt{s}$=546 GeV and for the $1-|x_F|$ suppressed distribution at $\sqrt{s}$=200 and 900 GeV. 1A and 2A denotes one arm and two arm trigger, respectively.

Table 4: "Minijet"-features of GENCL compared to UA1's data (in parantheses). The 200 and 900 GeV data are from ref. [41] and the 546 GeV data from ref. [24]. Fraction "jet events" is the percentage of events with at least one jet with its axis more than 30^{o} from the vertical.

TABLE 1

Cluster type	$\langle n_{clus} \rangle$ at 546 GeV	Particle content	Probability	
Leading cluster	2 (fixed)	p	0.25	
		n	0.25	
		Δ^{++}	0.25	
		Δ^{+}	0.167	
		Δ^{o}	0.0833	
Nucleon pair	1.4	$p\bar{p}$	0.25	
		$p\bar{n}$	0.25	
		$n\bar{p}$	0.25	
		$n\bar{n}$	0.25	
Hyperon pair	0.37	$\Lambda\bar{\Lambda}$	0.444	
		$\Lambda\bar{\Sigma}^{+}$	0.111	
		$\Lambda\bar{\Sigma}^{-}$	0.111	
		$\Sigma^{+}\bar{\Lambda}$	0.111	
		$\Sigma^{-}\bar{\Lambda}$	0.111	
		$\Sigma^{+}\bar{\Sigma}^{+}$	0.028	
		$\Sigma^{-}\bar{\Sigma}^{-}$	0.028	
		$\Sigma^{+}\bar{\Sigma}^{-}$	0.028	
		$\Sigma^{-}\bar{\Sigma}^{+}$	0.028	
Xi pair	0.094	$\Xi^{o}\bar{\Xi}^{o}$	0.25	
		$\Xi^{o}\bar{\Xi}^{-}$	0.25	
		$\Xi^{-}\bar{\Xi}^{o}$	0.25	
		$\Xi^{-}\bar{\Xi}^{-}$	0.25	
Kaon pair	2.4	$K^{+}K^{-}$	0.25	All K's are
		$K^{+}\bar{K}^{o}$	0.25	with 60%
		$K^{o}K^{-}$	0.25	probability
		$K^{o}\bar{K}^{o}$	0.25	K^{*}.
Pion cluster	11.8	One or several π:s.		
		$\pi^{\pm}$ from Poisson(1.8).		
		On average 1.2 π^{o}.		

TABLE 2

$\sqrt{s}$ (GeV)	200 (20 000 events)			546 (40 000 events)			900 (20 000 events)		
Particle	$\langle n \rangle$	Fraction (%)	$\langle p_T \rangle$ (GeV/c)	$\langle n \rangle$	Fraction (%)	$\langle p_T \rangle$ (GeV/c)	$\langle n \rangle$	Fraction (%)	$\langle p_T \rangle$ (GeV/c)
$\pi^{\pm}$	17.75	36.08	0.37	24.02(22.3)[4]	35.81	0.40	27.86	35.65	0.42
$K^{\pm}$	1.57	3.19	0.57	2.44(2.2)[1]	3.64	0.60(0.57)[1]	2.99	3.83	0.63
$K^0_S+K^0_L$	1.58	3.21	0.57	2.45(2.2)[1]	3.65	0.61(0.57)[1]	3.02	3.86	0.64
$p+\bar{p}$	1.84	3.74	0.53	2.44(2.5)[9]	3.64	0.62	2.79	3.57	0.68
$n+\bar{n}$	1.86	3.76	0.53	2.44(2.5)[9]	3.64	0.63	2.84	3.63	0.68
$\Sigma^{\pm}+\overline{\Sigma^{\pm}}$	0.15	0.30	0.61	0.25(0.25)[4]	0.37	0.67	0.33	0.42	0.71
$\Lambda+\bar{\Lambda}$	0.29	0.59	0.61	0.51(0.6)[2]	0.76	0.67(0.6)[2]	0.65	0.83	0.70
$\Xi^-+\Xi^0+\overline{\Xi^-}+\overline{\Xi^0}$	0.078	0.16	0.84	0.19(0.22)[2]	0.28	0.90(1.1)[3]	0.29	0.37	0.93
$e^{\pm}$	0.27	0.55	0.11	0.37	0.55	0.12	0.43	0.55	0.12
γ	23.81	48.39	0.20	31.96(31.5)[5]	47.64	0.21	36.95	47.28	0.22
all	49.20	100.0	0.31	67.08	100.0	0.34	78.15	100.0	0.36
all charged	21.62	43.94	0.40	29.62(29.1)[6]	44.16	0.43(0.42)[7]	34.55	44.21	0.46
	(21.4)[6]		(0.39)[8]				(34.6)[6]		(0.45)[8]

Footnotes:
[1] Ref [16].
[2] Ref [39].
[3] Ref [15].
[4] Ref [9], inferred value for $|\eta|<5$.
[5] Ref [9], measured value for $|\eta|<5$.
[6] Ref [7].
[7] Ref [23], $|y|<2.5$ and $0.3<p_T<10$ GeV/c
[8] Ref [40], $|\eta|<2.5$.
[9] Ref [9], inferred value for $|\eta|<5$, and assumed one leading proton and one leading neutron per event on average.

TABLE 3

$\sqrt{s}$ (GeV)	x_F-dist.	Trigger efficiency (%) 1A	2A	1A+2A
546	R_Δ=0.0	5.8	93.9	99.7
	R_Δ=0.5	6.1	93.5	99.6
	$1-\|x_F\|$, R_Δ=0.0	2.6	97.3	99.9
200	$1-\|x_F\|$, R_Δ=0.0	6.0	93.8	99.8
900	$1-\|x_F\|$, R_Δ=0.0	2.4	97.5	99.9

TABLE 4

$\sqrt{s}$ (GeV)	Fraction "jet events" (%)	$\langle n_{ch} \rangle$ no-jet	$\langle n_{ch} \rangle$ jet	$\langle p_T \rangle$ (GeV/c) no-jet	$\langle p_T \rangle$ (GeV/c) jet
200	3.0 (5.9)	13.0 (13.8±.7)	28.8±.6 (26.5±.2)	0.412 (0.383±.005)	0.507±.002 (0.474±.007)
546	7.9 (12)	14.3±.1 (15)	34.5±.5 (35)	0.439±.001 (0.480)	0.506±.001
900	12.1 (17.2)	14.5±.1 (15.9±.1)	35.5±.6 (32.9±.1)	0.456±.001 (0.411±.005)	0.525±.001 (0.516±.006)

FIGURE CAPTIONS

Fig. 1.1 The UA5 experimental layout.

Fig. 2.1 Schematic picture of a non diffractive (ND) event (a), a single diffractive (SD) event (b) and a double diffractive event (c). In b) and c) the arrows show the momenta, these are not geometrical pictures. In a) the variable η is shown.

Fig. 2.2 The probability density P(y') used to generated the "pre-rapidity" y'.

Fig. 3.1 Pseudorapidity distributions for charged particles at fixed multiplicities at c.m. energies 200 and 900 GeV. Data from ref [11].

Fig. 3.2 Inclusive pseudorapidity distributions for charged particles at $\sqrt{s}$= 200, 546 and 900 GeV. Data from ref. [11].

Fig. 3.3 Rapidity distributions compared with pseudorapidity distributions for the same set of charged particles generated at $\sqrt{s}$=200 and 900 GeV. y_{beam} is the rapidity of the beam particle, which is the largest rapidity a leading baryon can have. The shaded areas show the contributions from the leading protons.

Fig. 3.4 Pseudorapidity distributions in four limited multiplicity intervals at $\sqrt{s}$=546 GeV. Normal GENCL and two modifications of it (described in the text) are compared to data [3].

Fig. 3.5 Feynman-x distribution for leading baryons using three different options in GENCL.

Fig. 3.6 The trigger efficiency in one trigger arm as a function of x_F of the leading baryon on the same side.

Fig. 3.7 The average x_F of one leading baryon as a function of x_F of the other leading baryon.

Fig. 3.8 Inelasticity (eq. 3.2) distribution as given by GENCL at c.m. energy 546 GeV.

Fig. 3.9 $\langle p_T \rangle$ vs. n_{ch} in the range $|\eta|<2.5$ at $\sqrt{s}$=200 and 900 GeV. Data from ref. [41].

Fig. 3.10 $\langle p_T \rangle$ vs. rapidity (full line) and pseudorapidity (dashed line) for all charged particles as given by GENCL at $\sqrt{s}$=546 GeV. The dotted line shows $\langle p_T \rangle$ vs. rapidity for charged pions only.

Fig. 3.11 Transverse momentum distribution for charged particles in $|y|<2.5$ at $\sqrt{s}$=546 GeV. The dashed curve is a very good fit to data [23]. Shaded areas show the size of the errors on data.

Fig. 3.12 Transverse momentum distribution for kaons in $|y|<2.5$. Data from ref. [16]. The dashed curve gives the same distribution in $|\eta|<2.5$.

Fig. 3.13 K/π ratio as a function of transverse momentum. Data from ref. [16].

Fig. 3.14 Charged multiplicity distributions in the regions $|\eta|<0.2$, 0.5, 1.5 and 3.0 plotted as $\langle n \rangle P(z)$ vs. $z=n/\langle n \rangle$. Data from ref. [5].

Fig. 3.15 The negative binomial parameter k as a function of η_c (see text). GENCL outputs with three different clustersizes $\langle \nu \rangle$ and with no clusters, are compared to data [5].

Fig. 3.16 Forward-backward correlation strength b as a function of $\sqrt{s}$ in the ranges $0<|\eta|<4$ (a) and $1<|\eta|<4$ (b). The three curves corresponds to three different average numbers of charged particles, $\langle \nu \rangle$, in the clusters of GENCL. The solid line is the default version.

Fig. 3.17 The dispersion $d_S(n_F)$ plotted as $4d_S^2(n_F)/n_S$ as a function of $n_S(=n_F+n_B)$ at 900 GeV (a and b) and 200 GeV (c and d). In a) and c) the regions are $1<|\eta|<4$ and in b) and d) $1<|\eta|<2$.

Fig. 3.18 The two-particle correlation function $C_n(\eta_1,\eta_2)$, for $20\leq n\leq 22$, as a function of the pseudorapidity difference $\eta_1-\eta_2$. The curves are for $\langle \nu \rangle$=1.1 (dash-dotted), 1.8 (solid) and 2.7 (dashed).

Fig. 3.19 Pseudorapidity distribution of photons at $\sqrt{s}$=546 GeV. Data from [14]. The curve is from GENCL.

Fig. 3.20 The transverse momentum distributions of photons at $\sqrt{s}$=200, 546 and 900 GeV as given by GENCL.

Fig. 3.21 The transverse momentum distribution for central photons ($|\eta|<0.9$) at $\sqrt{s}$=546 GeV. Data from ref. [46].

Fig. 3.22 Three examples of "spikes" in data (in black) and one example from an event generated by GENCL. The size of the window is 1/4 unit of pseudorapidity.

Fig. 3.23 Mean spike multiplicity as a function of observed multiplicity.

Fig. 3.24 Energy density in pseudorapidity around the jet axis. Only the φ hemisphere with the jet axis in the middle. Data from [40].

Fig. 3.25 The distribution of the transverse energy, E_T, at $\sqrt{s}$=546 GeV. Data from [24].

Fig. 3.26 Multiplicity distributions in $|\eta|<2.5$ for "jet events" (a), "no-jet events" (b) and all events (c) at $\sqrt{s}$=200 and 900 GeV. UA1's data [41] are in the shaded areas.

Fig. 3.27 Charged particle density in pseudorapidity near the diffractive clusters kinematical centre.

Fig. 3.28 Pseudorapidity distributions of charged particles from the decayed diffractive states with masses of 7 to 50 GeV (a) and 72 to 90 GeV (b). These have on average 8.5 and 15.3 charged particles (in DIFFR). The curves are from DIFFR with the parameter p_c=0.3 (dashed), 0.4 (solid) and 0.5 GeV/c (dash-dotted) giving $\langle p_T \rangle$=0.29, 0.38 and 0.45 GeV/c, respectively.

Fig. 3.29 Transverse momentum distribution of charged particles in three different massregions with <M>=3 GeV (dashed), <M>=20 GeV (full curve) and <M>=80 GeV (dash-dotted curve), as given by DIFFR.

Fig. 3.30 Pseudorapidity distribution of detected particles in 1-arm trigger events. The shaded area is the GENCL contribution. The curves are for three different values of the DIFFR parameter p_c.

Fig. 3.31 Distribution of the pseudorapidity distribution widths for 1-arm trigger events with 2-4 observed particles (a), 5-9 particles (b) and 9-12 particles (c). Shaded areas are GENCL contributions, solid curves DIFFR with $\langle p_T \rangle$=0.45 GeV/c (p_c=0.5 GeV/c) and dashed curves DIFFR with only isotropic decays.

Fig. 4.1 GEANT drawing of the simulated UA5 detector. Compare figure 1.1.

Fig. 4.2 Longitudinal (beam-direction) entry coordinates of observed tracks for data (solid) and Monte-Carlo (dashed), for all tracks which point within 5 cm of the primary vertex (a) and for all non-pointing tracks (b).

Fig. 4.3 Correlation coefficient ϱ between the azimuthal angle φ and the dip angle λ in the region $2.5<\eta<3.5$ (a), between φ and z (see text) in the same region (b), between φ and λ in the region $-1<\eta<0$ for the upper and lower streamer chambers (c) and (e) and $\varrho(\varphi,z)$ in the same region and for the two chambers (d) and (f).

SCHEMATIC LAYOUT OF THE STREAMER CHAMBER SYSTEM

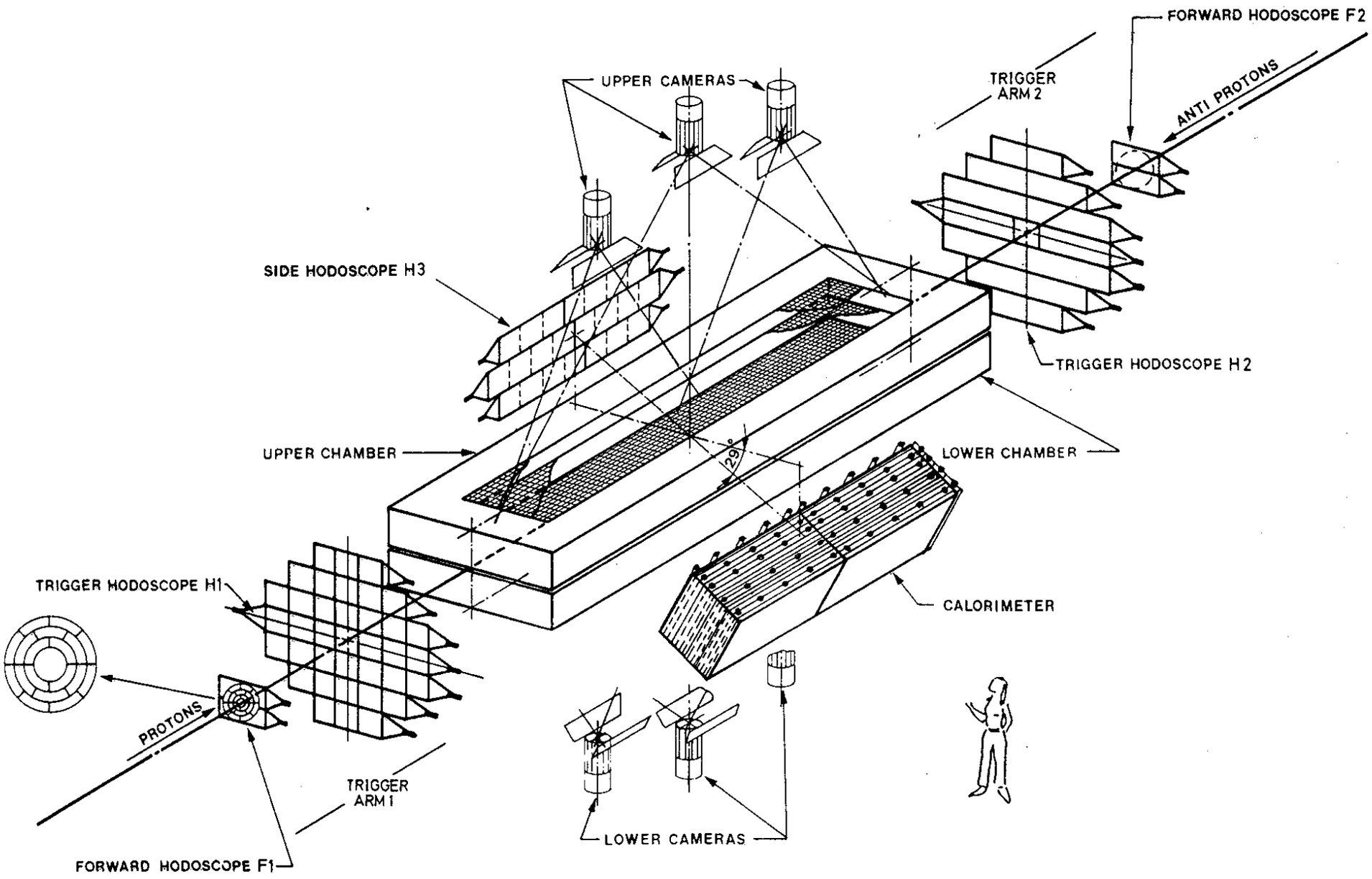

Fig. 1.1

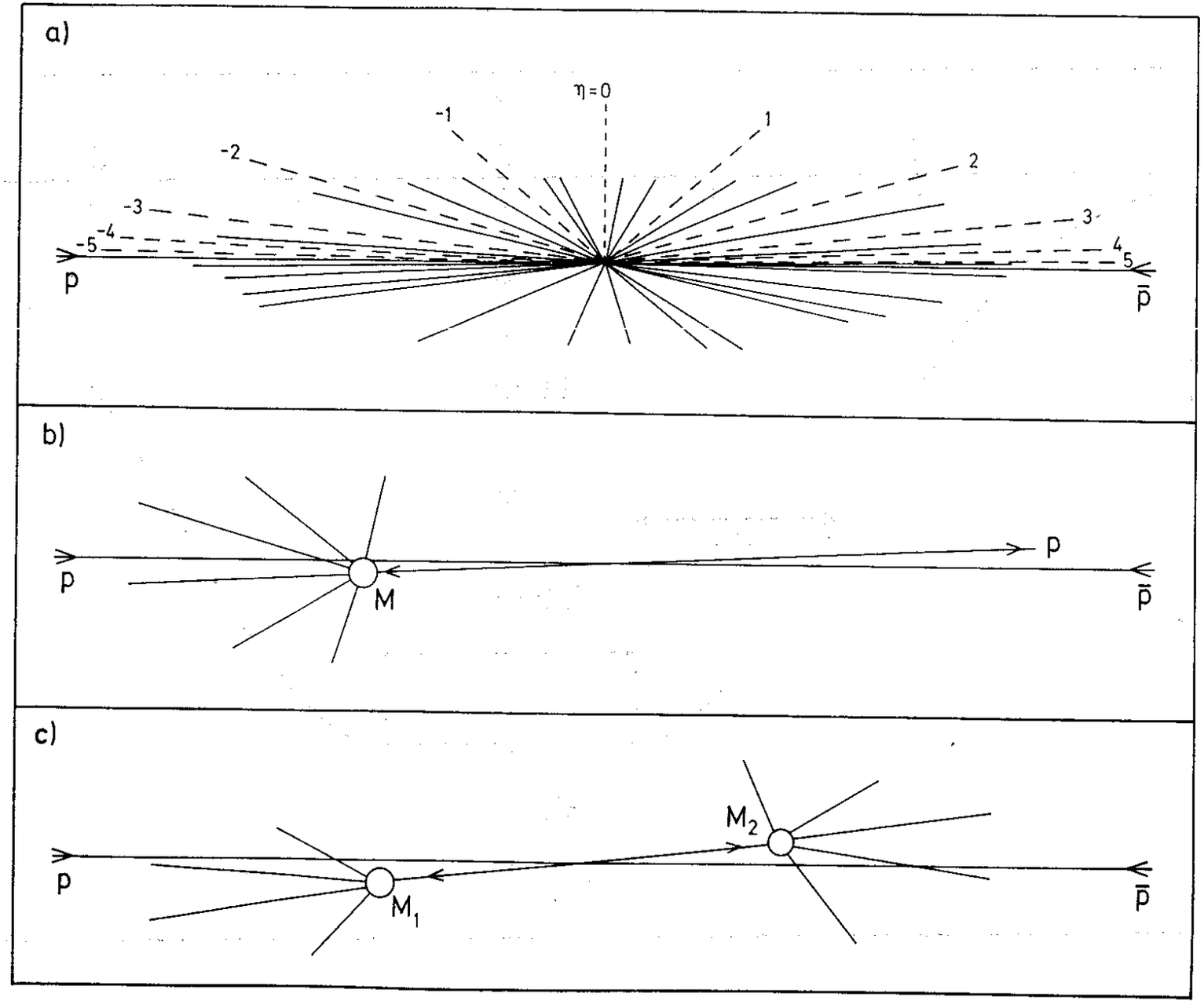

Fig. 2.1

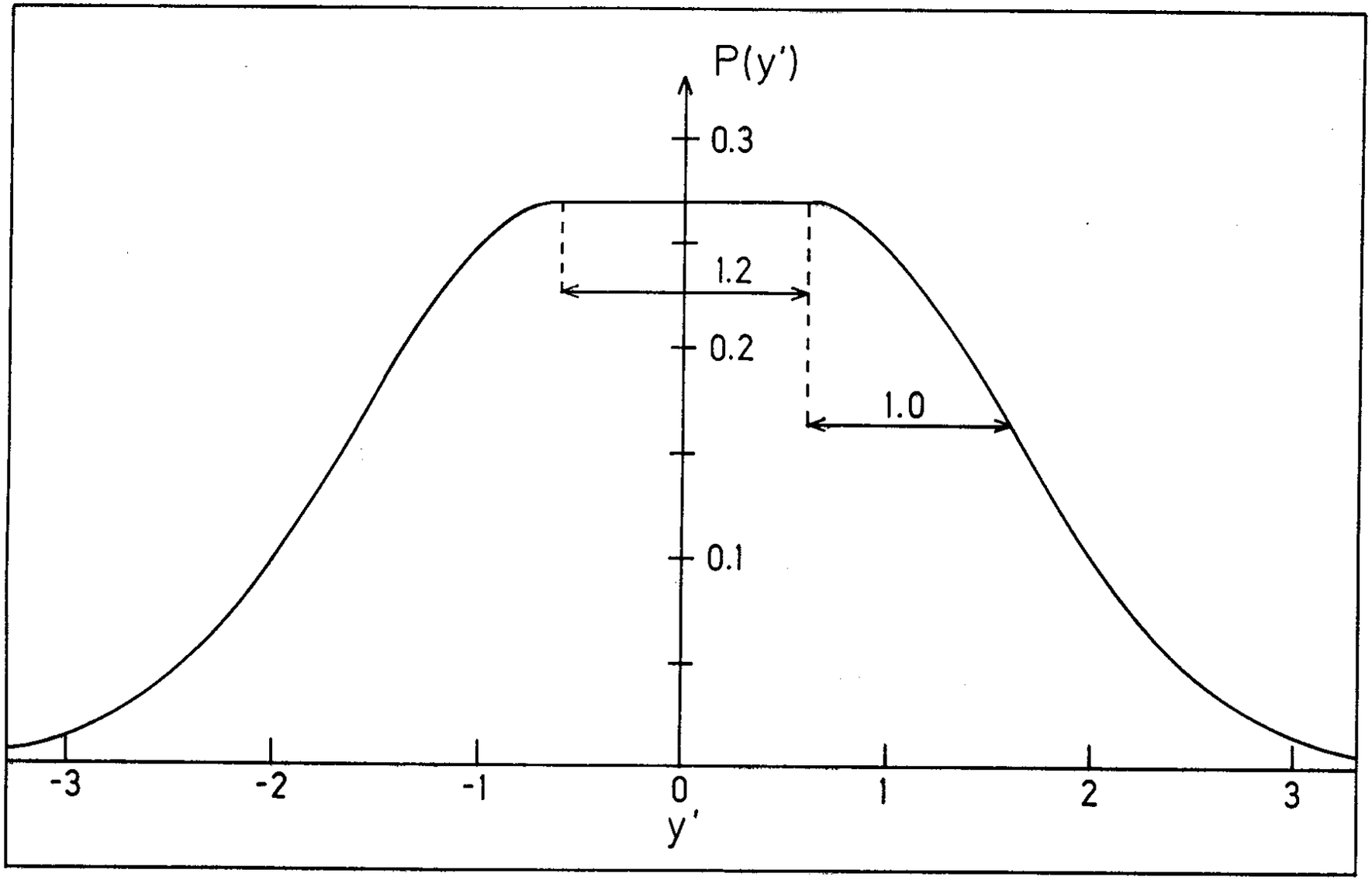

Fig. 2.2

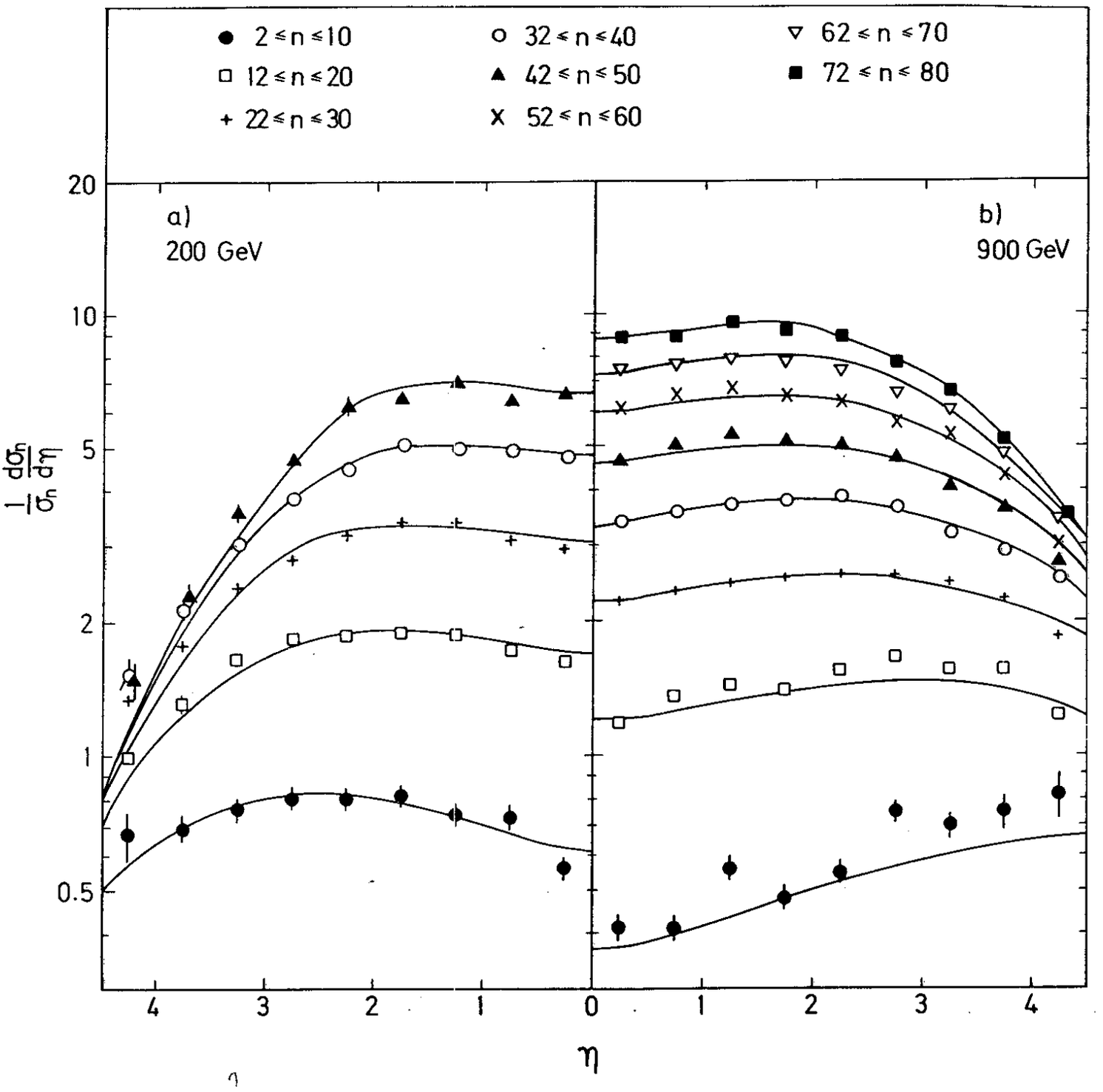
● 2 ≤ n ≤ 10
□ 12 ≤ n ≤ 20
+ 22 ≤ n ≤ 30
○ 32 ≤ n ≤ 40
▲ 42 ≤ n ≤ 50
X 52 ≤ n ≤ 60
▽ 62 ≤ n ≤ 70
■ 72 ≤ n ≤ 80
a)
200 GeV
b)
900 GeV
$\frac{1}{\sigma_n}\frac{d\sigma_n}{d\eta}$
20
10
5
2
1
0.5
4
3
2
1
0
1
2
3
4
η

Fig. 3.1

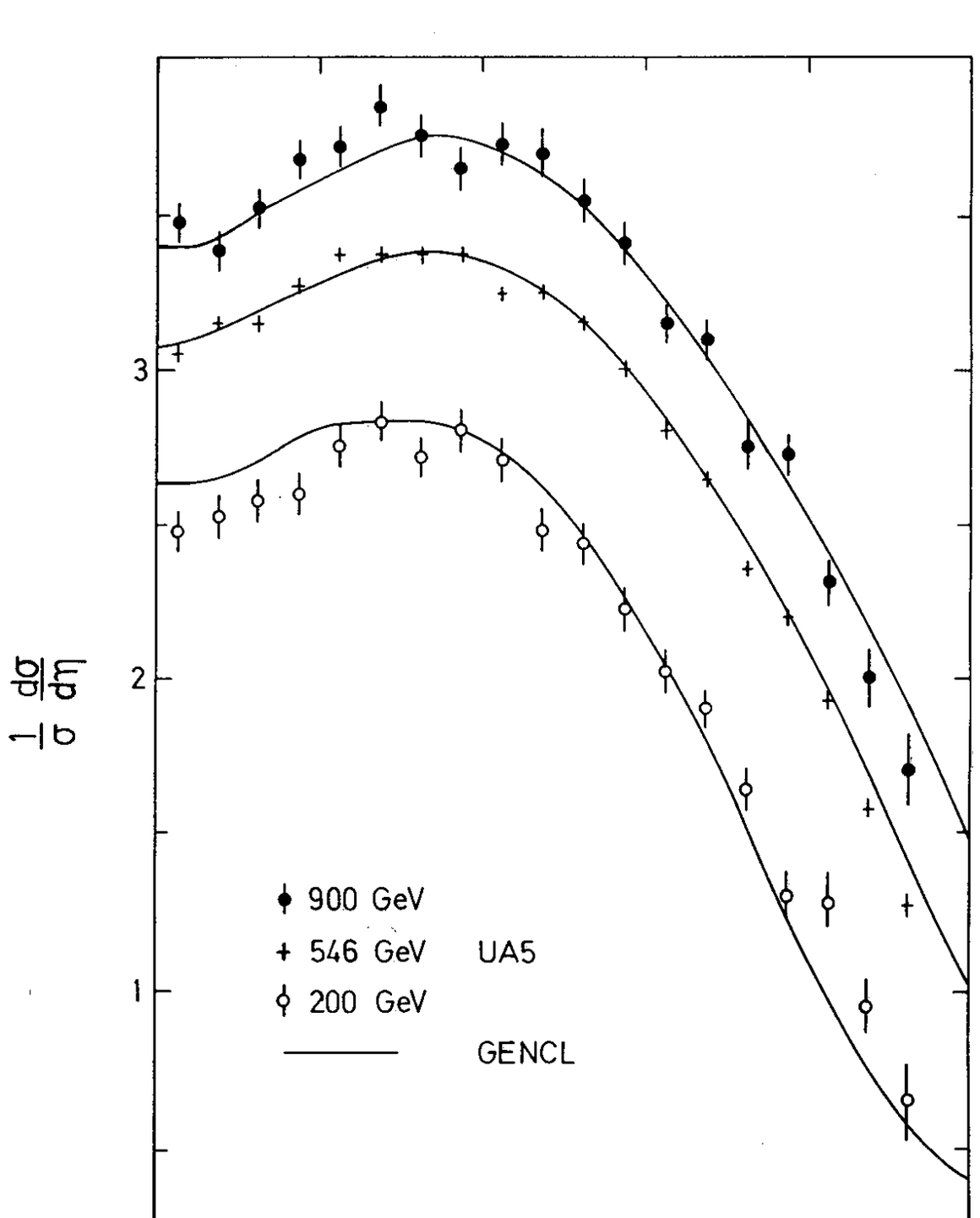
$\frac{1}{\sigma}\frac{d\sigma}{d\eta}$
3
2
1
0
1
2
3
4
5
η
900 GeV
546 GeV
200 GeV
UA5
GENCL

Fig. 3.2

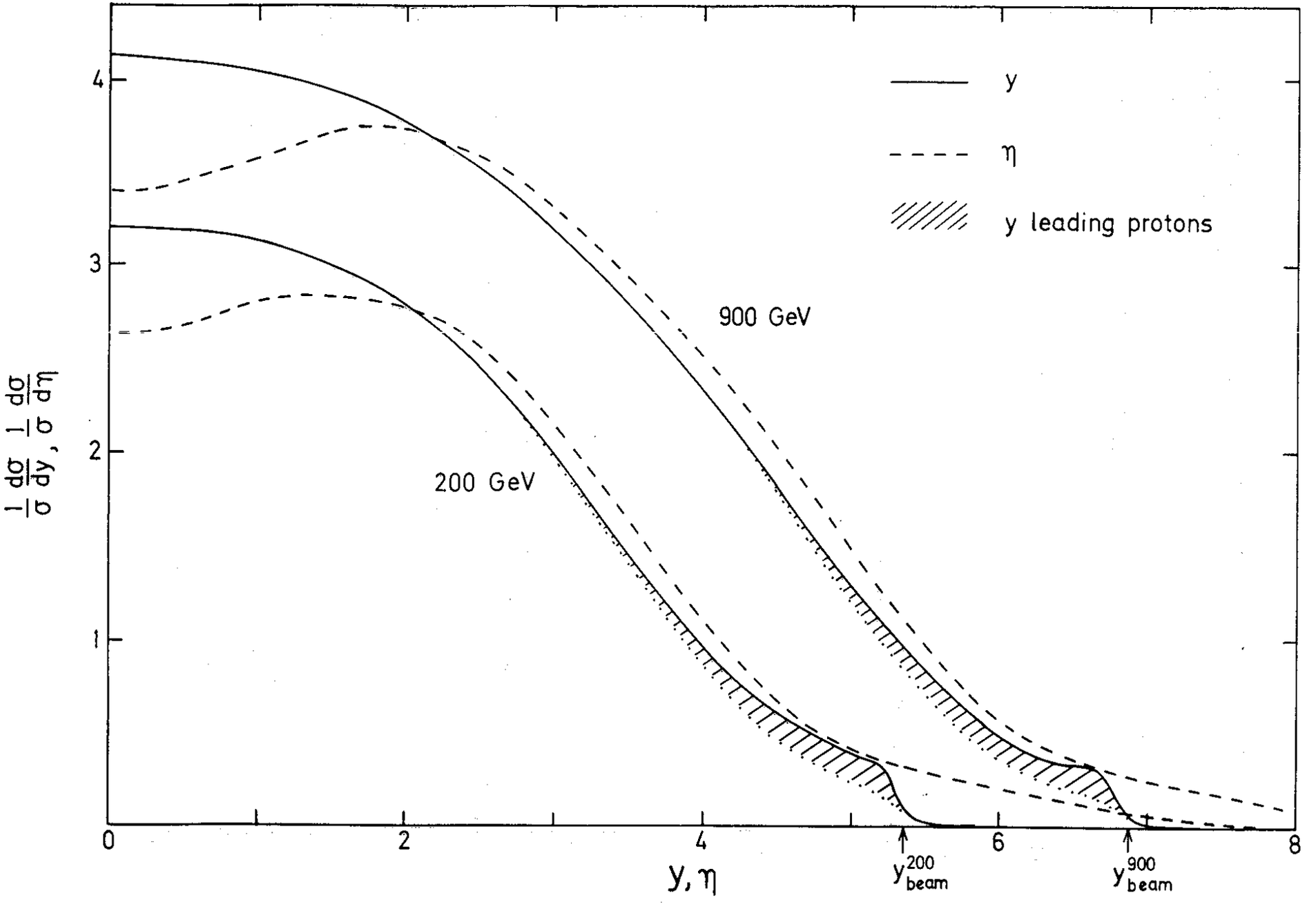
y
η
y leading protons
900 GeV
200 GeV
$\frac{1}{\sigma}\frac{d\sigma}{dy}, \frac{1}{\sigma}\frac{d\sigma}{d\eta}$
y, η
y^{200}_{beam}
y^{900}_{beam}
0
2
4
6
8
1
2
3
4

Fig. 3.3

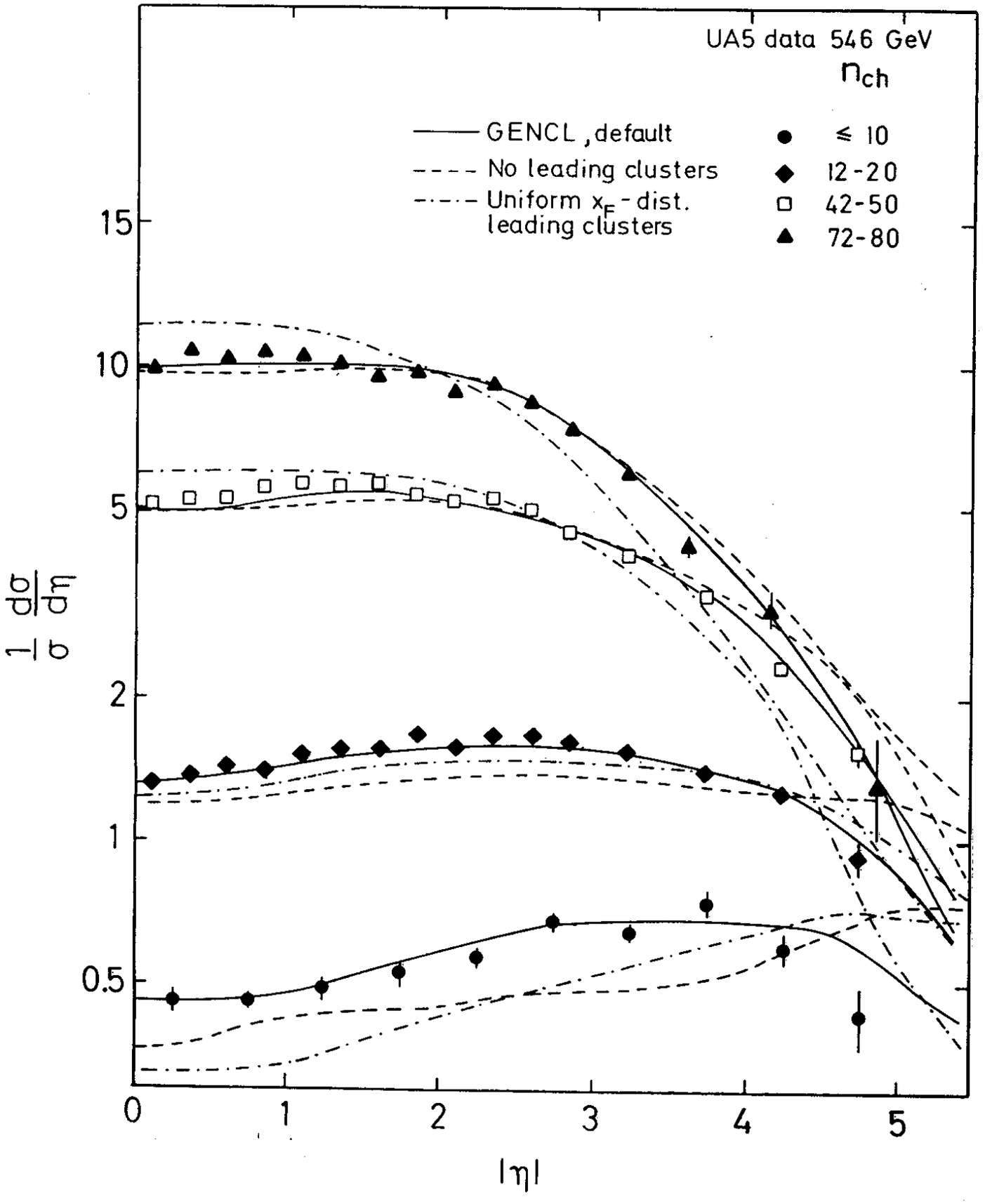
UA5 data 546 GeV
n_{ch}
GENCL, default
No leading clusters
Uniform x_F - dist. leading clusters
≤ 10
12-20
42-50
72-80
$\frac{1}{\sigma}\frac{d\sigma}{d\eta}$
$|\eta|$
15
10
5
2
1
0.5
0
1
2
3
4
5

Fig. 3.4

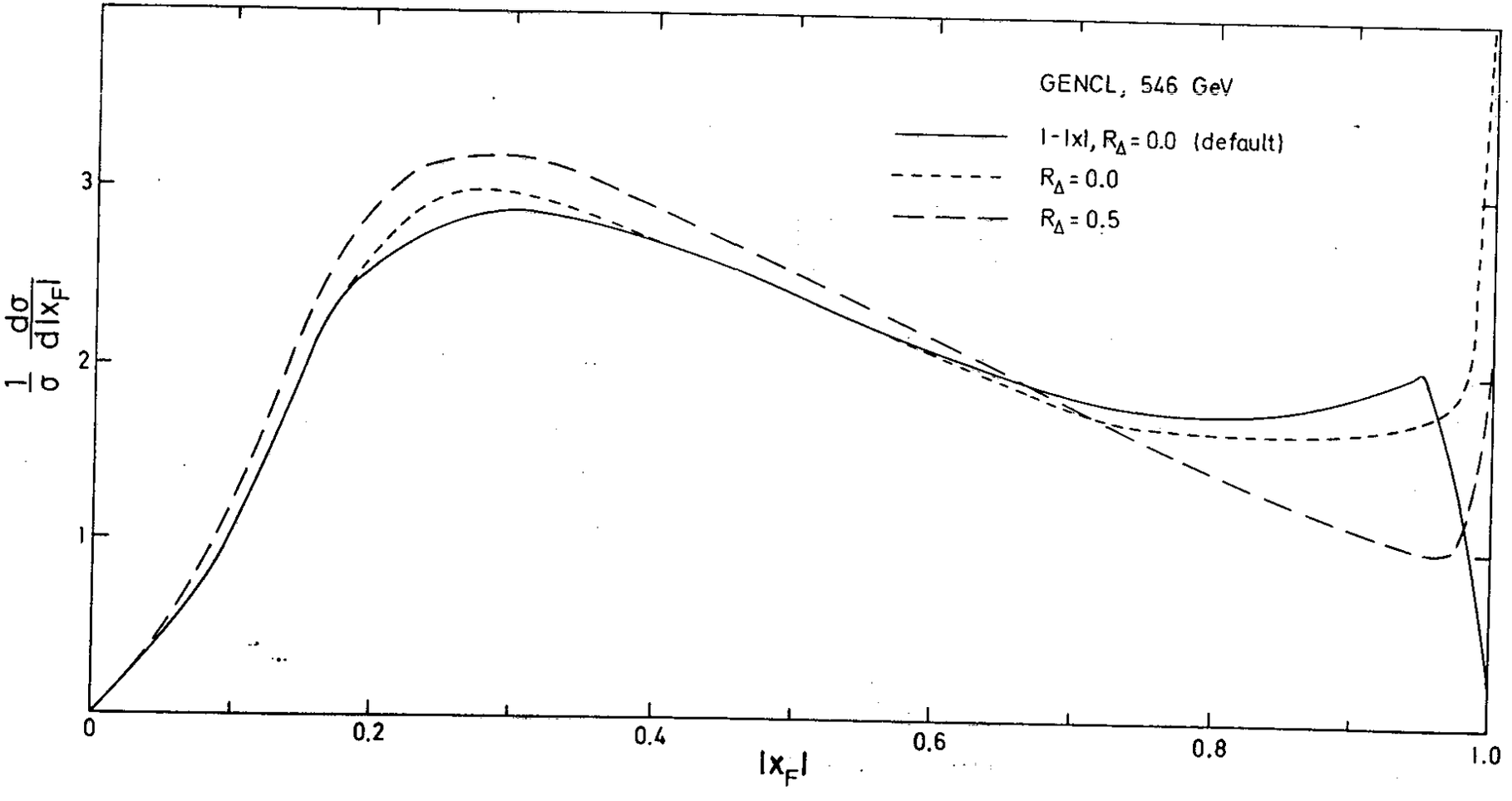
GENCL, 546 GeV
1-|x|, R_Δ = 0.0 (default)
R_Δ = 0.5
R_Δ = 0.0
$\frac{1}{\sigma}\frac{d\sigma}{d|x_F|}$
$|x_F|$
0
0.2
0.4
0.6
0.8
1.0
1
2
3

Fig. 3.5

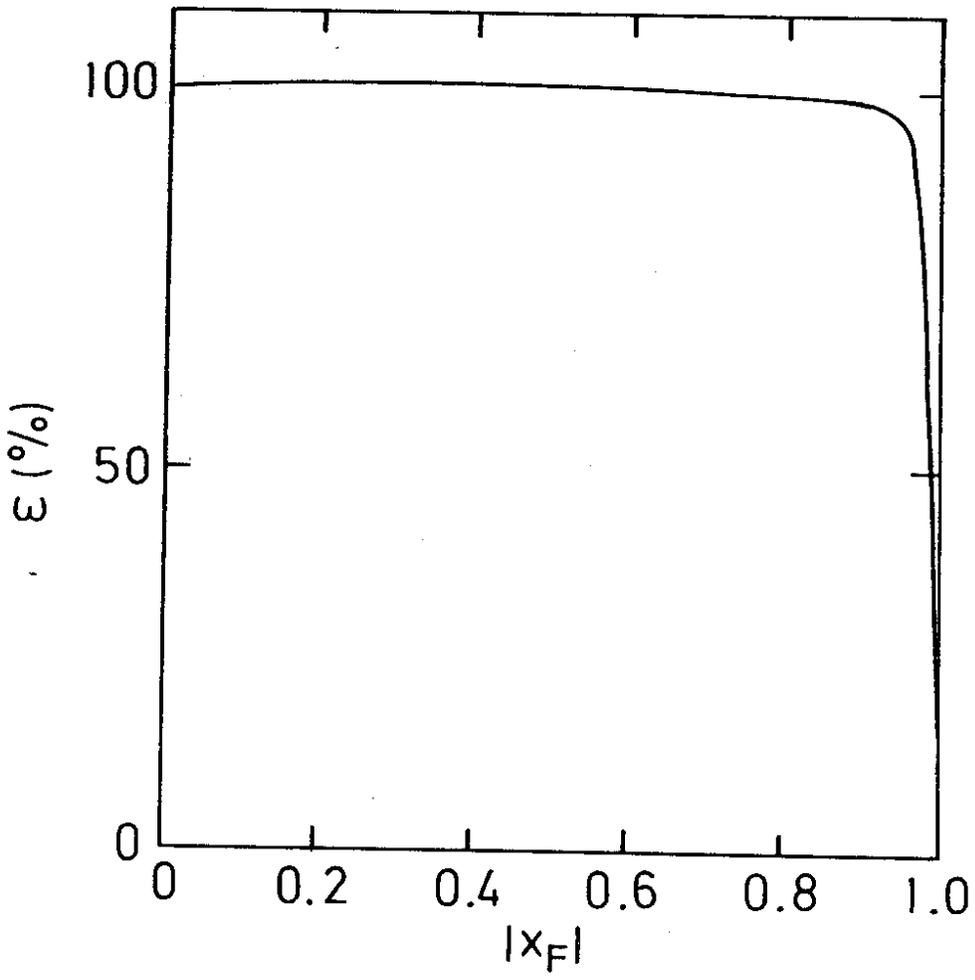

Fig. 3.6

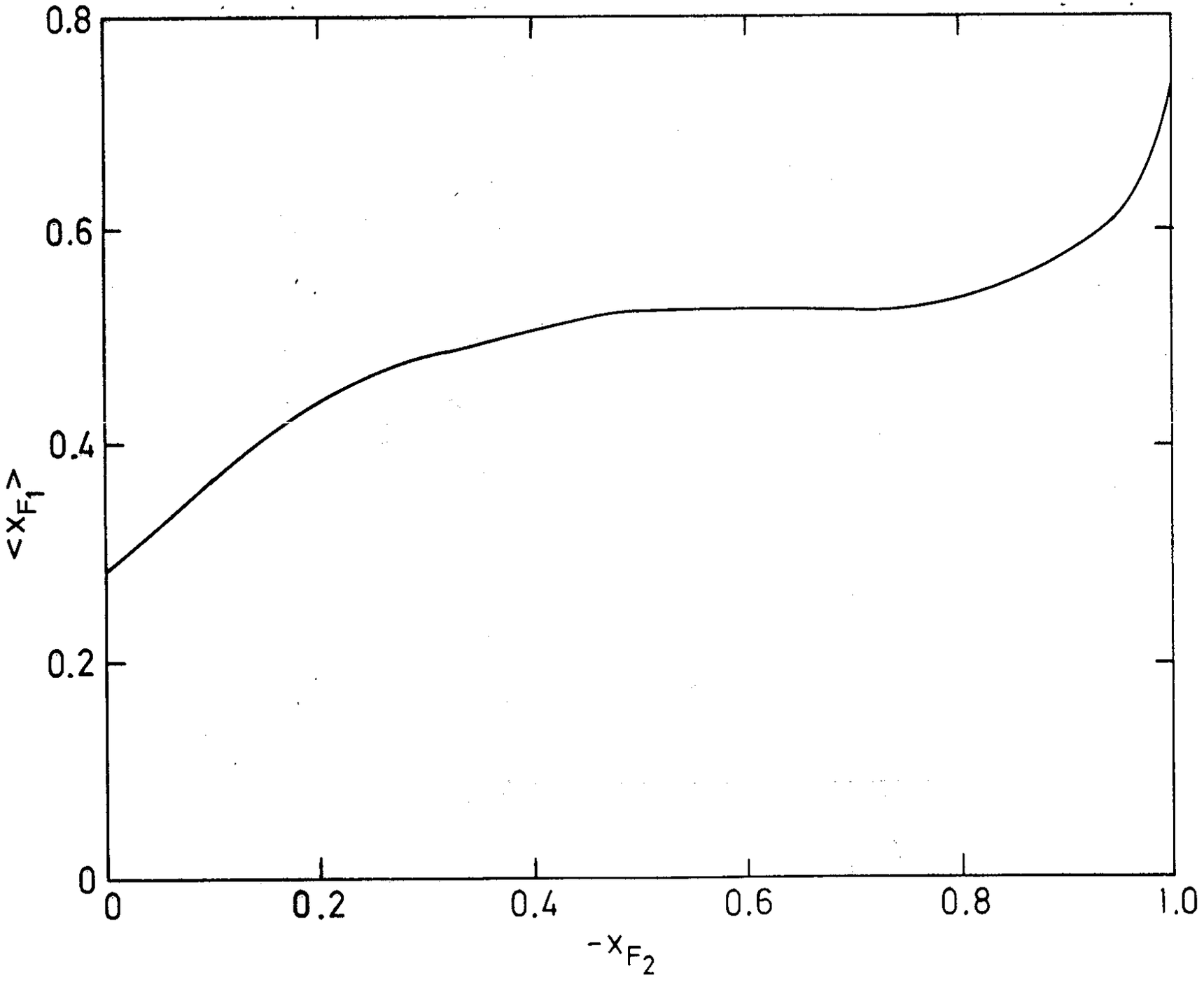

Fig. 3.7

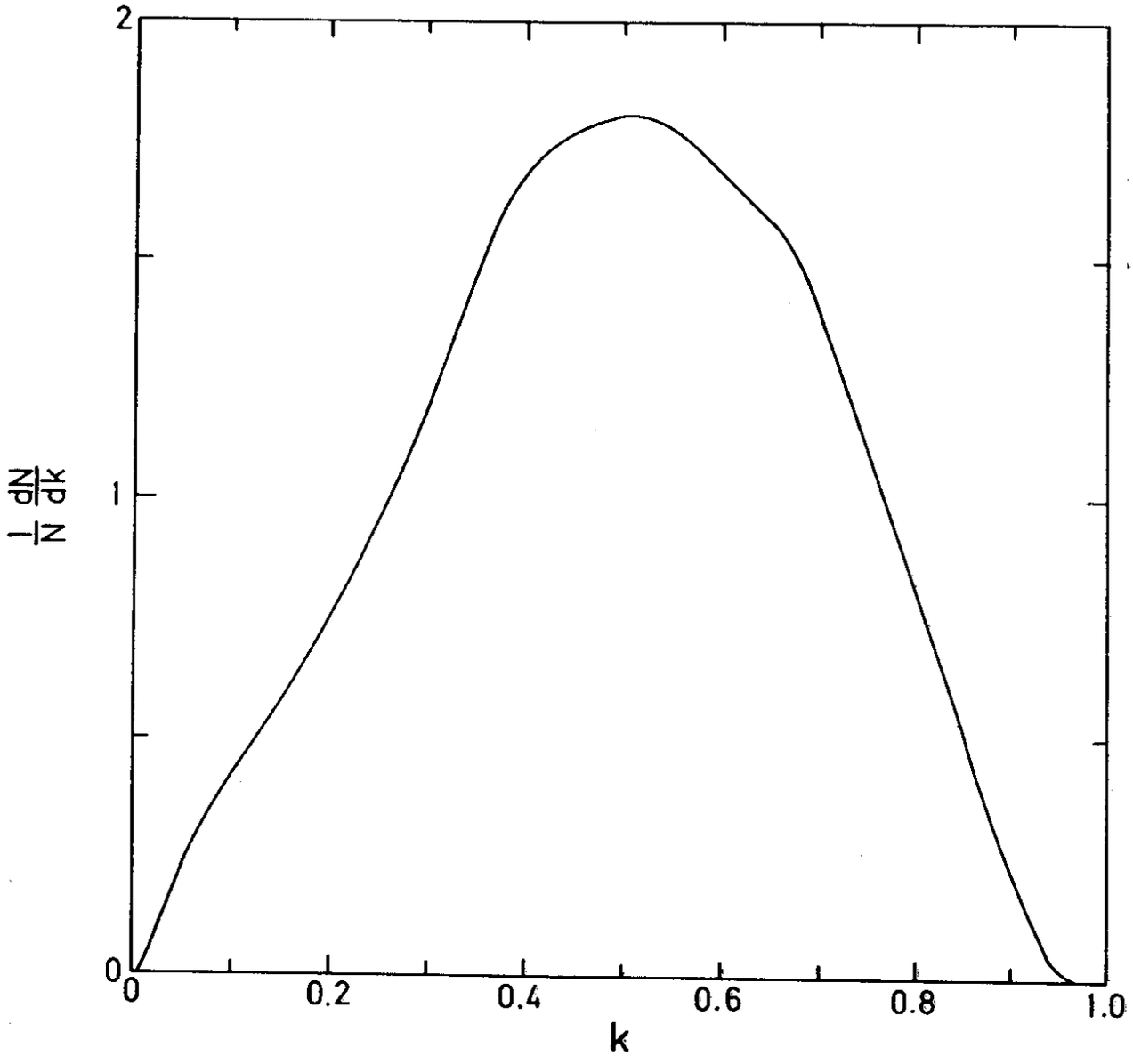

Fig. 3.8

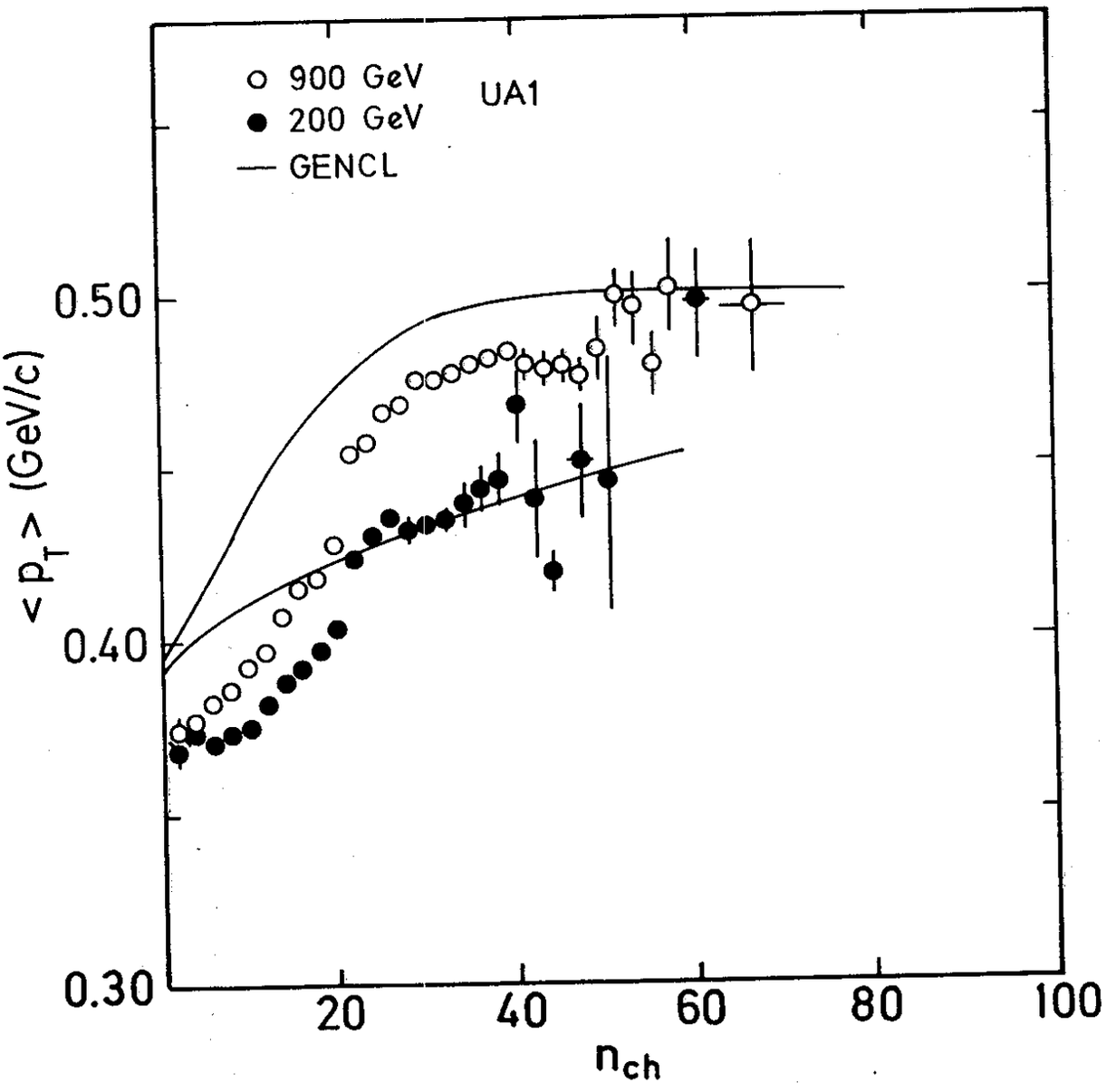

Fig. 3.9

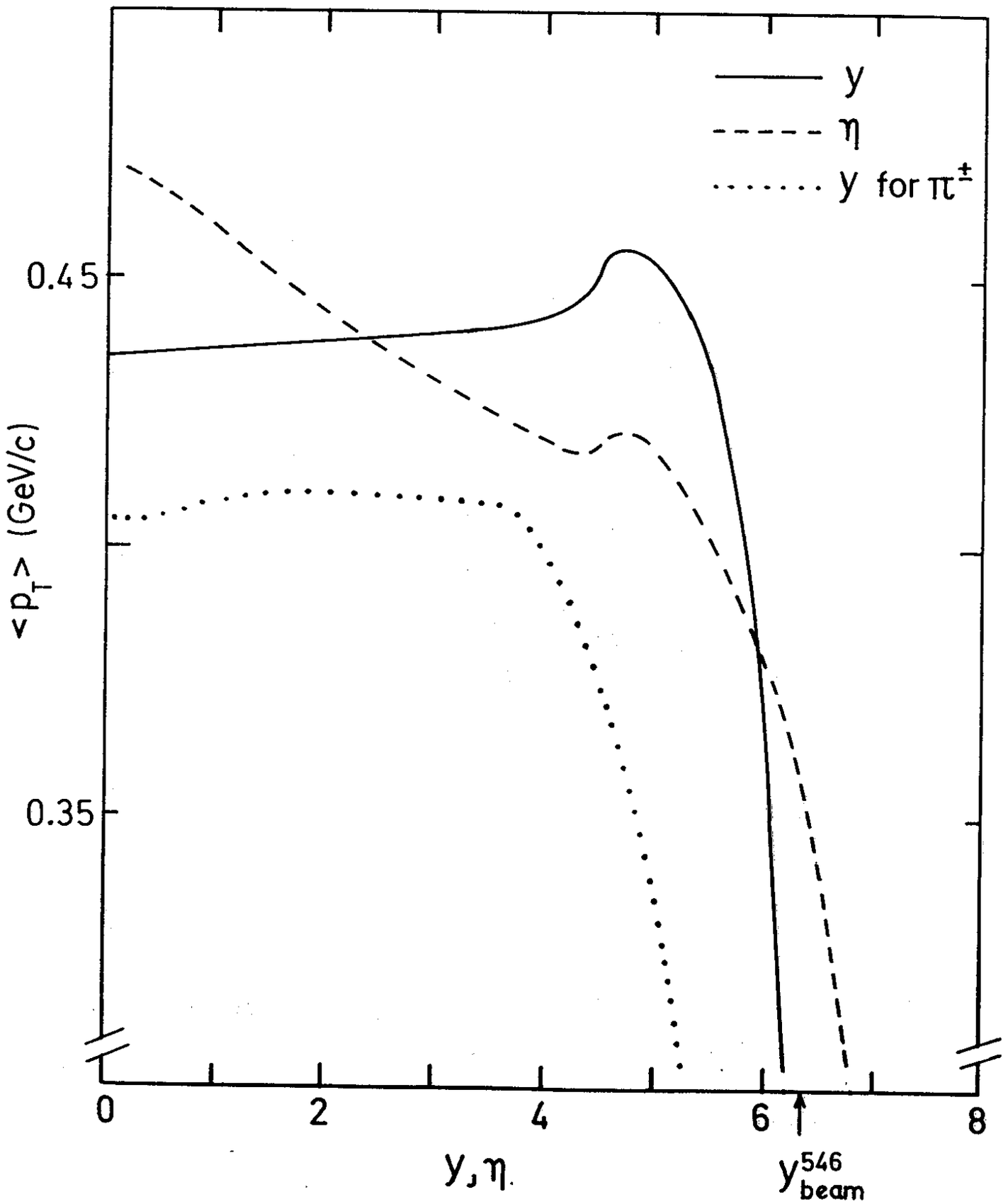

Fig. 3.10

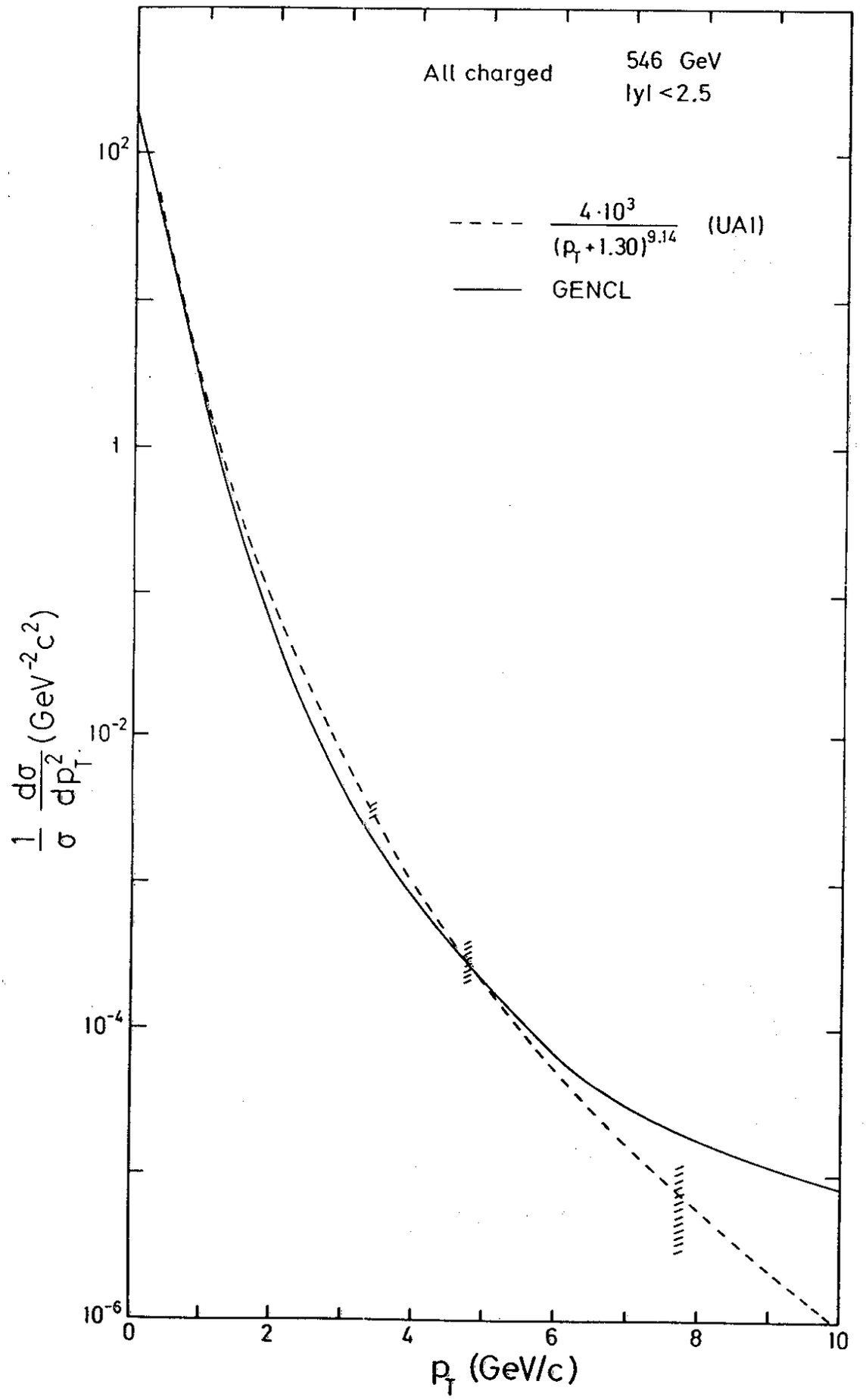
All charged
546 GeV
|y| < 2.5
$\frac{4 \cdot 10^3}{(p_T + 1.30)^{9.14}}$ (UA1)
GENCL
$\frac{1}{\sigma} \frac{d\sigma}{dp_T^2}$ (GeV^{-2}c^2)
p_T (GeV/c)
10^2
1
10^{-2}
10^{-4}
10^{-6}
0
2
4
6
8
10

Fig. 3.11

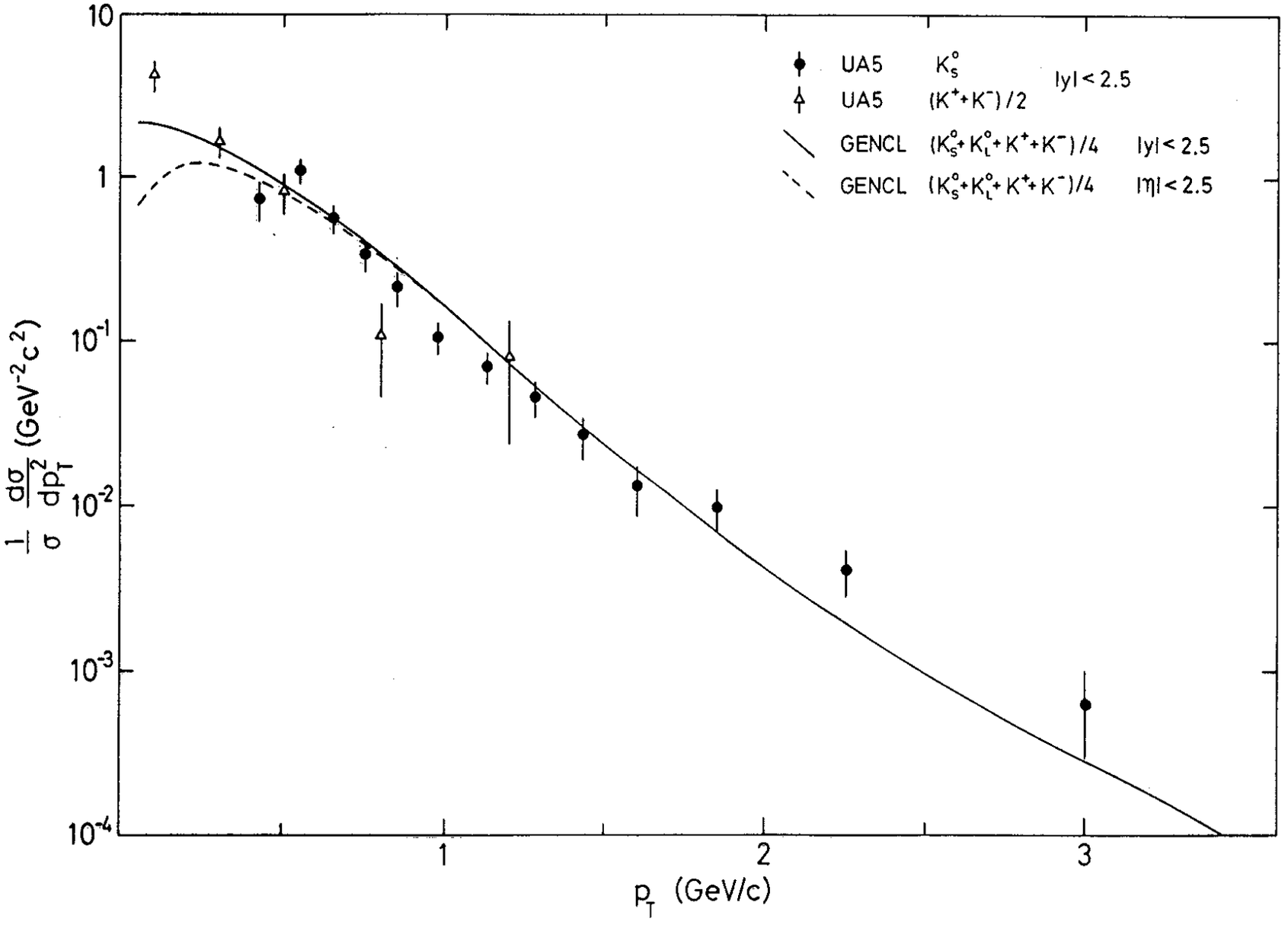
UA5 K^0_S
UA5 $(K^+ + K^-)/2$
$|y| < 2.5$
GENCL $(K^0_S + K^0_L + K^+ + K^-)/4$ $|y| < 2.5$
GENCL $(K^0_S + K^0_L + K^+ + K^-)/4$ $|\eta| < 2.5$
$\frac{1}{\sigma}\frac{d\sigma}{dp_T^2}$ $(GeV^{-2}c^2)$
p_T (GeV/c)
10
1
10^{-1}
10^{-2}
10^{-3}
10^{-4}
1
2
3

Fig. 3.12

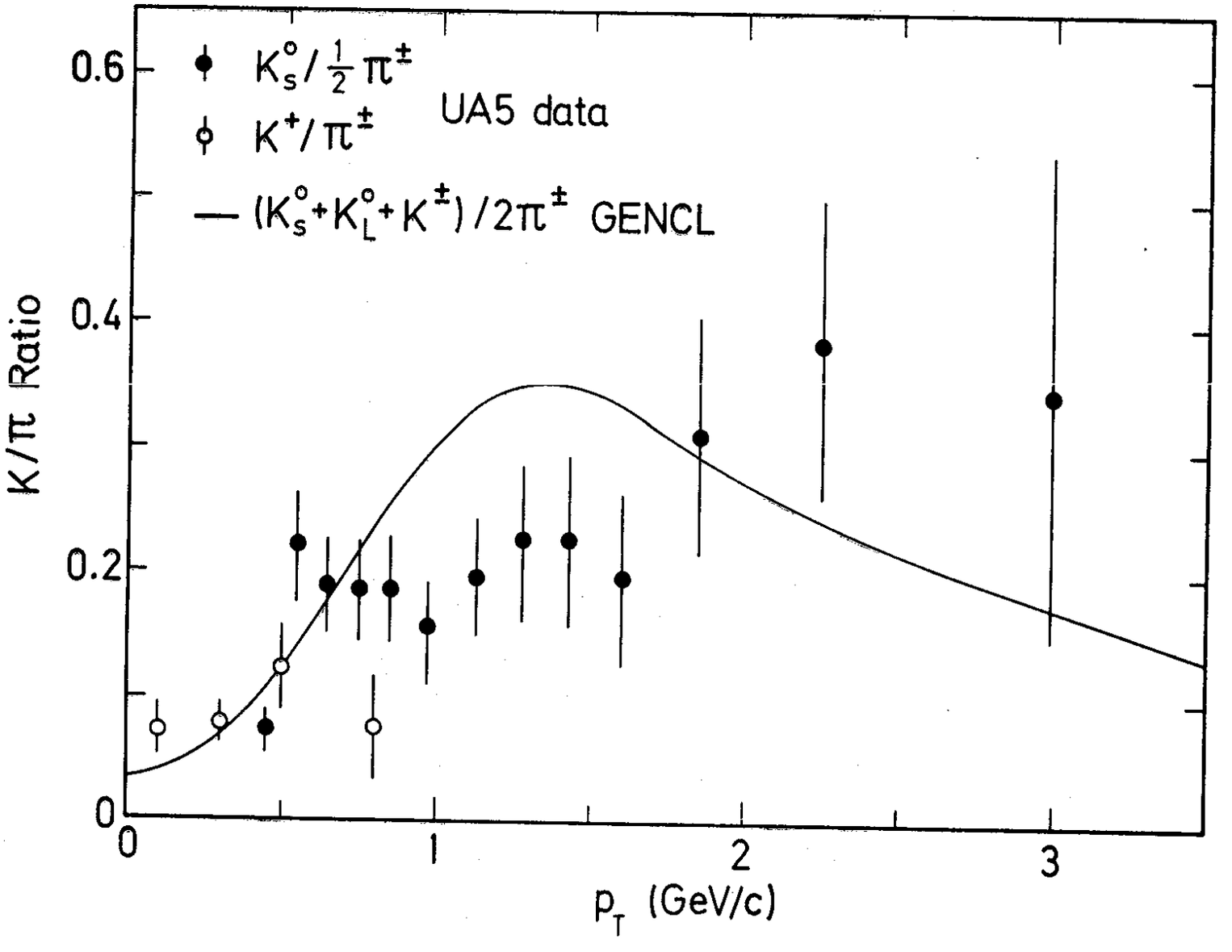
$K_s^0/\frac{1}{2}\pi^\pm$
$K^+/\pi^\pm$
UA5 data
$(K_s^0+K_L^0+K^\pm)/2\pi^\pm$ GENCL
K/π Ratio
0.6
0.4
0.2
0
0
1
2
3
p_T (GeV/c)

Fig. 3.13

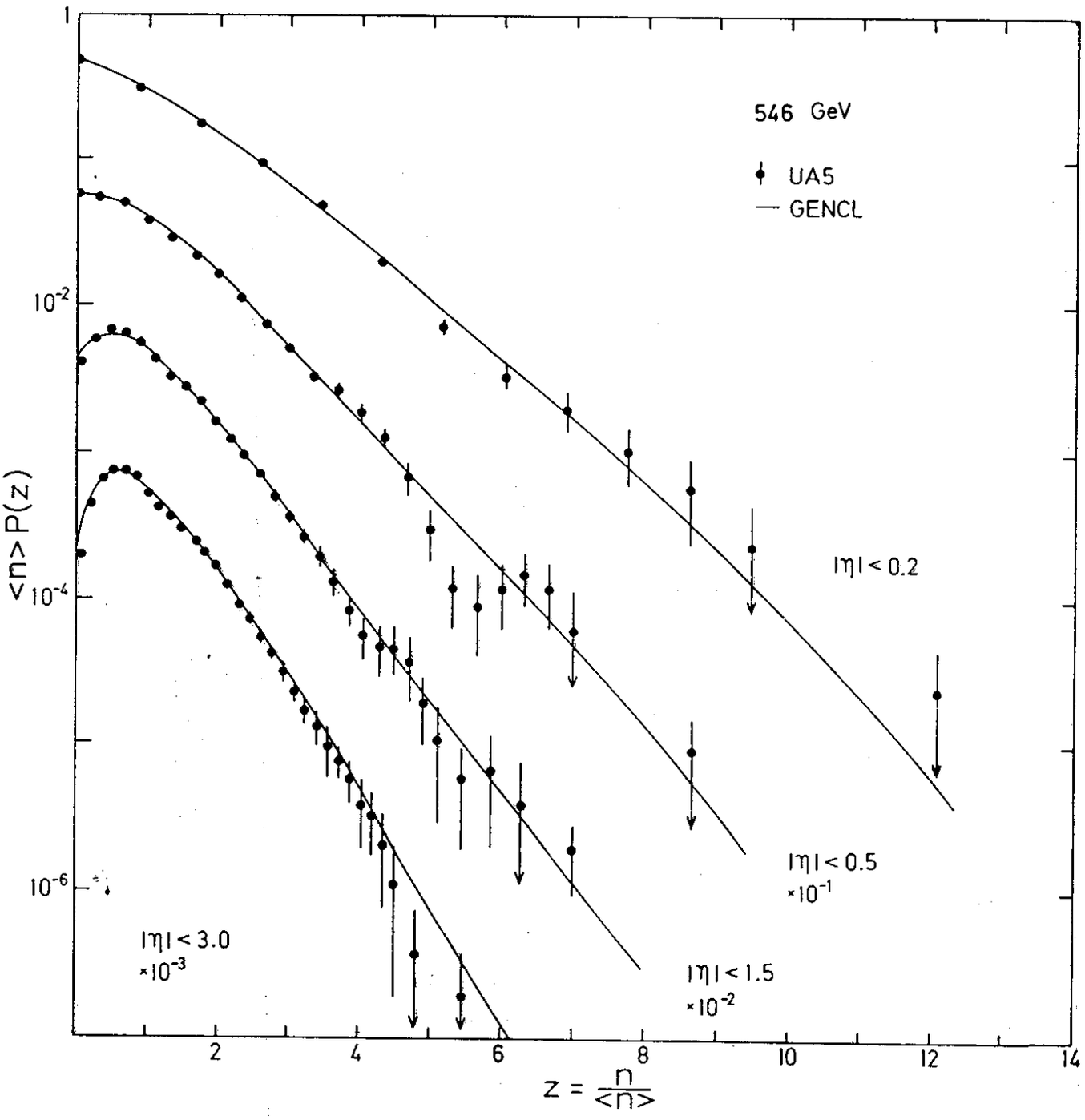
546 GeV
UA5
GENCL
$|\eta| < 0.2$
$|\eta| < 0.5$
$\times 10^{-1}$
$|\eta| < 1.5$
$\times 10^{-2}$
$|\eta| < 3.0$
$\times 10^{-3}$
$\langle n \rangle P(z)$
$z = \frac{n}{\langle n \rangle}$
1
10^{-2}
10^{-4}
10^{-6}
2
4
6
8
10
12
14

Fig. 3.14

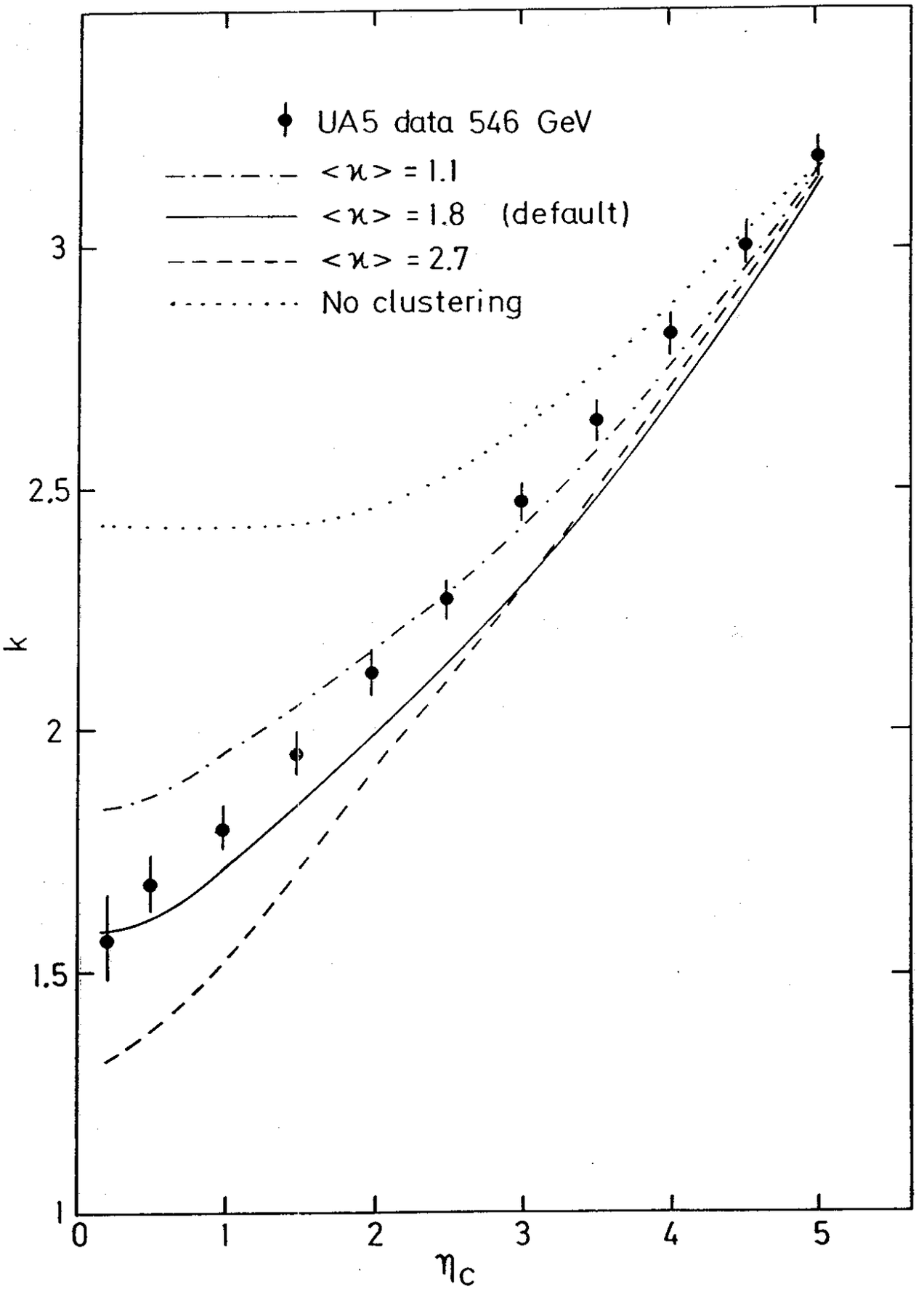
UA5 data 546 GeV
<n> = 1.1
<n> = 1.8 (default)
<n> = 2.7
No clustering
K
η_c
1
1.5
2
2.5
3
0
1
2
3
4
5

Fig. 3.15

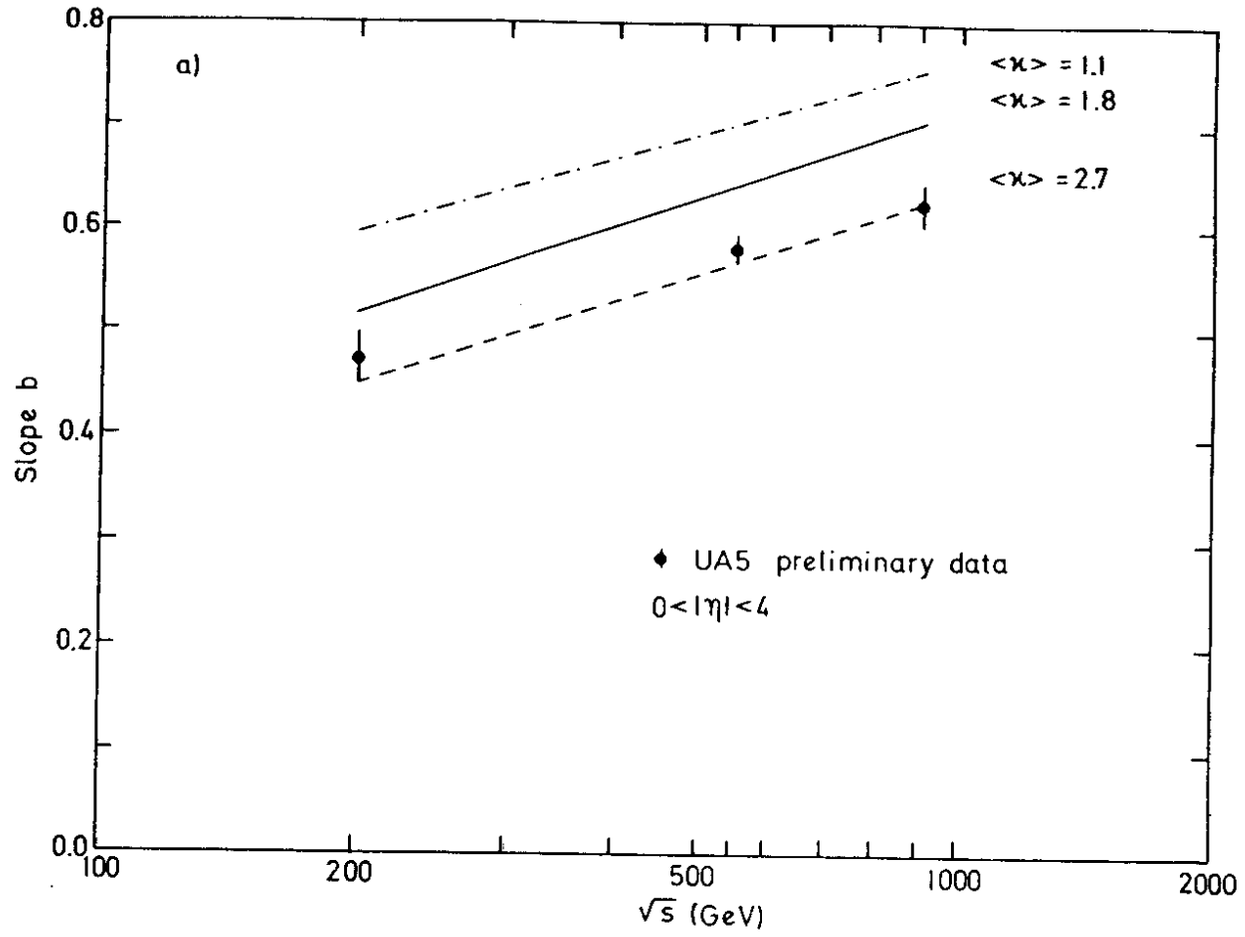
a)
<x> = 1.1
<x> = 1.8
<x> = 2.7
♦ UA5 preliminary data
0<|η|<4
Slope b
√s (GeV)
0.0
0.2
0.4
0.6
0.8
100
200
500
1000
2000

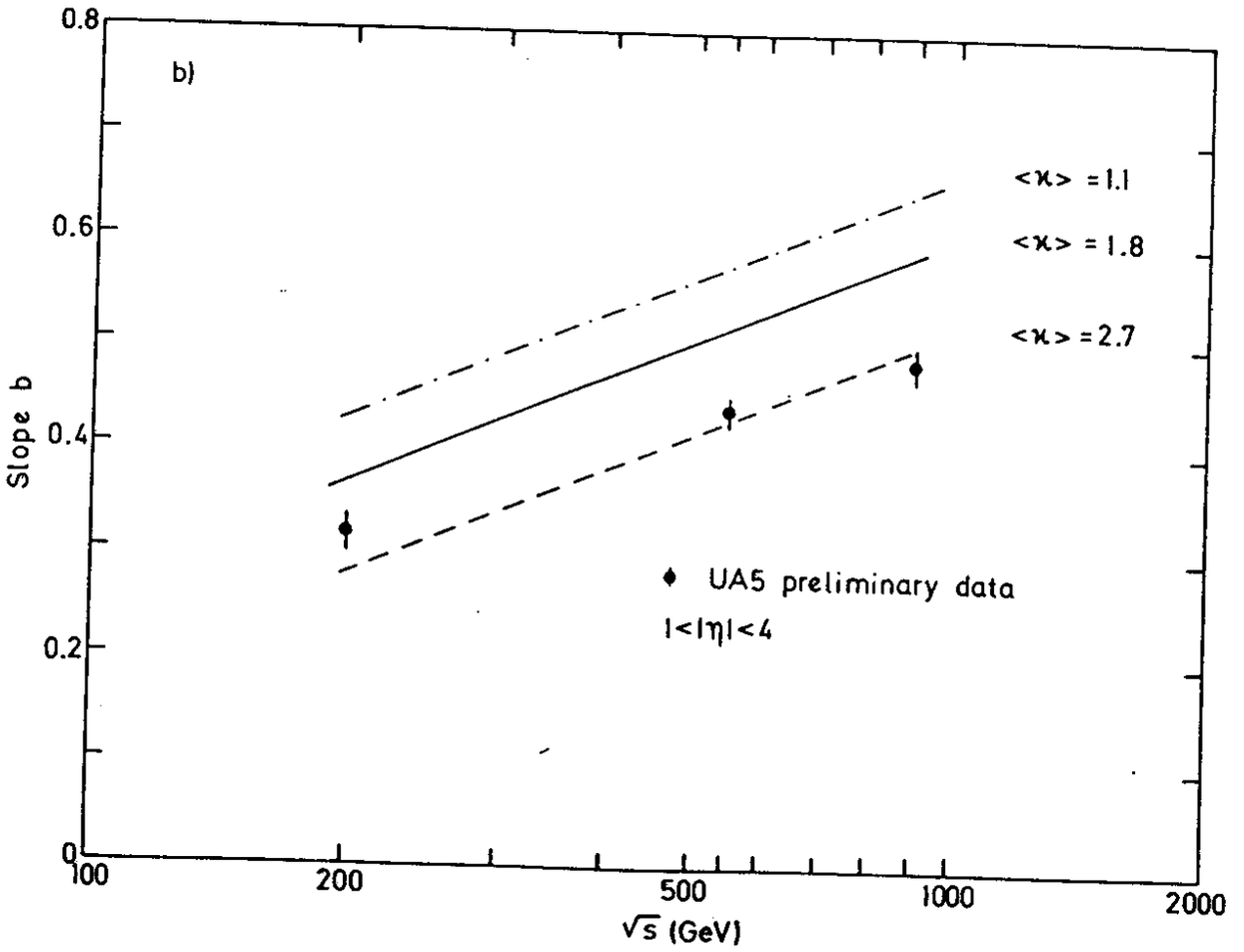
b)
<x> = 1.1
<x> = 1.8
<x> = 2.7
♦ UA5 preliminary data
1<|η|<4
Slope b
√s (GeV)
0
0.2
0.4
0.6
0.8
100
200
500
1000
2000

Fig. 3.16

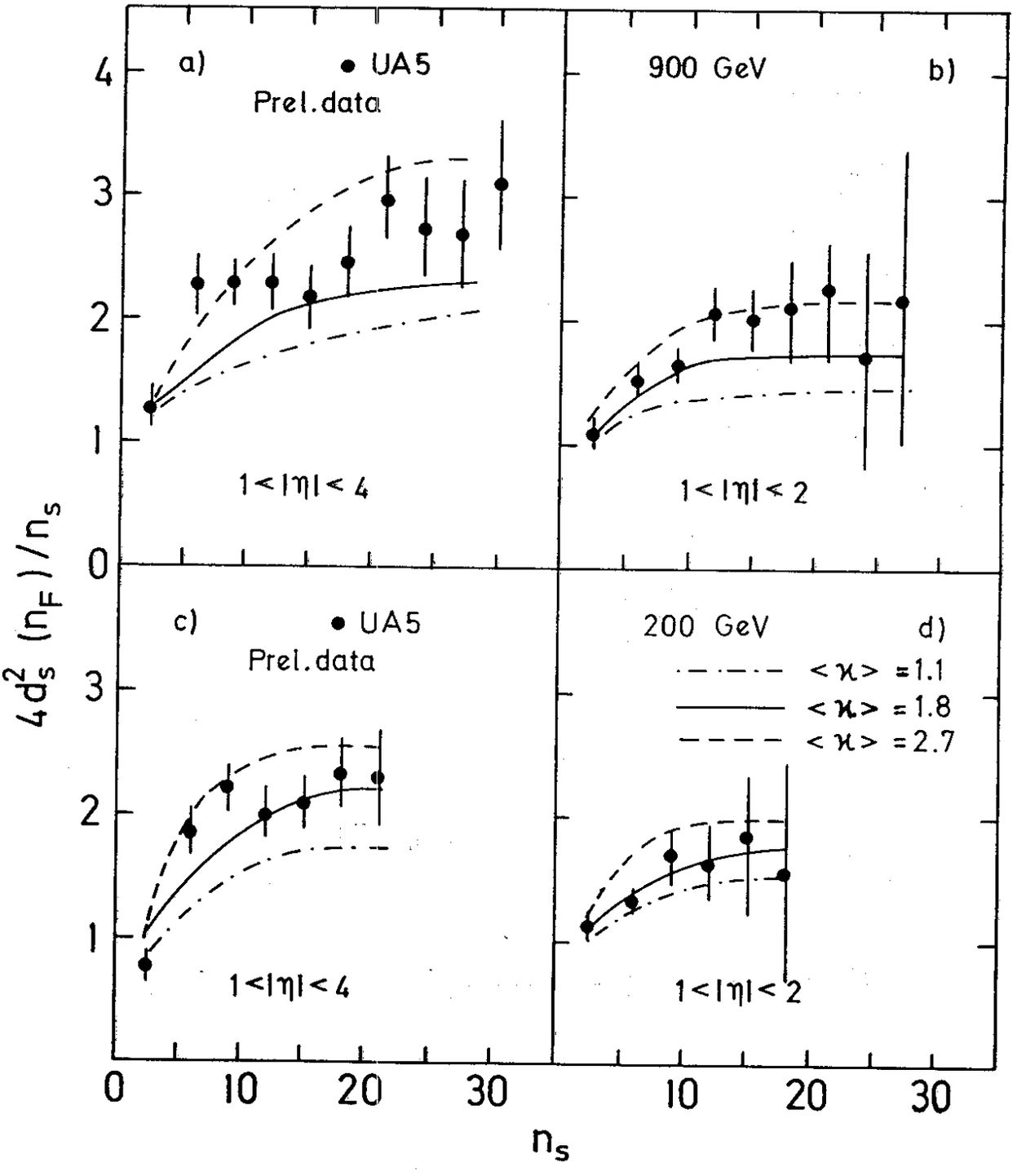
a)
• UA5
Prel.data
1<|η|<4
900 GeV
b)
1<|η|<2
c)
• UA5
Prel.data
1<|η|<4
200 GeV
d)
<κ> =1.1
<κ> =1.8
<κ> =2.7
1<|η|<2
$4d_s^2(n_F)/n_s$
n_s

Fig. 3.17

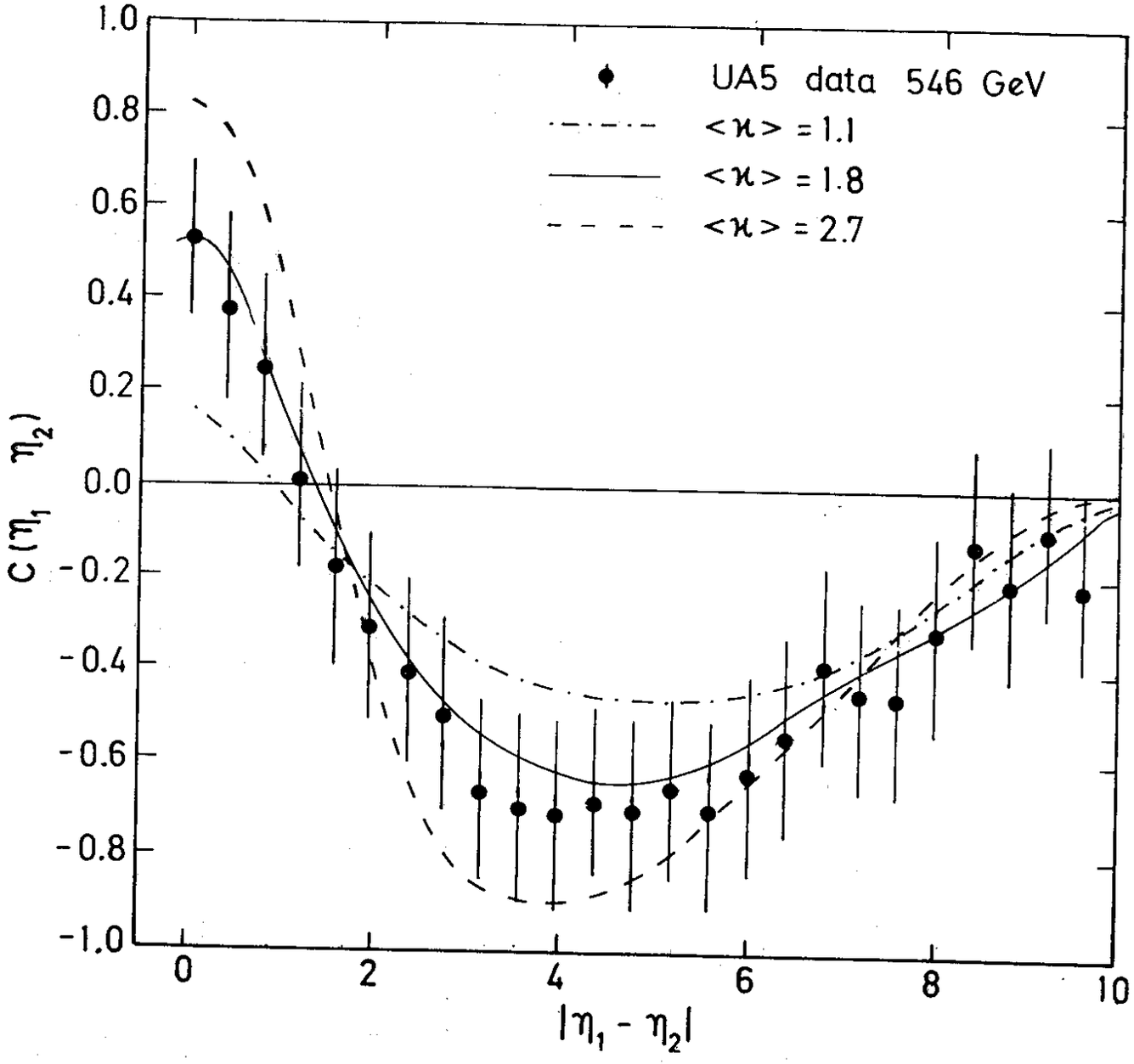
UA5 data 546 GeV
<n> = 1.1
<n> = 1.8
<n> = 2.7
C(η1 η2)
|η1 - η2|
1.0
0.8
0.6
0.4
0.2
0.0
-0.2
-0.4
-0.6
-0.8
-1.0
0
2
4
6
8
10

Fig. 3.18

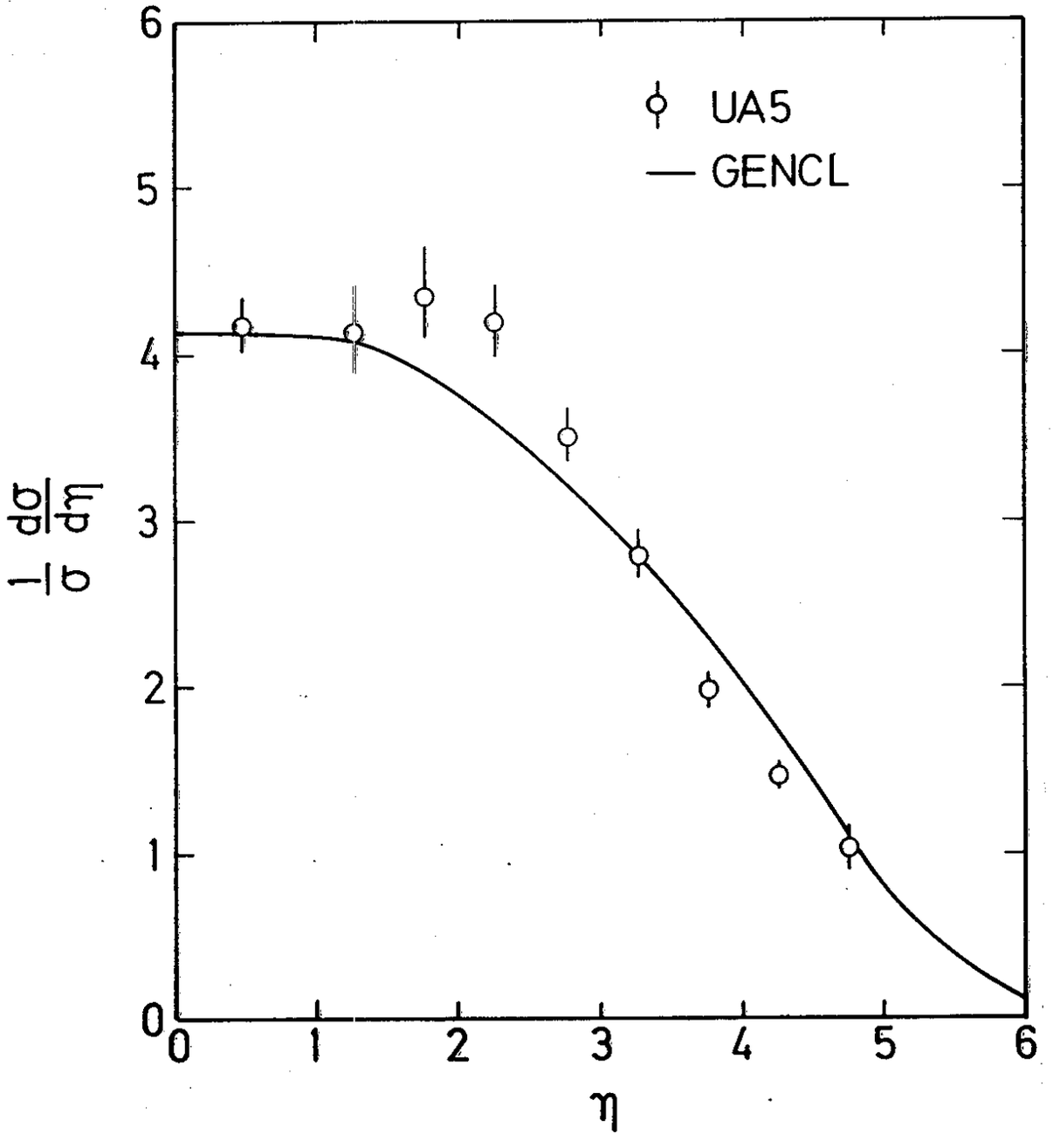

Fig. 3.19

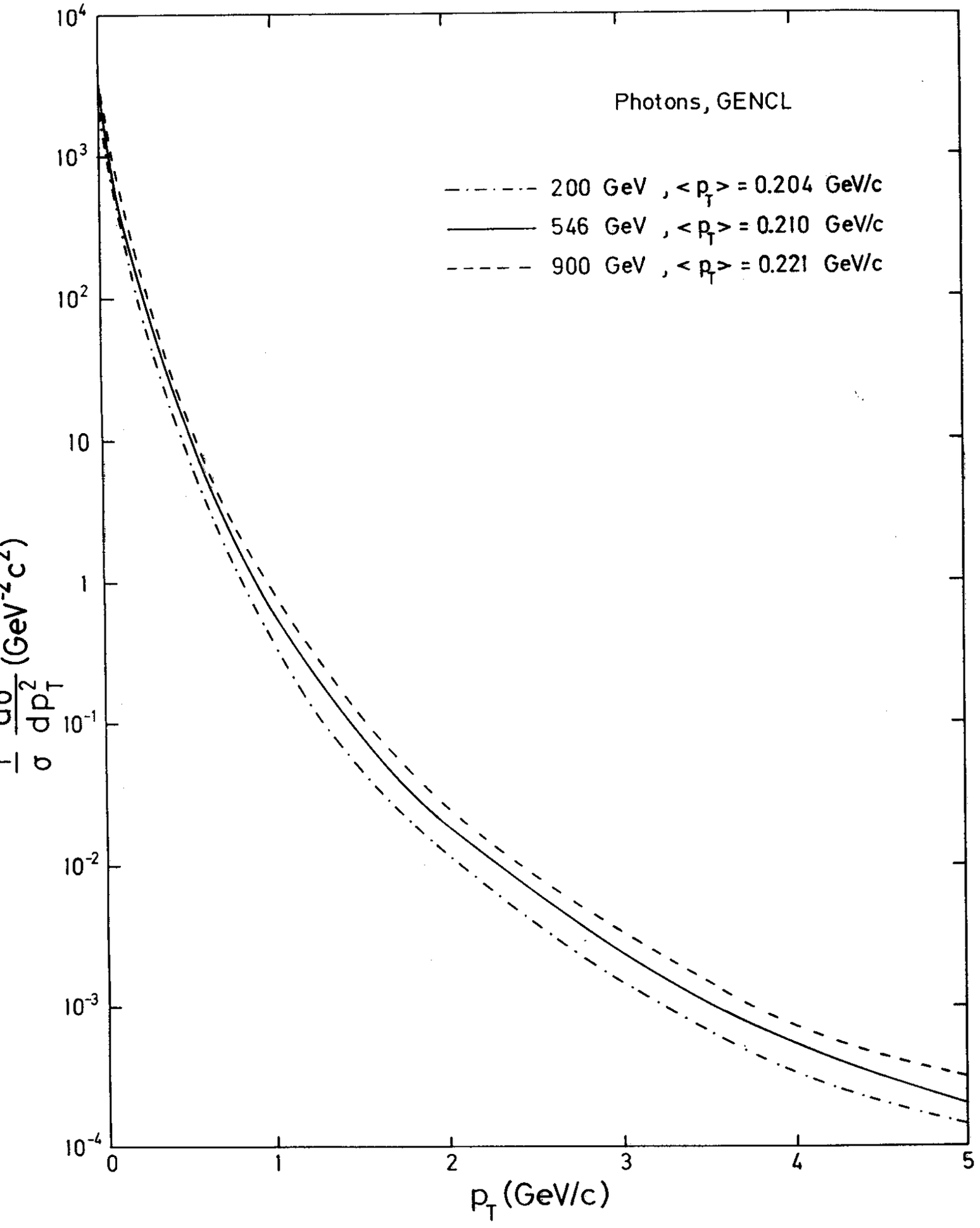
Photons, GENCL
200 GeV , < p_T > = 0.204 GeV/c
546 GeV , < p_T > = 0.210 GeV/c
900 GeV , < p_T > = 0.221 GeV/c
1/σ dσ/dp_T^2 (GeV^-2 c^2)
p_T (GeV/c)
10^4
10^3
10^2
10
1
10^-1
10^-2
10^-3
10^-4
0
1
2
3
4
5

Fig. 3.20

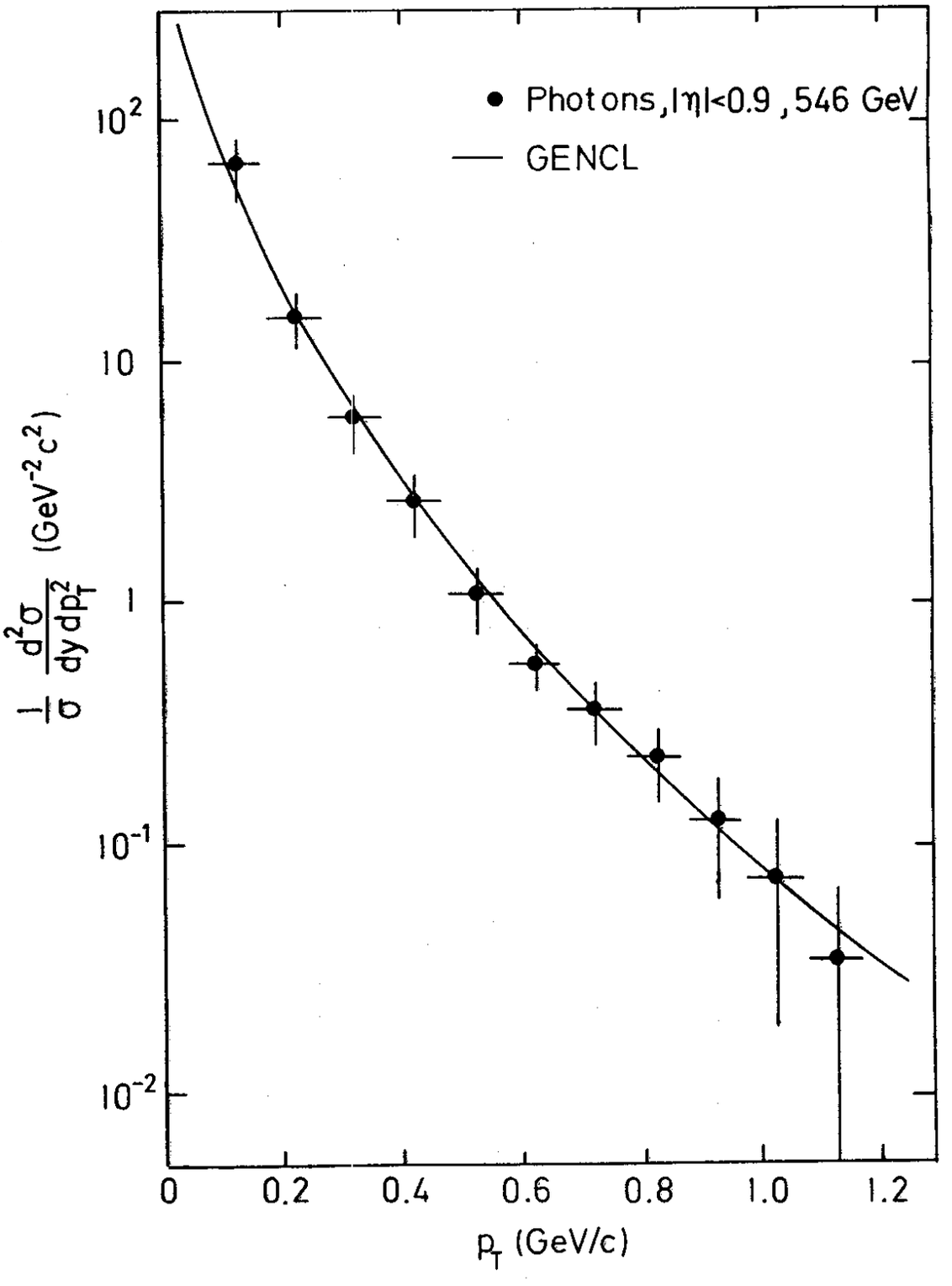
Photons, |η|<0.9 , 546 GeV
GENCL
$\frac{1}{\sigma}\frac{d^2\sigma}{dy\,dp_T^2}$ (GeV^{-2}c^2)
10^2
10
1
10^{-1}
10^{-2}
0
0.2
0.4
0.6
0.8
1.0
1.2
p_T (GeV/c)

Fig. 3.21

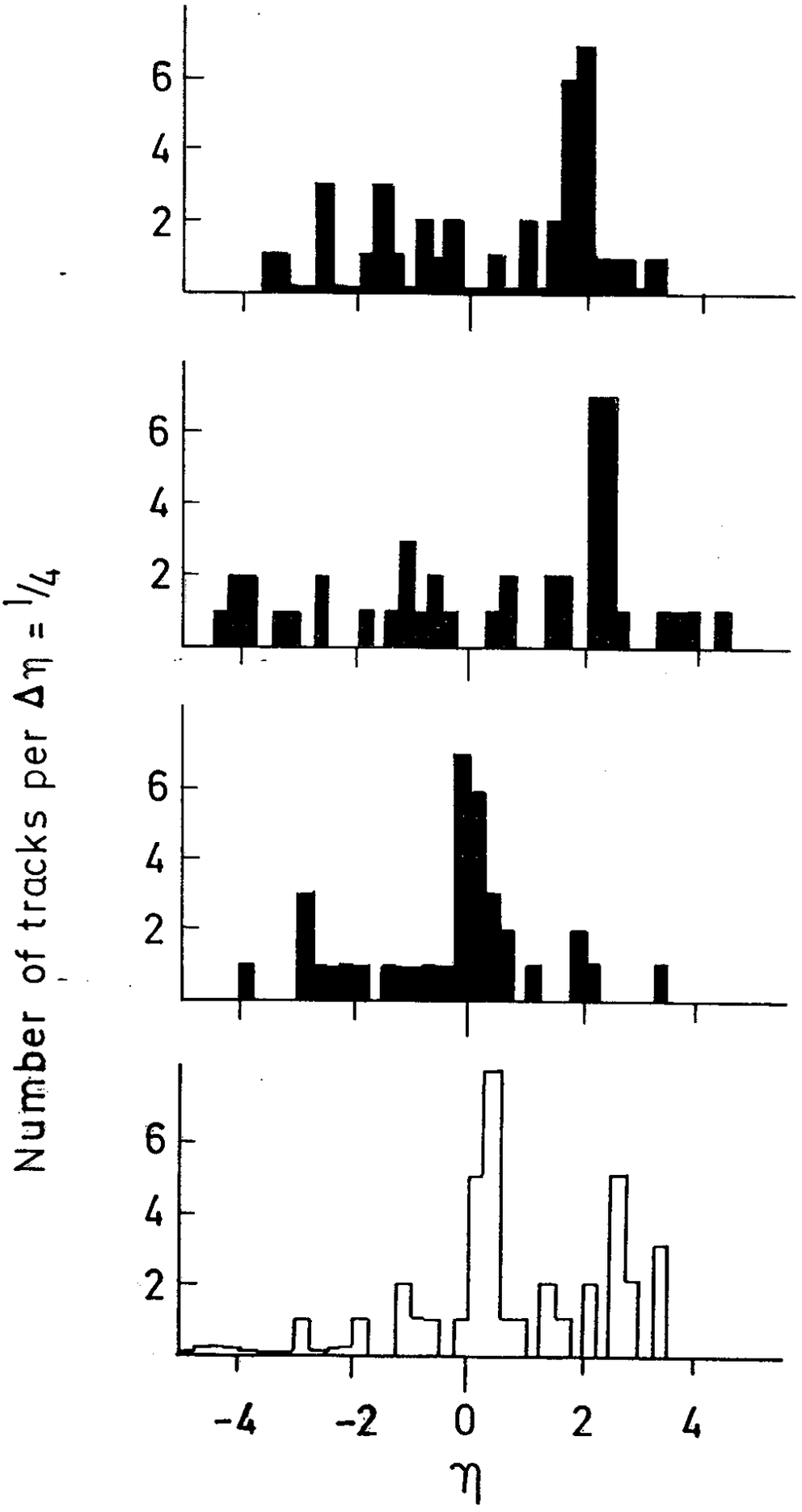

Fig. 3.22

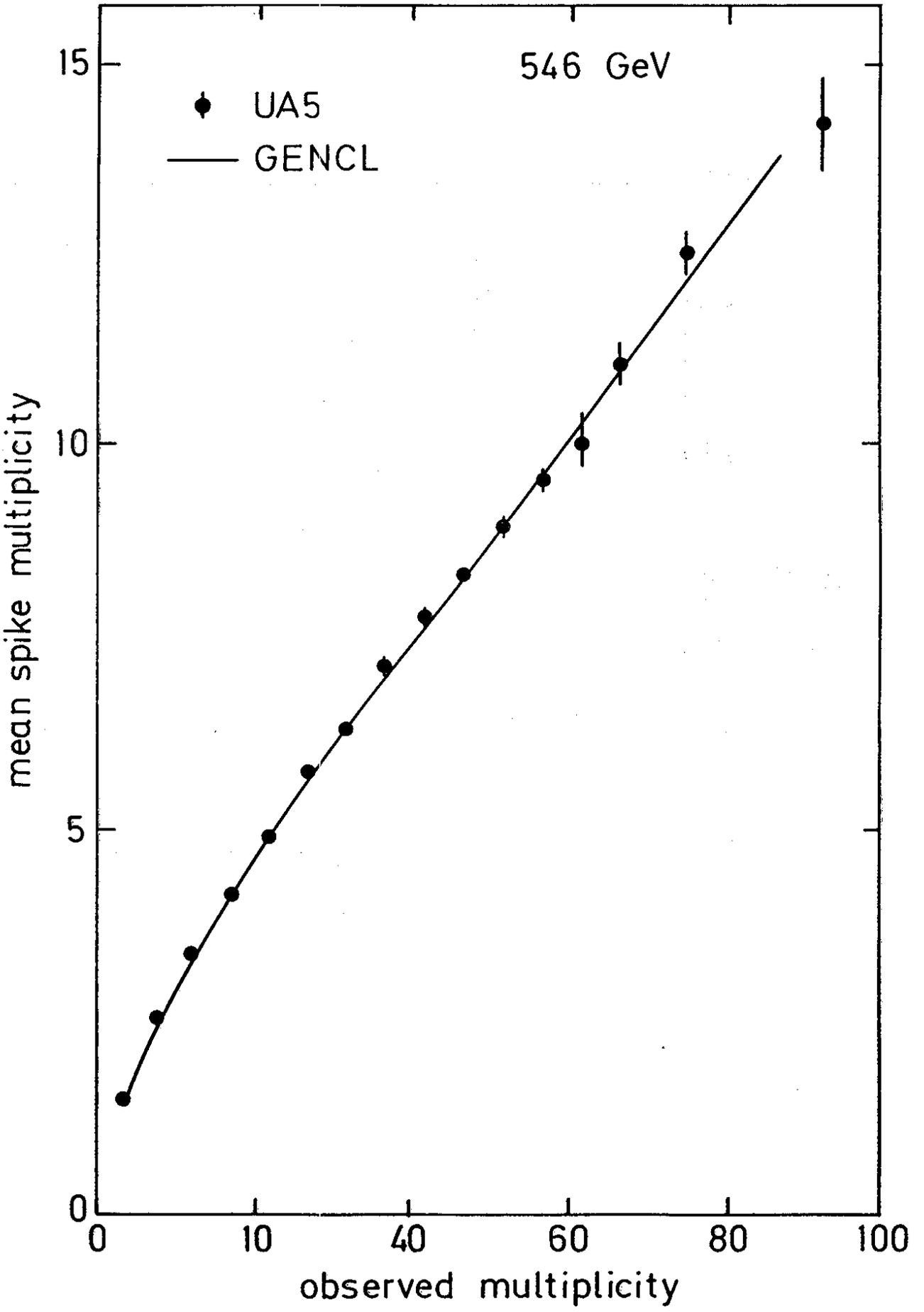
546 GeV
UA5
GENCL
mean spike multiplicity
observed multiplicity
0
5
10
15
0
10
40
60
80
100

Fig. 3.23

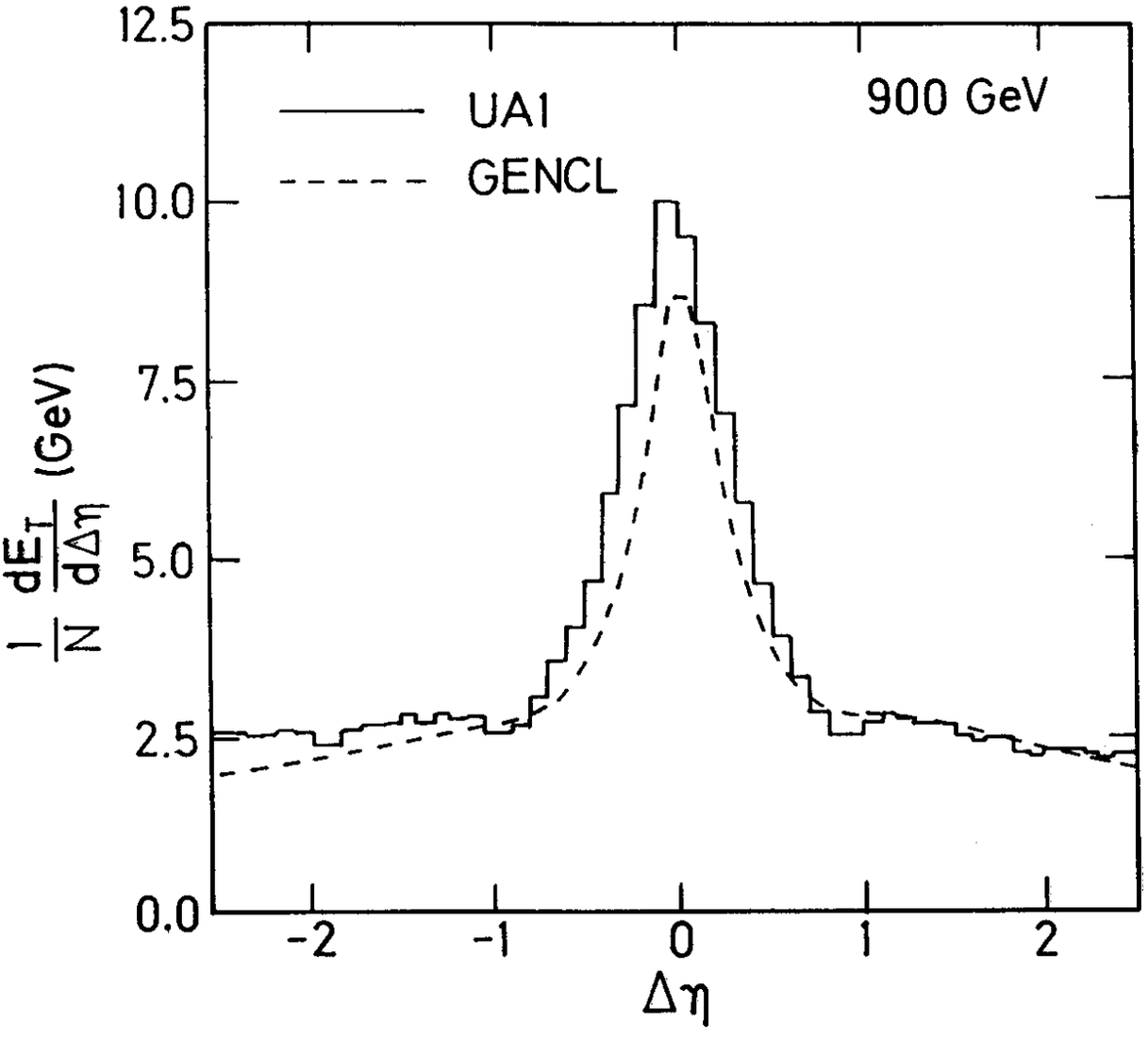
12.5
10.0
7.5
5.0
2.5
0.0
UA1
GENCL
900 GeV
$\frac{1}{N}\frac{dE_T}{d\Delta\eta}$ (GeV)
-2
-1
0
1
2
$\Delta\eta$

Fig. 3.24

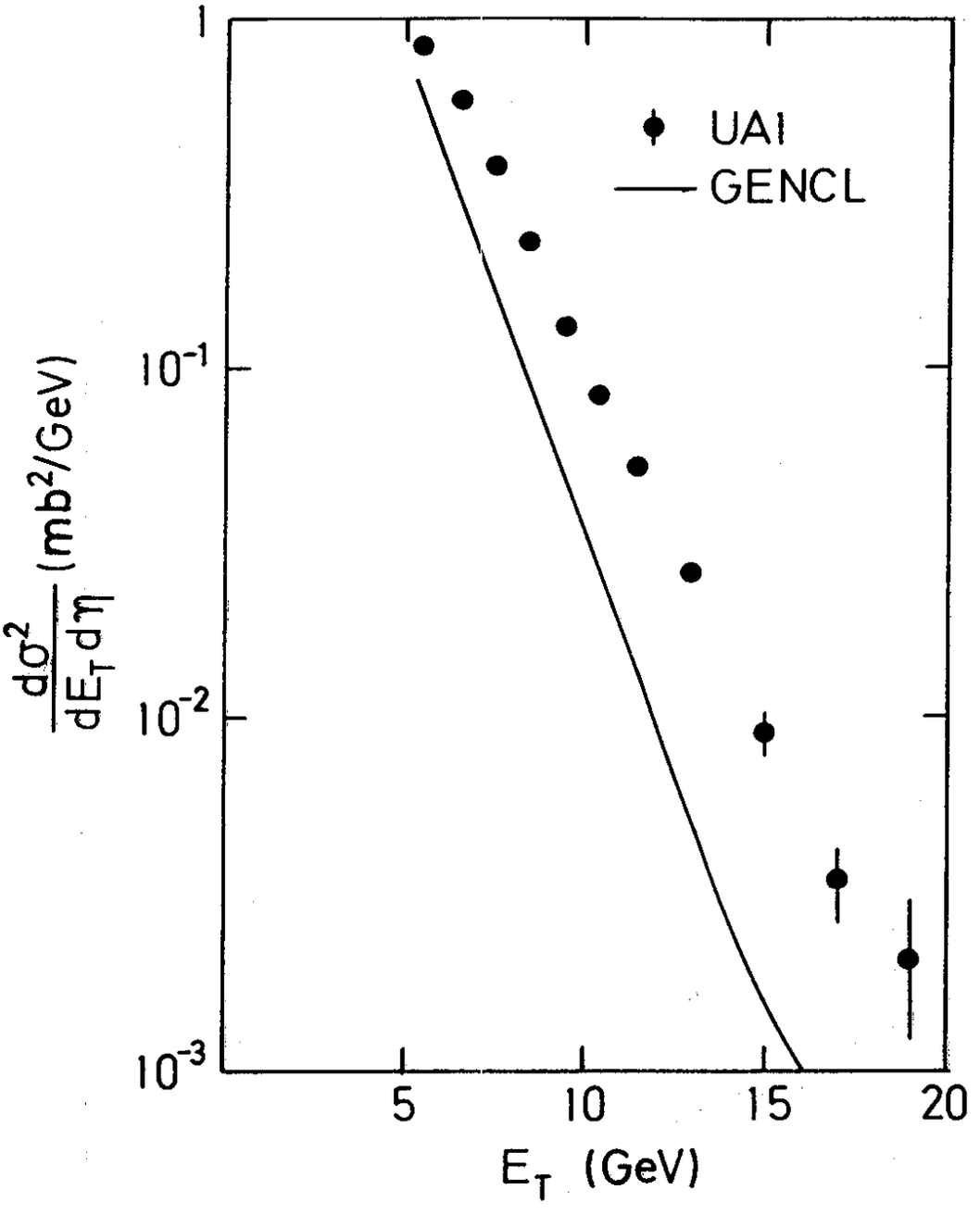
UA1
GENCL
1
10^{-1}
10^{-2}
10^{-3}
$\frac{d\sigma^2}{dE_T d\eta}$ (mb²/GeV)
5
10
15
20
E_T (GeV)

Fig. 3.25

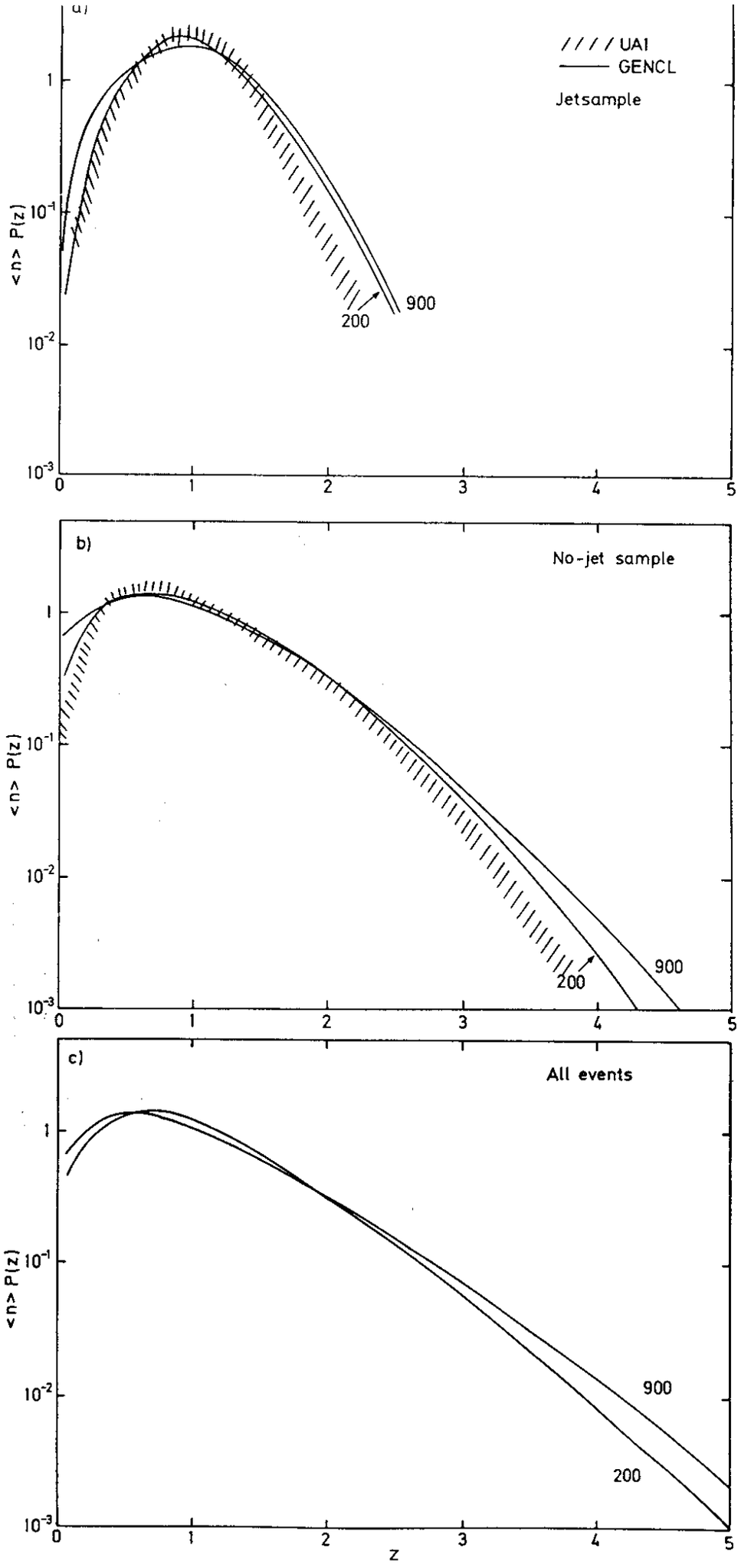
a)
//// UA1
—— GENCL
Jetsample
<n> P(z)
1
10^{-1}
10^{-2}
10^{-3}
900
200
0
1
2
3
4
5
b)
No-jet sample
<n> P(z)
1
10^{-1}
10^{-2}
10^{-3}
900
200
0
1
2
3
4
5
c)
All events
<n> P(z)
1
10^{-1}
10^{-2}
10^{-3}
900
200
0
1
2
3
4
5
z

Fig. 3.26

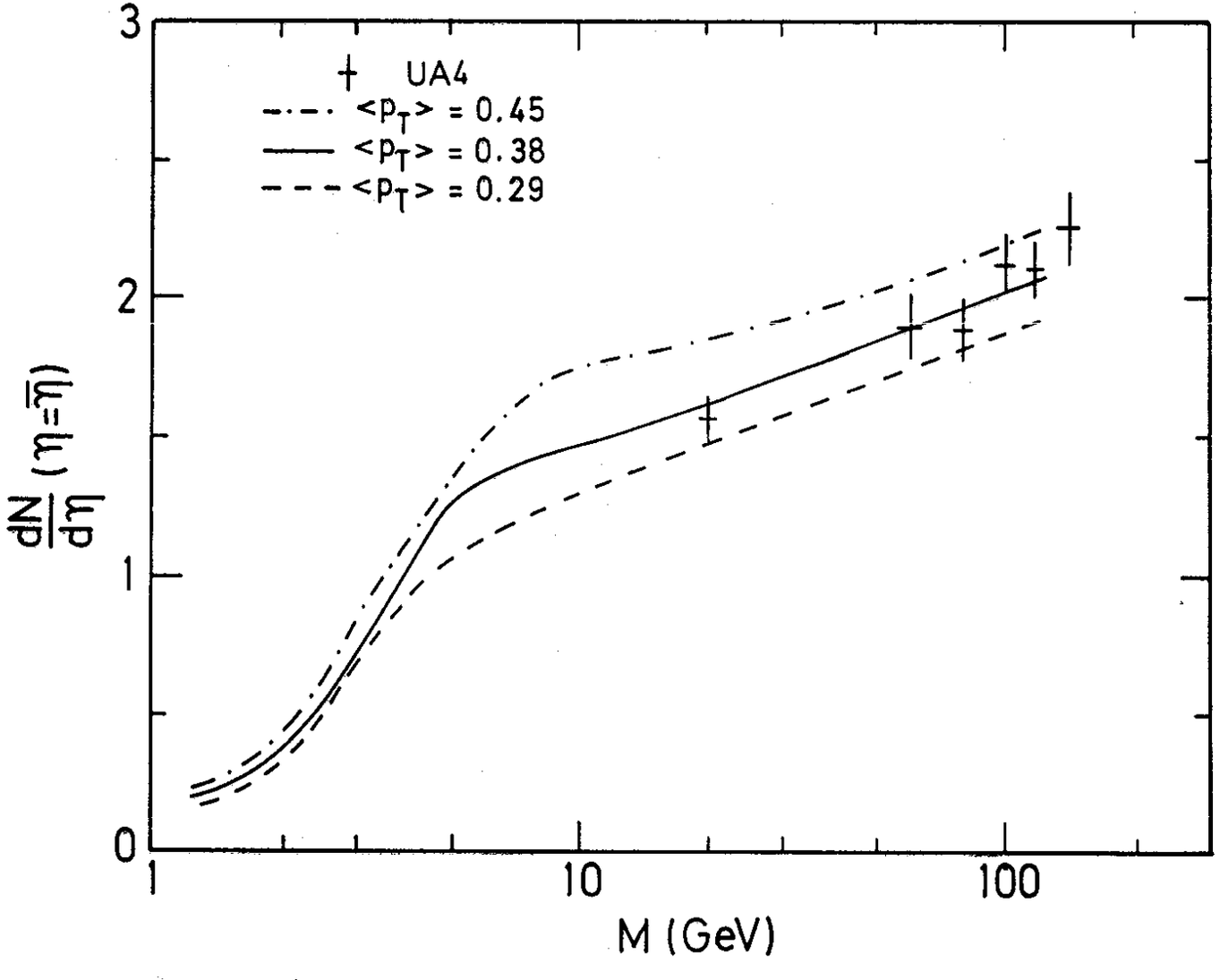
UA4
<p_T> = 0.45
<p_T> = 0.38
<p_T> = 0.29
$\frac{dN}{d\eta}(\eta=\bar{\eta})$
0
1
2
3
1
10
100
M (GeV)

Fig. 3.27

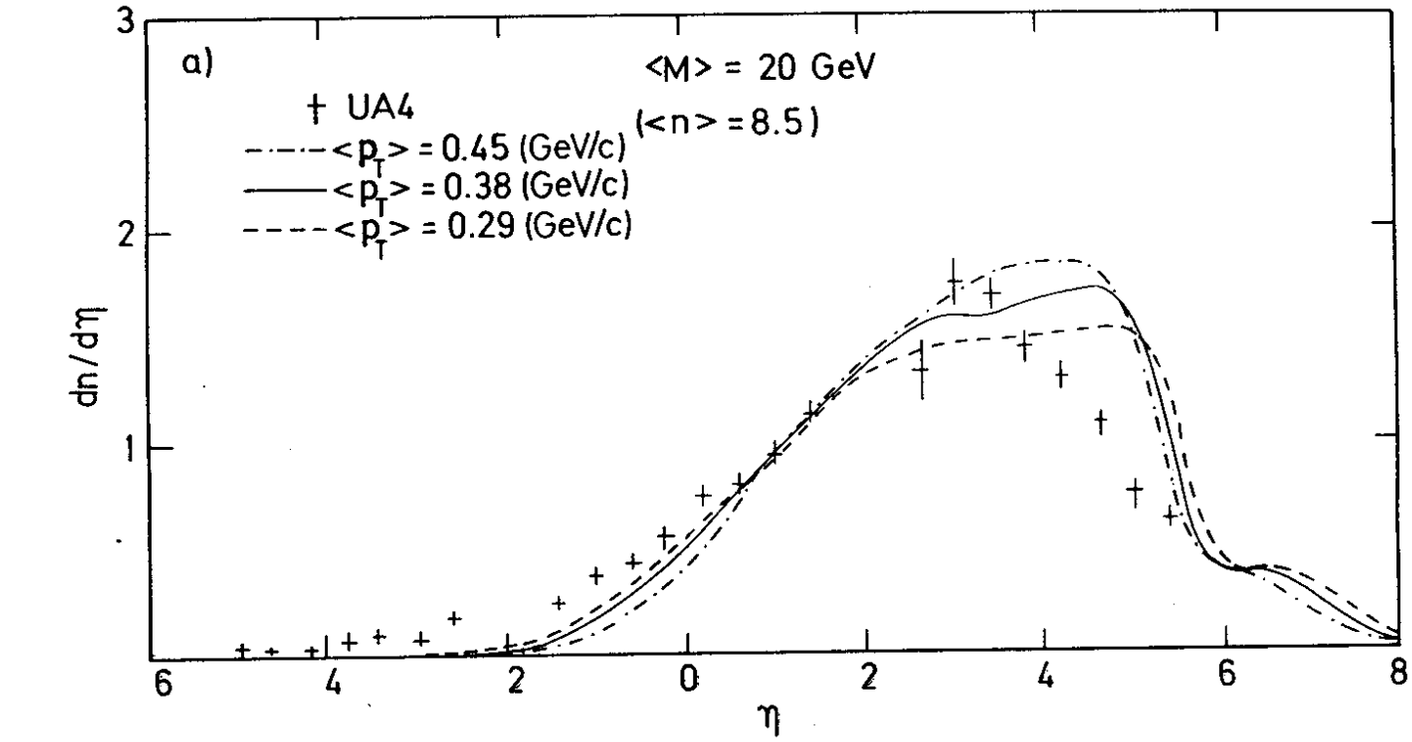
a)
<M> = 20 GeV
(<n> = 8.5)
+ UA4
<p_T> = 0.45 (GeV/c)
<p_T> = 0.38 (GeV/c)
<p_T> = 0.29 (GeV/c)
dn/dη
η

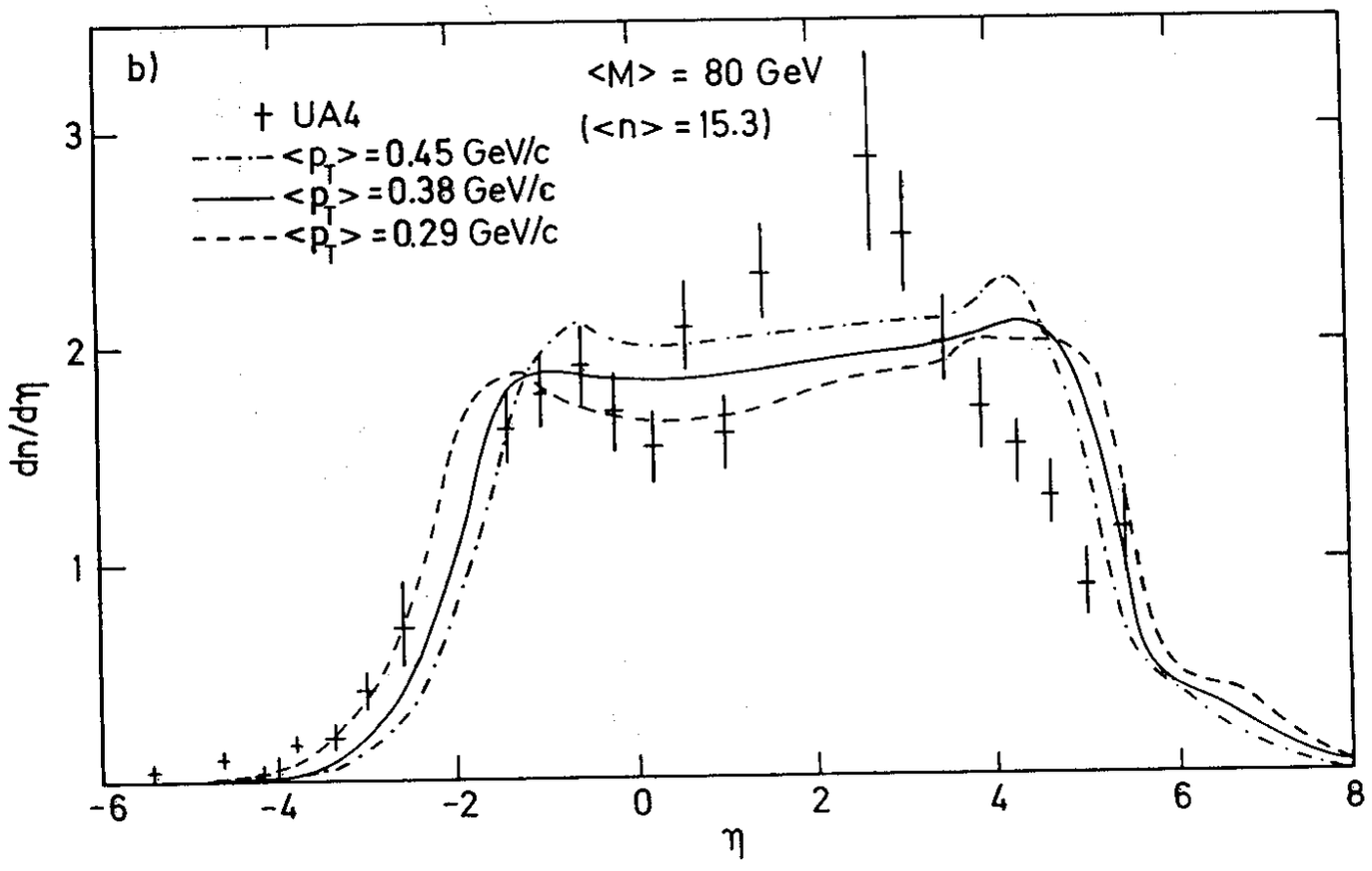
b)
<M> = 80 GeV
(<n> = 15.3)
+ UA4
<p_T> = 0.45 GeV/c
<p_T> = 0.38 GeV/c
<p_T> = 0.29 GeV/c
dn/dη
η

Fig. 3.28

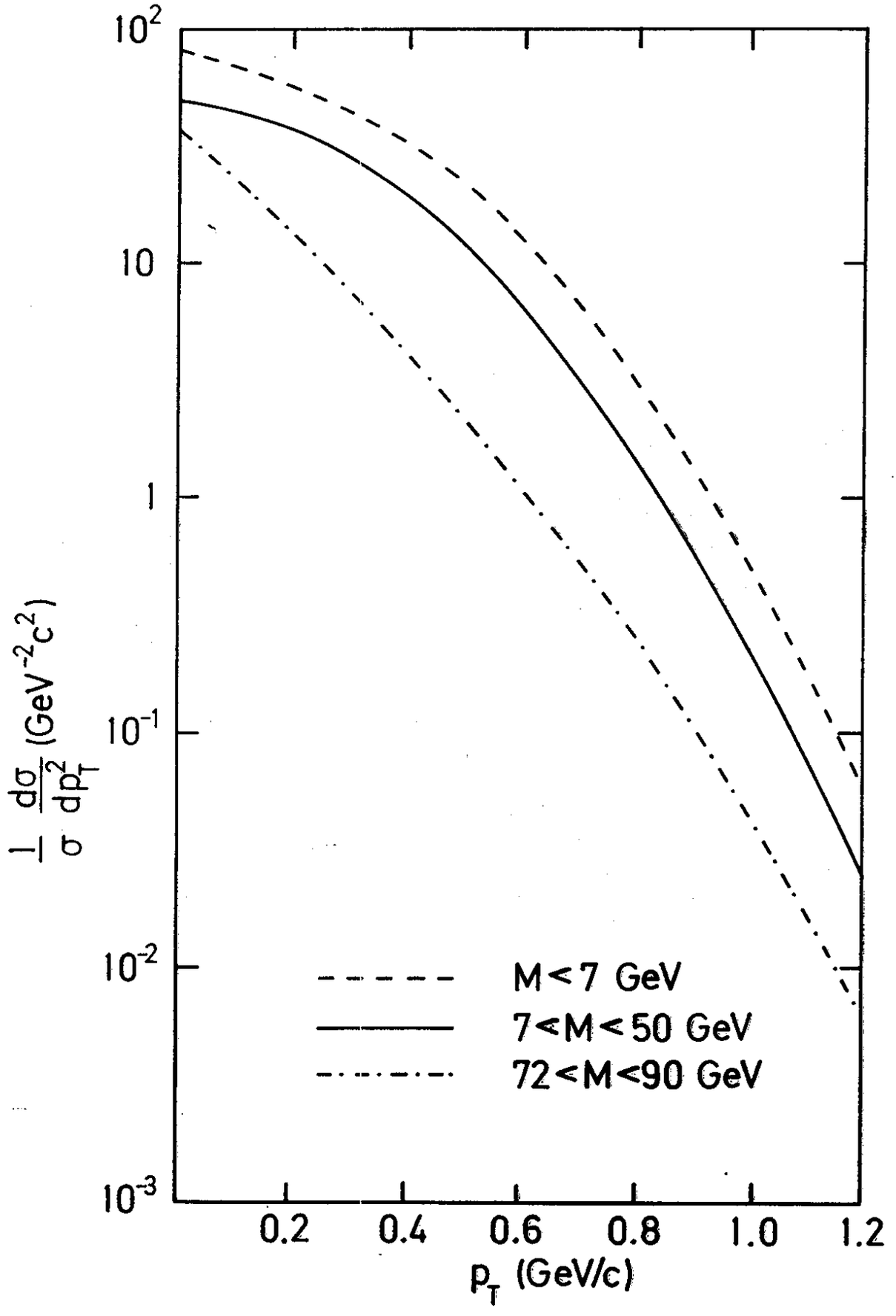
10^2
10
1
10^{-1}
10^{-2}
10^{-3}
$\frac{1}{\sigma}\frac{d\sigma}{dp_T^2}$ (GeV^{-2}c^2)
M<7 GeV
7<M<50 GeV
72<M<90 GeV
0.2
0.4
0.6
0.8
1.0
1.2
p_T (GeV/c)

Fig. 3.29

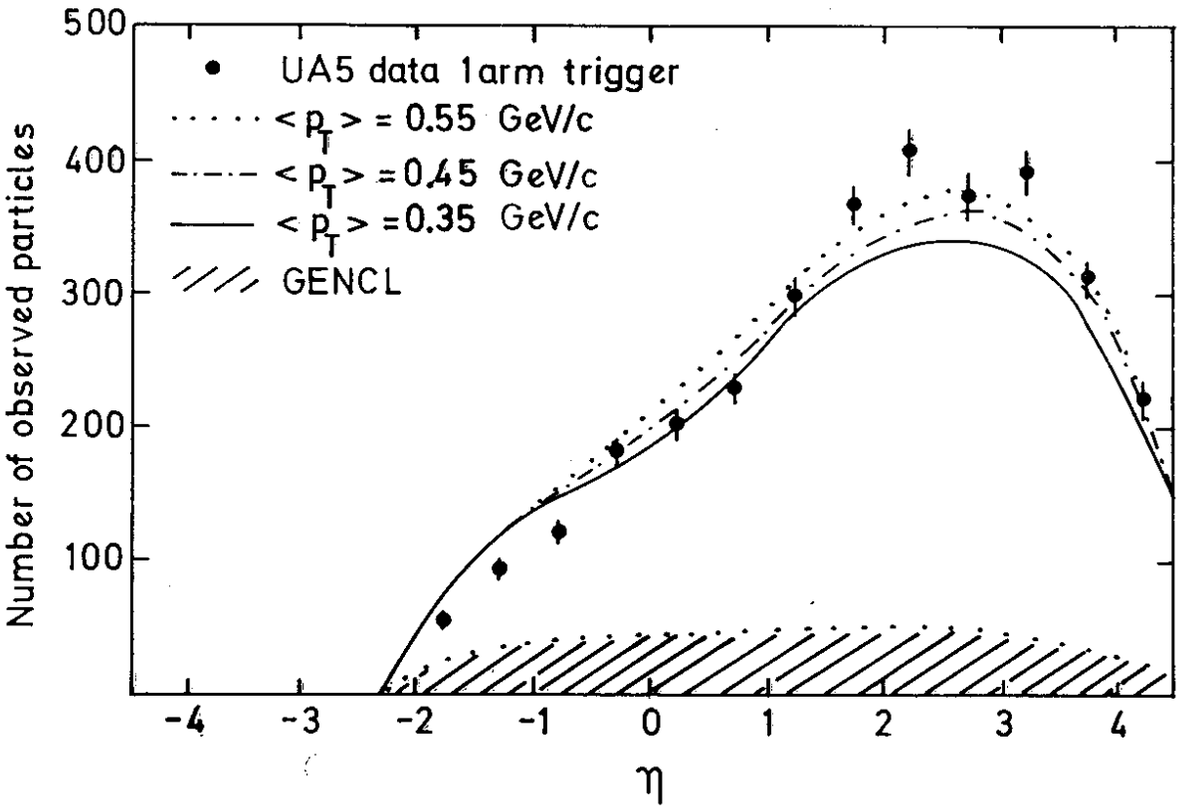
500
400
300
200
100
Number of observed particles
UA5 data 1arm trigger
< p_T > = 0.55 GeV/c
< p_T > = 0.45 GeV/c
< p_T > = 0.35 GeV/c
GENCL
-4
-3
-2
-1
0
1
2
3
4
η

Fig. 3.30

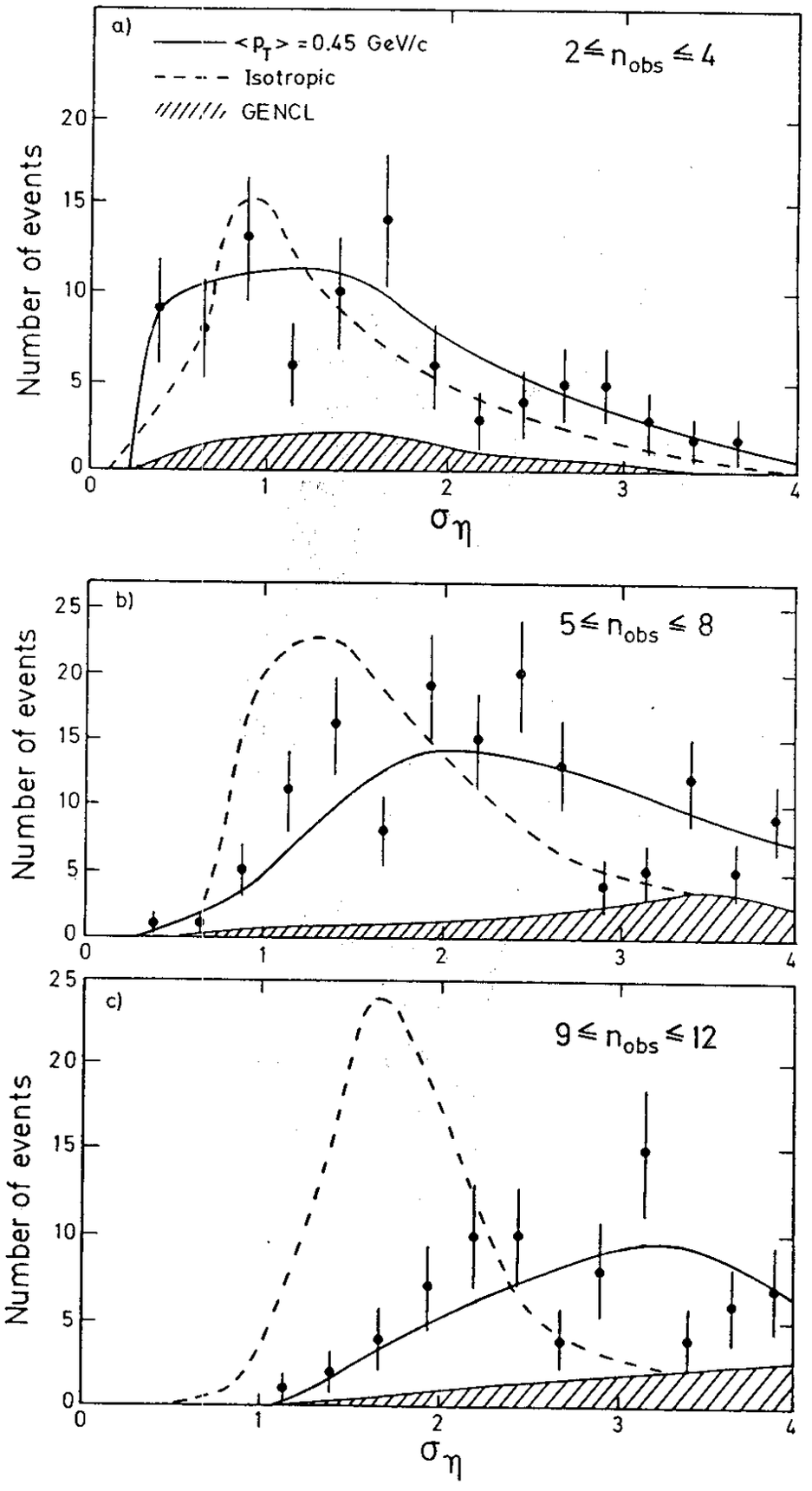
a)
$\langle p_T \rangle$ = 0.45 GeV/c
Isotropic
GENCL
$2 \leq n_{obs} \leq 4$
Number of events
σ_η
b)
$5 \leq n_{obs} \leq 8$
Number of events
c)
$9 \leq n_{obs} \leq 12$
Number of events
σ_η

Fig. 3.31

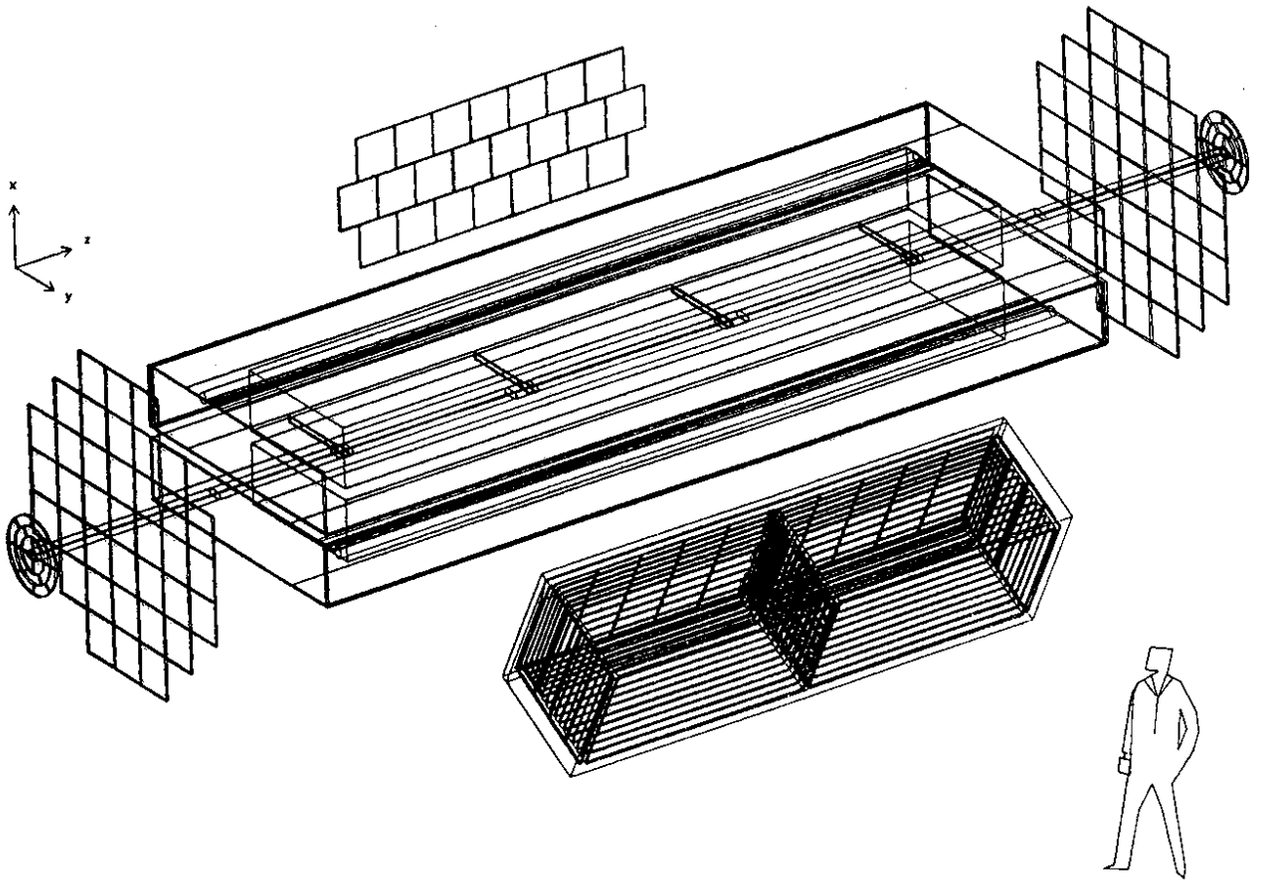

Fig. 4.1

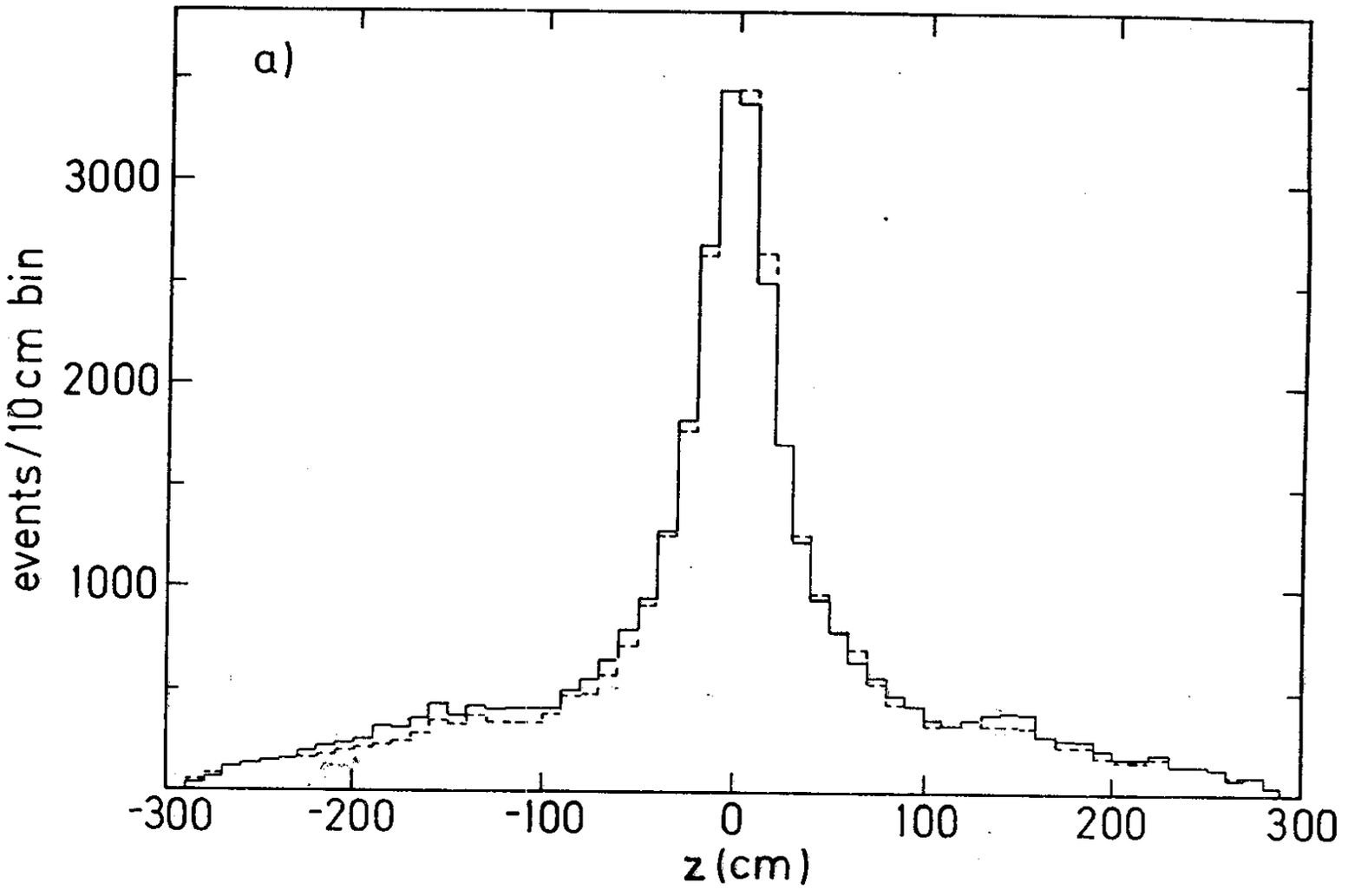
a)
3000
2000
1000
events/10cm bin
-300
-200
-100
0
100
200
300
z (cm)

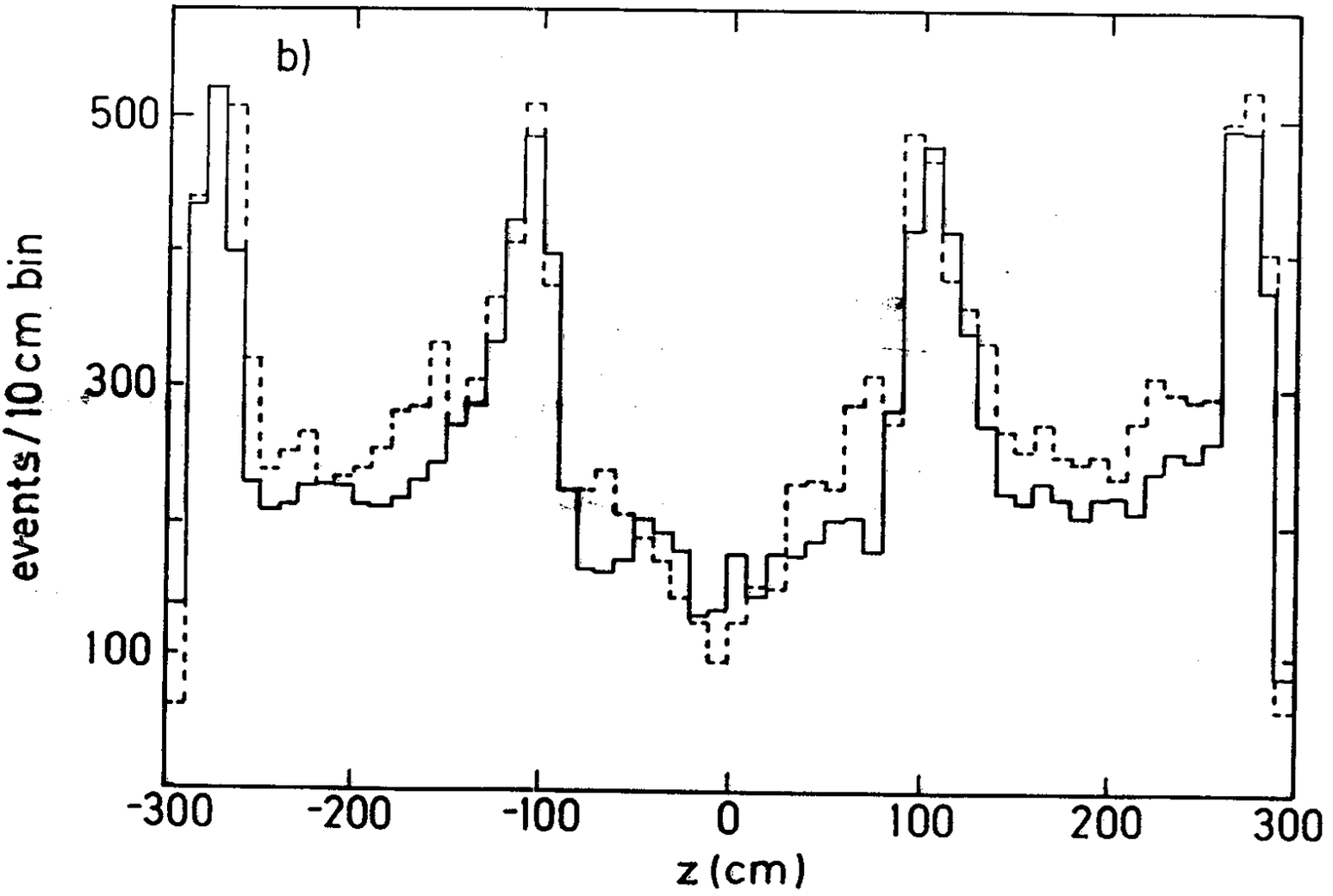
b)
500
300
100
events/10cm bin
-300
-200
-100
0
100
200
300
z (cm)

Fig. 4.2

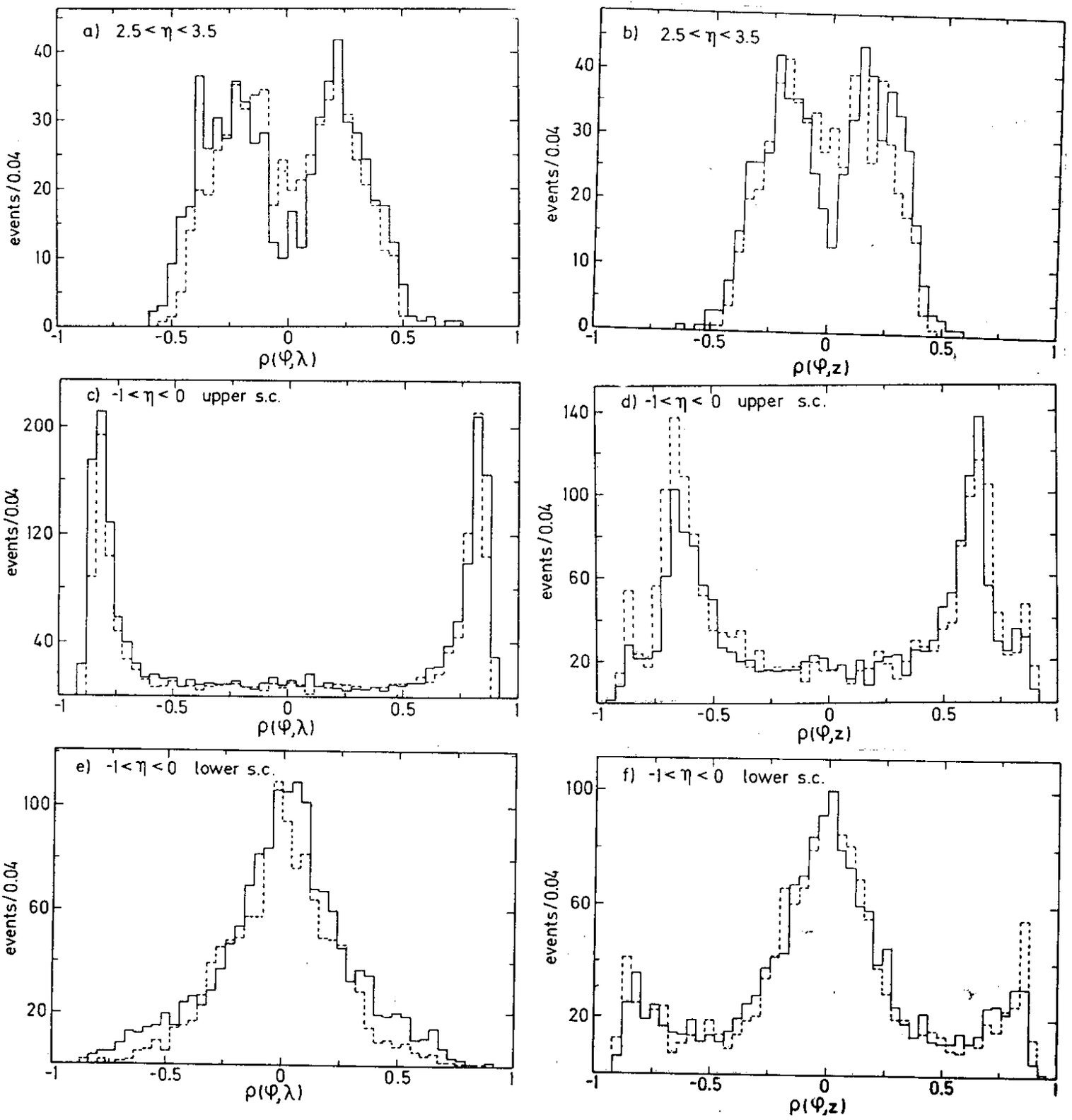
a) 2.5 < η < 3.5
b) 2.5 < η < 3.5
c) -1 < η < 0 upper s.c.
d) -1 < η < 0 upper s.c.
e) -1 < η < 0 lower s.c.
f) -1 < η < 0 lower s.c.
events/0.04
ρ(φ,λ)
ρ(φ,z)

Fig. 4.3